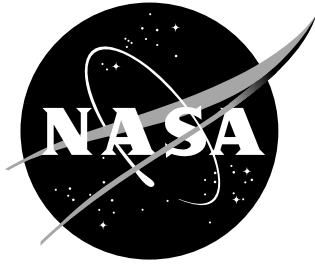


NASA / TP-2000-210551



Numerical Study of Rarefied Hypersonic Flow Interacting With a Continuum Jet

Christopher E. Glass
Langley Research Center, Hampton, Virginia

November 2000

The NASA STI Program Office ... in Profile

Since its founding, NASA has been dedicated to the advancement of aeronautics and space science. The NASA Scientific and Technical Information (STI) Program Office plays a key part in helping NASA maintain this important role.

The NASA STI Program Office is operated by Langley Research Center, the lead center for NASA's scientific and technical information. The NASA STI Program Office provides access to the NASA STI Database, the largest collection of aeronautical and space science STI in the world. The Program Office is also NASA's institutional mechanism for disseminating the results of its research and development activities. These results are published by NASA in the NASA STI Report Series, which includes the following report types:

- **TECHNICAL PUBLICATION.** Reports of completed research or a major significant phase of research that present the results of NASA programs and include extensive data or theoretical analysis. Includes compilations of significant scientific and technical data and information deemed to be of continuing reference value. NASA counterpart of peer-reviewed formal professional papers, but having less stringent limitations on manuscript length and extent of graphic presentations.
- **TECHNICAL MEMORANDUM.** Scientific and technical findings that are preliminary or of specialized interest, e.g., quick release reports, working papers, and bibliographies that contain minimal annotation. Does not contain extensive analysis.
- **CONTRACTOR REPORT.** Scientific and technical findings by NASA-sponsored contractors and grantees.

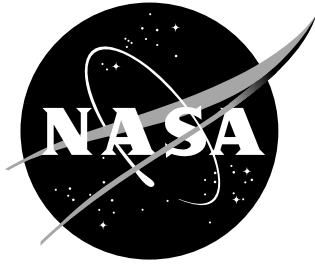
- **CONFERENCE PUBLICATION.** Collected papers from scientific and technical conferences, symposia, seminars, or other meetings sponsored or co-sponsored by NASA.
- **SPECIAL PUBLICATION.** Scientific, technical, or historical information from NASA programs, projects, and missions, often concerned with subjects having substantial public interest.
- **TECHNICAL TRANSLATION.** English-language translations of foreign scientific and technical material pertinent to NASA's mission.

Specialized services that complement the STI Program Office's diverse offerings include creating custom thesauri, building customized databases, organizing and publishing research results ... even providing videos.

For more information about the NASA STI Program Office, see the following:

- Access the NASA STI Program Home Page at <http://www.sti.nasa.gov>
- E-mail your question via the Internet to help@sti.nasa.gov
- Fax your question to the NASA STI Help Desk at (301) 621-0134
- Phone the NASA STI Help Desk at (301) 621-0390
- Write to:
NASA STI Help Desk
NASA Center for Aerospace Information
7121 Standard Drive
Hanover, MD 21076-1320

NASA / TP-2000-210551



Numerical Study of Rarefied Hypersonic Flow Interacting With a Continuum Jet

Christopher E. Glass
Langley Research Center, Hampton, Virginia

National Aeronautics and
Space Administration

Langley Research Center
Hampton, Virginia 23681-2199

November 2000

The information presented in this report was offered as a thesis in partial fulfillment of the requirements for the Degree of Doctor of Philosophy, The Pennsylvania State University, University Park, Pennsylvania, August 1999.

Available from:

NASA Center for AeroSpace Information (CASI)
7121 Standard Drive
Hanover, MD 21076-1320
(301) 621-0390

National Technical Information Service (NTIS)
5285 Port Royal Road
Springfield, VA 22161-2171
(703) 605-6000

This report is also available in electronic form at URL <http://techreports.larc.nasa.gov/ltrs/>

Abstract

An uncoupled Computational Fluid Dynamics–Direct Simulation Monte Carlo (CFD–DSMC) technique is developed and applied to provide solutions for continuum jets interacting with rarefied external flows. The technique is based on a correlation of the appropriate Bird breakdown parameter for defining a surface within which the continuum solution is unaffected by the external flow–jet interaction. This surface is then used to uncouple the continuum CFD solution from the non-continuum DSMC solution to obtain a solution for the entire flow field including the interaction region. The technique is applied to two problems to assess and demonstrate its validity: one of a jet interaction in the transitional–rarefied flow regime and the other in the moderately rarefied regime.

The correlation is obtained by analyzing the structure of various Bird breakdown surfaces for a range of jet to free stream conditions, and the results show that the appropriate Bird breakdown surface for uncoupling the continuum and non-continuum solutions is a function of a non-dimensional parameter relating the momentum flux and collisionality between the two interacting flows. The correlation is exploited for the simulation of a jet interaction modeled for an experimental condition in the transitional–rarefied flow regime and the validity of the correlation is demonstrated. This is the first time such a correlation has been obtained for defining a Bird breakdown parameter appropriate to a continuum jet with a rarefied flow.

The uncoupled technique is also applied to an aerobraking flight condition for the Mars Global Surveyor spacecraft with attitude control system jet interaction. Aerodynamic yawing moment coefficients for cases without and with jet interaction at various angles-of-attack were predicted, and results from the present method compare well with values published previously. The flow field and surface properties are analyzed in some detail to describe the mechanism by which the jet interaction affects the aerodynamics.

Table of Contents

List of Tables	vii
List of Figures	viii
Nomenclature	xii
Acknowledgments	xv
Preface	xvii
Chapter 1. Literature Review of Jet Interaction Flows	1
1.1 Challenge of a Jet Interacting with Rarefied Flow	1
1.2 Jet Interactions in Various Flow Regimes	7
1.2.1 Free Molecular Flow Regime	8
1.2.2 Rarefied Flow Regime	11
1.2.2.1 Experimental Studies	12
1.2.2.2 Computational Studies	15
1.2.3 Continuum Flow Regime	17
1.3 Summary	18
Chapter 2. Uncoupled CFD–DSMC Technique	20
2.1 Jet Interaction Flow Field	20
2.2 CFD–DSMC Uncoupling at the Breakdown Surface	21

2.3	Numerical Methods	25
2.3.1	Computational Fluid Dynamics	25
2.3.1.1	Historical Perspective	26
2.3.1.2	Governing Equations	34
2.3.1.3	Solution Method	36
2.3.2	Direct Simulation Monte Carlo	43
2.3.2.1	Historical Perspective of Kinetic Theory	44
2.3.2.2	Application of the Solution Technique	51
Chapter 3.	Jet Interaction with Transitional–Rarefied Flow over Flat Plate . . .	54
3.1	Discussion of the Jet Interaction Experiment	54
3.2	Assessment of 2-D Flat Plate Flow	58
3.2.1	Common Viscous Interaction Parameters	58
3.2.2	DSMC Modeling by the G2 Code	61
3.3	Uncoupled Technique for Transitional–Rarefied Flow	68
3.3.1	CFD Modeling of the Jet Interaction	69
3.3.2	Non-Interacting Continuum Jet Plume Surface	74
3.3.3	Analysis of the Non-Interacting Jet Plume Surface	77
3.4	Uncoupled CFD–DSMC Jet Interaction	83
3.4.1	CFD Modeling of the Continuum Jet	84
3.4.2	Surface Triangulation for DSMC	86
3.4.3	DSMC Modeling of the Interacting Flow Field	90
3.4.4	Analysis of DSMC Results	105

3.4.5	Effect of DSMC Grid on Flow and Surface Properties	116
3.4.6	Effect of Bird Breakdown Parameter	124
Chapter 4.	MGS Jet Interaction with Rarefied Flow	143
4.1	MGS Aerobraking Maneuver	143
4.2	CFD Modeling of Attitude Control System (ACS) Thruster	146
4.3	Breakdown of Continuum Jet Flow	151
4.4	Surface Triangulation for DSMC	154
4.5	DSMC Modeling of MGS	155
4.5.1	MGS Flow Field Without Jet Interaction	157
4.5.2	MGS Flow Field With Jet Interaction	163
4.5.3	MGS Surface Pressure Without and With Jet Interaction . . .	170
4.6	MGS Aerodynamics	176
Chapter 5.	Concluding Remarks	181
Chapter 6.	Direction for Future Research	183
References	185
Appendix.	Flow Field and Surface Properties from the Uncoupled CFD–DSMC	
	Solution (available online at http://techreports.larc.nasa.gov/ltrs/)	198
A.1	Symmetry Plane Flow Field Properties	199
A.1.1	Coarse Grid Resolution	201
A.1.2	Fine Grid Resolution	251
A.2	Upper Plate Surface Properties	324

A.2.1	Coarse Grid Resolution	324
A.2.2	Fine Grid Resolution	345

List of Tables

A.1 Flow field variables on symmetry plane, coarse grid. 201

A.2 Flow field variables on symmetry plane, fine grid. 251

A.3 Surface variables on upper plate, coarse grid. 326

A.4 Surface variables on upper plate, fine grid. 345

List of Figures

1.1	Jet interaction corner flow model of Allègre and Raffin [3].	13
3.1	Schematic diagram of the jet interaction flat plate model.	56
3.2	Viscous interaction parameters of the upper flat plate surface flow with no jet interaction.	60
3.3	Number density contours of the flat plate flow from the G2 DSMC solution.	63
3.4	Boundary layer edge and local Knudsen number of the upper surface flat plate flow with no jet interaction.	65
3.5	Rarefaction of the flat plate upper surface flow with no jet interaction. .	67
3.6	Selected grid planes of the CFD computational domain.	70
3.7	Flow field streamlines on the symmetry plane from the CFD solution. .	73
3.8	Number density contours on the symmetry plane from the CFD solution.	75
3.9	Jet breakdown surface from CFD solution (P is the Bird breakdown parameter).	79
3.10	Correlation of breakdown parameter value at jet plume breakdown sur- face interface with interaction for $Kn_d = 0.038$	82
3.11	CFD grid and number density contours for axisymmetric free expanding jet.	85
3.12	Triangulated flat plate and jet plume continuum surface geometries. . .	89
3.13	Uniform grid for DSMC jet interaction simulation.	91
3.14	Number density contours from the uniform grid solution.	93

3.15	Grid after first adaptation for DSMC jet interaction simulation.	95
3.16	Number density contours from first adapted grid solution.	96
3.17	Grid after second adaptation for DSMC jet interaction simulation. . . .	98
3.18	Number density contours from second adapted grid solution.	100
3.19	Grid after third adaptation for DSMC jet interaction simulation.	102
3.20	Number density contours from third adapted grid solution.	104
3.21	Comparisons of pressure, heating, and shear stress on the flat plate sur- face at the symmetry line.	106
3.22	Flow separation and attachment caused by the flat plate jet interaction.	109
3.23	Jet interaction flow field at various cross flow planes.	114
3.24	Symmetry plane number density contours from the $P = 0.01$ uncoupled CFD-DSMC solution showing key locations for comparisons.	118
3.25	Effect of DSMC grid on location of compression wave flow field features.	119
3.26	Effect of DSMC grid on center line surface properties.	122
3.27	Comparison of Ar jet flow properties forward of the jet exit on the sym- metry plane at $P = 0.011$	125
3.28	Comparison of Ar jet flow properties on the $x = 0.125m$ cross flow plane at $P = 0.011$	126
3.29	Comparison of Ar jet flow properties aft of the jet exit on the symmetry plane at $P = 0.011$	127
3.30	Flow variable change along line 1 as a function of breakdown parameter value.	130

3.31	Flow variable change along line 2 as a function of breakdown parameter value.	131
3.32	Flow variable change along line 3 as a function of breakdown parameter value.	132
3.33	Number density contours on the symmetry plane for various breakdown parameters.	136
3.34	Number density contours at $x = 0.125$ m cross flow plane for various breakdown parameters.	137
3.35	Surface pressure comparisons to show effect of breakdown parameter. . .	140
3.36	Detailed surface pressure and simulated oil flow comparisons at the nozzle exit location.	141
4.1	Surface geometry of the Mars Global Surveyor (MGS) aerobraking configuration.	145
4.2	CFD grid for the MGS ACS thruster (Primex MR-111C).	148
4.3	Number density contours and streamlines for MGS ACS thruster.	150
4.4	$P = 0.02$ breakdown surface location for MGS ACS thruster.	153
4.5	Closeup view of MGS ACS thruster and $P = 0.02$ breakdown surface. . .	156
4.6	Planar cross section of MGS flow field with no ACS jet interaction ($\alpha = 0^\circ$). . .	158
4.7	Planar cross section of MGS flow field with no ACS jet interaction ($\alpha = 15^\circ$).	161
4.8	Planar cross section of MGS flow field with no ACS jet interaction ($\alpha = -15^\circ$).	162

4.9	Planar cross section of MGS flow field with ACS jet interaction ($\alpha = 0^\circ$).	166
4.10	Planar cross section of MGS flow field with ACS jet interaction ($\alpha = 15^\circ$).	168
4.11	Planar cross section of MGS flow field with ACS jet interaction ($\alpha = -15^\circ$).	169
4.12	Windward surface pressure contours on MGS ($\alpha = 0^\circ$).	172
4.13	Windward surface pressure contours on MGS ($\alpha = 15^\circ$).	173
4.14	Windward surface pressure contours on MGS ($\alpha = -15^\circ$).	175
4.15	Comparison of yawing moment coefficient for the MGS without and with ACS jet interaction.	178
A.1	Flow field on the symmetry plane showing locations of the coarse and fine grid resolution regions.	200
A.2	Diagram of flat plate model showing locations of the coarse and fine grid resolution regions.	325

Nomenclature

A	= area, m^2
\mathbf{c}	= molecular velocity vector, m/sec
C	= Chapman-Rubeson constant
C_{Mx}	= yawing moment coefficient
d	= diameter, m
e	= specific internal energy, J/kg
f	= velocity distribution function
f_o	= Maxwellian velocity distribution function
\mathbf{F}	= inviscid flux vector
\mathbf{F}_v	= viscous flux vector
g_i	= gravitational field
G	= non-dimensional ratio of number density flux, nV , with the molecular collision probability flux, $\frac{\nu}{\lambda d}$
h	= specific enthalpy, J/kg
k	= Boltzmann constant, $1.38 \times 10^{-23} \text{ J/K}$
Kn	= Knudsen number, λ/L
L	= length, m
m	= mass, kg
M	= Mach number
M	= molecular weight, kg/mole

n	= number density, molecules/m ³
n_o	= Loschmidt's number, 2.687×10^{25} molecules/m ³
$\hat{\mathbf{n}}$	= unit normal
N	= inverse of Bird breakdown parameter, $\frac{1}{P}$
N	= Avogadro's number, 6.0225×10^{26} molecules/kg-mole
p	= pressure, Pa
P	= Bird breakdown parameter, $\frac{\vec{V} \cdot \nabla \rho}{\nu \rho}$
q	= dynamic pressure, Pa
\mathbf{q}	= primitive variable vector
\dot{q}'' or q_i	= heat flux, W/m ²
\mathbf{Q}	= conservative variable vector
\mathbf{r}	= position vector, m
Re	= Reynolds number, $\frac{\rho V L}{\mu}$
\mathbf{S}	= chemical source vector
T	= temperature, K
T_{Kn}^*	= normalized Knudsen layer edge temperature
\mathbf{u} or u_i	= velocity vector with components u , v , and w , m/sec
V	= velocity, m/sec
V	= volume, m ³
\bar{V}	= viscous interaction parameter, $\frac{M_\infty}{\sqrt{Re}} \sqrt{C}$
V_{Kn}^*	= normalized Knudsen layer edge velocity
x, y, z	= Cartesian coordinates, m

α	= angle-of-attack, deg
$\delta_{0.99}$	= boundary layer edge
λ	= molecular mean free path, m
μ	= viscosity, kg/m-sec
ν	= intermolecular collision frequency, 1/sec
ρ	= density, kg/m ³
τ	= characteristic time, sec; also shear stress, Pa
σ	= molecular cross section, m ²
Ω	= solid angle, sterad
$\bar{\chi}$	= viscous interaction parameter, $\frac{M_\infty^3}{\sqrt{Re}}\sqrt{C}$

Subscripts

d	= with respect to diameter
eff	= effective
jet	= jet nozzle exit
l	= local condition
mix	= mixture
q, p	= species in the mixture
∞	= free stream

Superscripts

*	= post-collision condition
---	----------------------------

Acknowledgments

I am most grateful and indebted to my thesis advisor, Vigor Yang, for taking me as his student at Penn State and for providing guidance with this research effort. I am also grateful and indebted to the other committee members, John Cimbala, Gary Settles, Lyle Long, and Richard Wilmoth for their thoughtful comments and suggestions. Furthermore, technical discussions with Graeme Bird, Gerald LeBeau, and James Moss have been helpful in clarifying various aspects of this research relating to rarefied flow and the direct simulation Monte Carlo technique.

In addition, I'm indebted to some members of the staff at NASA Langley Research Center: to my branch heads, Alan Wieting and Charles Miller III, for their encouragement and for allowing me time from my other duties to pursue an advanced degree at Penn State; to Karen Bibb and the GeoLab staff for their help in producing some of the geometry files used in this study; to William Kleb for locating some of the reference material used in this study; and to George Allison for managing the financial support provided to me during the years of study.

Personal acknowledgments are given to friends and colleagues I met while at the Penn State Gas Dynamics Lab for making the time spent there meaningful and enjoyable: Farrukh Alvi, Louis Cattafesta III, Lori Dodson, Sanjay Garg, Timothy Garrison, Joseph Hsu, Steven Johnson, Yeol Lee, Steven McIntyre, J. D. Miller, and Jonathan Naughton.

This document was typeset using the L^AT_EX 2_ε system. The thesis and bibliography style files were provided by Stephen G. Simpson at The Pennsylvania State

University anonymous FTP site <ftp://ftp.math.psu.edu/pub/simpson/tex/>. Thanks are given to William Wood for his help with the $\text{\LaTeX} 2_{\epsilon}$ system. Lastly, and most of all, an acknowledgment to my wife, Dorothy Glass, for her support while I pursued this goal and her help in editing this thesis.

Preface

The present research effort was initiated at the NASA Langley Research Center Aerothermodynamics Branch because there was a need to better understand and predict the effects of reaction control system jets on vehicle aerodynamics in the rarefied flow regime, where the flow field surrounding the vehicle contains both continuum and non-continuum fluid. The effect of reaction control system jet interaction is not well understood in the rarefied flow regime and may have an unanticipated influence on vehicle aerodynamics. Typically, these effects are obtained from conventional wind-tunnel-derived empirical relationships, and large variances are allowed in the vehicle flight control laws that use the relationships to account for the uncertainty. However, with emerging computational tools and techniques, such as massively parallel, multi-processor computers and direct simulation Monte Carlo method computer codes written to take advantage of the multi-processor capability, problems, which were previously too large to simulate numerically, can now be solved routinely. To this end, the methodology developed during the course of this study can be applied to numerically predict effects of a reaction control system on vehicle aerodynamics in the rarefied flow regime for upcoming aerospace vehicles such as the reusable launch vehicle (RLV) and the Future-X.

Chapter 1

Literature Review of Jet Interaction Flows

1.1 Challenge of a Jet Interacting with Rarefied Flow

A critical design concern for vehicles that pass through the rarefied regime of an atmosphere, either during a deorbit or to accomplish an orbital aerobrake maneuver, is vehicle stability and control. In this less dense portion of an atmosphere where density changes rapidly with altitude, common vehicle aerodynamic control surfaces such as elevons, wing and body flaps, and rudders, etc. are not effective. When these surfaces are deflected, generated forces are small and generally not large enough to adequately produce stable flight control. Active flight control in the rarefied regime is obtained using a reaction control system (RCS). The RCS is an arrangement of jet thrusters placed strategically about the vehicle surface offset from the center of gravity, which produces forces that generate moments and control vehicle roll, pitch, and yaw. Because the RCS jets issue from the vehicle surface as a continuum plume, it is important in the vehicle design to understand the effect of the interacting continuum jet with the locally changing rarefied flow field on vehicle aerodynamics.

For example, as the Shuttle Orbiter leaves orbit for an atmospheric entry, the RCS is initially the only vehicle control mechanism. After passing through the free molecular regime during entry, the Shuttle Orbiter enters the rarefied flight regime. The number density of the free stream increases with decreasing altitude, and the RCS jets begin to

interact with the local flow. The RCS provides vehicle control for the Shuttle Orbiter through the transition from the rarefied to the continuum regime until the aerodynamic control surfaces become effective trim devices. Roll control jets are operated down to a flight dynamic pressure of 480 Pa, and pitch control jets to a dynamic pressure of 960 Pa (Kanipe [41]). However, the aft yaw RCS jets are required for trim from entry interface with the atmosphere down to flight speeds of about Mach number one (Kanipe [41] and Romere et al. [67]).

Early experience with the Shuttle Orbiter showed that the RCS jet interaction scaling parameters from conventional wind tunnel tests marginally predicted hypersonic aerodynamic flight characteristics in the rarefied and near rarefied continuum regimes (For example, see Kanipe and Roberts [42], Kanipe [41], Romere et al. [67], and Scallion [74]). During the first Shuttle Orbiter entry, discrepancies between flight and predicted vehicle aerodynamics were observed from the rarefied down to the continuum regime at about Mach number 10. Pitching moment based on body flap deflection was not predicted correctly (Throckmorton [83]), and induced rolling moment from aft RCS yaw jet interaction was over predicted (Kanipe and Roberts [42], Romere et al. [67], Allègre et al. [3]; and Scallion [74]). The aerodynamic predictions for the Shuttle Orbiter were based on Mach 10 wind tunnel experiments and extrapolated to higher flight Mach numbers using scaling parameters (Kanipe and Roberts [42] and Kanipe [41]). Rarefaction and high-temperature effects during high Mach number flight are different from those in the wind tunnel, which may lead to an incorrect simulation (Allègre et al. [3]). Scallion [74] suggests the most probable cause of the discrepancy between wind tunnel and flight RCS interaction effects is not including vehicle wake correlations in the

scaling parameter definition. Although discrepancies existed between predictions and flight, the uncertainty boundary of the flight control system during the Shuttle Orbiter first flights was wide enough to compensate for the differences (Kanipe [41] and Romere et al. [67]).

The National Aeronautics and Space Administration (NASA) Shuttle Orbiter has been operational for almost two decades using technologies developed nearly thirty years ago. Laws of the vehicle flight control system are empirically based, obtained first by extrapolated wind tunnel scaling parameters, then modified as flight operational data became available. NASA has proven by the success of the program that aerodynamic control of the Shuttle Orbiter can be maintained during descent from orbit. The gross effect of the RCS jet interaction on vehicle control is known through flight experience, but local flow field and surface effects caused by the interaction are not well understood (Scallion [74]). By understanding better the effects of RCS jet interactions, especially in the rarefied high-speed flight regime, the uncertainty in force and moment predictions will be reduced, thus increasing flight control efficiency (Romere et al. [67]).

In an effort to ensure reliable and affordable future access to space for the nation, NASA is developing new technologies for a next generation single-stage-to-orbit (SSTO) reusable launch vehicle (RLV) (Throckmorton [83] and Goldin [32]). The RLV is planned to complement and eventually replace the current Shuttle Orbiter space transportation system. Because the RLV will operate in a flight regime similar to that of the Shuttle Orbiter, it will clearly need an RCS during orbital maneuvers and atmospheric entry at the end of a mission. The effects of the RCS jet interaction on the Shuttle Orbiter aerodynamic characteristics is well known by experience throughout the flight profile;

however, these effects are configuration specific, and the extensive database is not applicable to other vehicle classes (Scallion [74]). Therefore, studies of the RCS interaction effects applicable to the RLV configuration should be undertaken. Of interest are RCS interactions during entry through the rarefied, near-rarefied, and continuum flow regimes where scaling laws from conventional wind tunnels will need to be refined using results from numerical studies to provide an adequate flight aerodynamic database.

Much international interest has recently been generated in defining effects of RCS interactions for planned space vehicles entering the Earth's atmosphere after orbit. The H-II Orbiting Plane (HOPE), an unmanned Japanese reusable space transportation vehicle, was designed to use RCS for control during its transit through the rarefied regime after deorbit (Yamamoto [96] and Nagai et al. [54]). Flight tests to verify computational fluid dynamics (CFD) and experimental scaling parameters have been accomplished on the Japanese Hypersonic Flight Experiment (HYFLEX) (Watanabe and Takaki [91] and Watanabe et al. [90]). Analysis of flight data from HYFLEX was planned to aid in the development of HOPE (Watanabe et al. [90]). The European Space Agency (ESA) also had an interest in defining the effects of RCS interactions for their HERMES space vehicle. Pörtner [61] reviewed the Shuttle Orbiter RCS scaling parameters used for predicting aerodynamic flight performance, made recommendations for HERMES RCS wind tunnel tests (Pörtner [61]), and tested the HERMES 1.0 configuration in the German DLR V2G hypersonic vacuum tunnel to assess RCS interaction effects on the thruster leading edge (Pörtner [62]). Although the HOPE (Kallender [40]) and the HERMES programs have been cut or scaled back significantly, early RCS interaction studies show the importance placed on an RCS interaction database for these vehicles.

Another class of vehicles, planetary probes such as the Magellan and Mars Global Surveyor (MGS), used RCS in a rarefied atmosphere during the actively controlled aerobraking phase of their missions; for example, see Rault [63], Rault et al. [65], Shane et al. [76], and Shane [77]. A planetary exploration program has been established and the MGS is the first spacecraft of a series of orbiters and landers of the Mars Surveyor Program (NASA [55] and Goldin [32]). A pair of spacecraft is planned to be sent to Mars every twenty-six months for the next five years. The next surveyor missions are the Mars Surveyor 1998 and the Mars Surveyor 2001; the Mars Surveyor 1998 was launched December 11, 1998 and is presently in the cruise phase of the mission to Mars. Both the MGS and Mars Surveyor 1998 are actively controlled by RCS during aerobraking maneuvers to correct any anomaly in the vehicle trajectory while circularizing the orbit about Mars.

Rault [63] studied an actively controlled aerobraking maneuver of the Magellan spacecraft in the atmosphere of Venus using the direct simulation Monte Carlo (DSMC) method. After the primary surface mapping mission objectives were met, interest focused on obtaining higher resolution atmospheric planetary measurements, which required the spacecraft to be placed into a lower Venus orbit. Rault [63] used a DSMC molecular simulation to analyze aerodynamic characteristics of Magellan during flight through the rarefied atmosphere. For one of the final experiments of Magellan in 1993, the Windmill Experiment, RCS was used to offset torque induced by the solar panels pinwheeling while the spacecraft traveled about the lower orbit. One goal of the experiment was to obtain an indirect measurement of solar panel and vehicle surface momentum accommodation in the Venus atmosphere (Rault et al. [65]). Large discrepancies existed between flight

data and aerodynamic moments predicted by a free molecular analysis. Application of the DSMC by Rault et al. [65], in which the RCS jets were modeled as a source flow from the vehicle surface, showed better agreement with the flight data. The much higher density RCS jet plumes interacted with the free stream and shadowed the solar panels and a portion of the spacecraft from the lower density incoming flow, thus affecting vehicle aerodynamic loads.

The DSMC technique was also applied by Rault et al. [65] to predict aerodynamics of the MGS from RCS interaction during Mars orbital aerobraking maneuvers. A jet flow model, similar to the one used for the Magellan DSMC study, was incorporated to include the RCS jets in the simulation. The study showed that an effective thrust reversal will occur on the MGS because of jet interaction effects when the RCS is fired during orbital periapsis, an unexpected result. The RCS jets for both of the planetary studies was simulated as an inflow of molecules into the DSMC computational domain from discrete locations on the spacecraft surface. Shane et al. [76] have applied the same technique to analyze the aerodynamic effects of an unlocked and out-of-alignment MGS solar panel during the RCS burn phase of the aerobraking maneuver with the Martian atmosphere. The study provides details of the extent of thrust reversal as a function of orbital altitude (that is, free stream number density). Although specific aerodynamic characteristics of planetary aerobraking in the rarefied regime during an RCS jet firing for Magellan and MGS have been studied (Rault [63], Rault et al. [65], and Shane et al. [76]), more investigations will be necessary to quantify aerobraking vehicle aerodynamics for future planetary missions because interaction effects from RCS jets in the rarefied flow regime are configuration specific.

Defining the effects of RCS interactions in the rarefied flight regime poses unique challenges for the vehicle design and aerodynamic control. Extensive RCS interaction wind tunnel tests were performed for the Shuttle Orbiter design because numerical techniques were at that time considered unreliable. Experimental scaling parameters were derived from wind tunnel test results and extrapolated to flight as vehicle control laws. As confidence in numerical techniques has grown, a different approach has evolved to define the effects of RCS interactions. The method proposed and begun by the Japanese to define the effects of RCS interactions for the HOPE space vehicle was to develop scaling parameters based on a mix of computational fluid dynamics (CFD) simulations and wind tunnel and flight experiments. Recent studies of the RCS interacting flow field for planetary probes during actively controlled aerobraking maneuvers have been performed as molecular simulations using the DSMC technique. Results from the DSMC RCS studies for the Magellan and MGS missions have provided physical insight into the flow physics of rarefied jet interactions, in particular, the high density jet plume shadowing the free stream and causing a thrust reversal in the rarefied flight regime.

1.2 Jet Interactions in Various Flow Regimes

Described in Section 1.1 are specific examples of vehicles that encounter jet interactions with rarefied free stream. Presented in this section is a brief overview of jet interactions with non-rarefied free stream conditions and some recent generic experimental and computational jet interactions with rarefied free stream flow.

Interacting jet flows have many practical engineering applications, which extend from hypersonic near free molecular interactions to low speed continuum free stream flow

interactions. A review of currently available methods, which can be applied to study jet interactions, shows that traditionally, wind tunnel experiments have defined the physical aspects of a given problem. Recently, however, with the arrival of supercomputers and advanced computational techniques, jet interactions are being explored numerically. Both numerical and experimental techniques have strengths and weaknesses: Computational studies can provide a solution of all relevant properties over an entire domain of interest, whereas, an experiment provides only those properties that can be physically measured or inferred from measurements. Computational techniques do suffer grid resolution, convergence, and other problems, which are topics of current research efforts. However, the combination of both experimental and computational techniques applied to a given jet interaction study provides much greater understanding of fundamental flow physics than either technique can provide independently.

1.2.1 Free Molecular Flow Regime

The weakest jet interaction with the free stream occurs in the free molecular flow regime. Jet thrusters of an RCS are used for vehicle control during maneuvers such as orbital adjustments, docking, moon landing, and manned extravehicular activities (EVA) (Dettleff [19]). Generally, jet interactions with the free stream flow are negligible on orbit because the space surrounding the vehicle has very few molecules with which the high density RCS jet flow can interact. The RCS jet expands freely in this regime and provides thrust for vehicle control. Dettleff [19] has extensively reviewed jet plume flow for space technology applications. Although jet interactions with the free stream are not a concern, defining plume impingement effects on surrounding vehicle structural components is

important. Mass, momentum, and energy are transferred from the jet plume to the surrounding vehicle structure and cause contamination, undesired forces, and structural heating. The thorough review of plume impingement by Dettleff [19] includes discussions of the effects of jet exit Reynolds number, jet plume specific heat ratio, angle and source distance of the plume surface impingement, multiple jets interacting, and correlations of these effects derived from vacuum tunnel experiments.

Recently, Lumpkin et al. [47] and Rault [64] studied plume impingement from Shuttle Orbiter RCS during docking maneuvers with the Russian space station Mir to ensure jet plume impingement pressure and heat loads did not damage the Mir solar panels or cause attitude control problems. Prior to this type of numerical study, plume impingement effects would be quantified by engineering codes making use of corrections such as those presented by Dettleff [19]; however, the Shuttle Orbiter docking maneuver with the Mir was simulated by a combined CFD–DSMC approach to provide an independent assessment of pressure and heat loads. The CFD solution technique was applied to the expanding plume flow in the immediate vicinity outside of the RCS nozzle exit, and a continuum breakdown boundary, the Bird breakdown surface (Bird [11]), was obtained from the CFD solution of the expanding plume. A breakdown surface defined the outer extent of the RCS plume continuum flow region where the Navier–Stokes equations are applicable. Flow properties from the CFD solution at the breakdown surface location were then used as an inflow boundary for a molecular simulation applied by the DSMC technique. This uncoupled CFD–DSMC approach of Lumpkin et al. [47] and Rault [64] provided high fidelity estimates for pressure and heat loads on the Mir space station from close proximity Shuttle Orbiter RCS engine firing during docking maneuvers.

The Germans (See Rosenhauser et al. [68].) have also used an uncoupled CFD–DSMC technique to predict flow from an expanding thruster plume. An experimental study in the Deutsches Zentrum für Luft- und Raumfahrt (DLR) high vacuum plume test facility, Simulationsanlage für Treibstrahlen Göttingen (STG), simulated plumes from a 0.5 N conical thruster into a high vacuum background environment. For the numerical simulation of the nozzle and plume flow, CFD was performed to the nozzle exit for the high Reynolds number case and inside the nozzle otherwise, where the local Knudsen number, Kn , was less than 0.05. The interface between the CFD and DSMC was uncoupled for these calculations; that is, information was allowed to pass only from the CFD to the DSMC solution domain, which is appropriate for such an expanding flow. Comparison between the experiment and numerical simulation was generally good; however, a more accurate modeling of the nozzle wall temperature distribution may decrease the difference between the two [68].

Not only are RCS thrusters a source of gas impingement for vehicles in orbit, but venting and outgassing from the vehicle surface pose a contamination threat to the vehicle. Rault and Woronowicz [66] have applied the DSMC technique to analyze surface contamination on the halogen occultation experiment (HALOE) telescope optics on the Upper Atmospheric Research Satellite (UARS) from surface outgassing, equipment venting, and attitude thruster firing while in orbit. Molecules from surface sources were introduced into the DSMC computational domain as either emitting gases with no bulk velocity or as drifting Maxwellian free jets. The study provided simulations of the local contamination field and surface contamination on the UARS HALOE instruments, which showed that estimates based on engineering codes were too conservative.

RCS impingement and surface outgassing studies such as those described above show the usefulness of the DSMC technique in analyzing flow about vehicles in orbit in the free molecular flow regime. The DSMC technique has almost become a necessary tool for the spacecraft designer in determining contamination, pressure, and heat loads for space vehicles in orbit. Although engineering codes that predict contamination fields about satellites with line-of-sight view factors using approximations such as those given by Dettleff [19] provide a first order estimate of the effects of the plume impingement contamination, DSMC molecular simulations provide a more accurate estimate of the contamination flow field. Intermolecular collisions and multiple surface interactions are modeled directly with DSMC, as opposed to the ad hoc models for the return flux used in engineering codes. With DSMC techniques and computational resources improving, accurate DSMC calculations of the flow field and surface contamination about geometrically complex satellites in orbit can now be performed with short turnaround times on desktop workstations (Rault and Woronowicz [66]). A deficiency with the method presented by Rault and Woronowicz [64] and [66], however, is that accuracy in the continuum flow region adjacent to the outgassing surface or thruster plume was limited because the DSMC technique required excessive computational resources to provide a complete representation of the flow field in those regimes.

1.2.2 Rarefied Flow Regime

In addition to studies of configuration-specific RCS jet interactions in the rarefied flow regime described above in Section 1.1, some recent generic experimental and computational studies of rarefied flow interacting with continuum jets have been accomplished.

These studies were performed to increase fundamental understanding of the flow physics and resultant surface effects from jet interaction with a rarefied free stream flow on simple shapes. The experiments also provide a database to validate existing and developing computational techniques, which can then be applied to obtain jet flow field interactions for the more complex flight configurations and flight conditions.

1.2.2.1 Experimental Studies

A French experiment performed in the SR3 wind tunnel of the Centre National de la Recherche Scientifique (CNRS) in Meudon, France (Allègre and Raffin [3] and Allègre et al. [4]) models a jet interaction in a corner to simulate effects such as those caused by an RCS jet near a wing-fuselage juncture. The model used in the experiment is shown in Figure 1.1. Two sharp leading edge flat plates oriented perpendicular to each other form a corner. The horizontal plate has an orifice oriented normal to its surface through which a supersonic jet is injected. Both plates, at zero incidence to a rarefied Mach 20 N_2 free stream, were instrumented with pressure orifices. Surface pressure distributions and surface oil flow visualizations at various free stream and jet flow conditions from the experiment are presented by Allègre and Raffin [3].

Also, the British have recently performed jet interaction experiments using generic models in the Low Density Nitrogen Tunnel (LDT) at the Defence Evaluation and Research Agency (DERA) in Farnborough, United Kingdom (Gilmore and Warburton [28], Gilmore [27], and Warburton [88]). Gilmore and Warburton [28] experimentally and numerically studied the jet interaction flow about an 8° sphere cone with an axisymmetric annular jet. The sphere cone was also tested with a circular disk at the jet injection

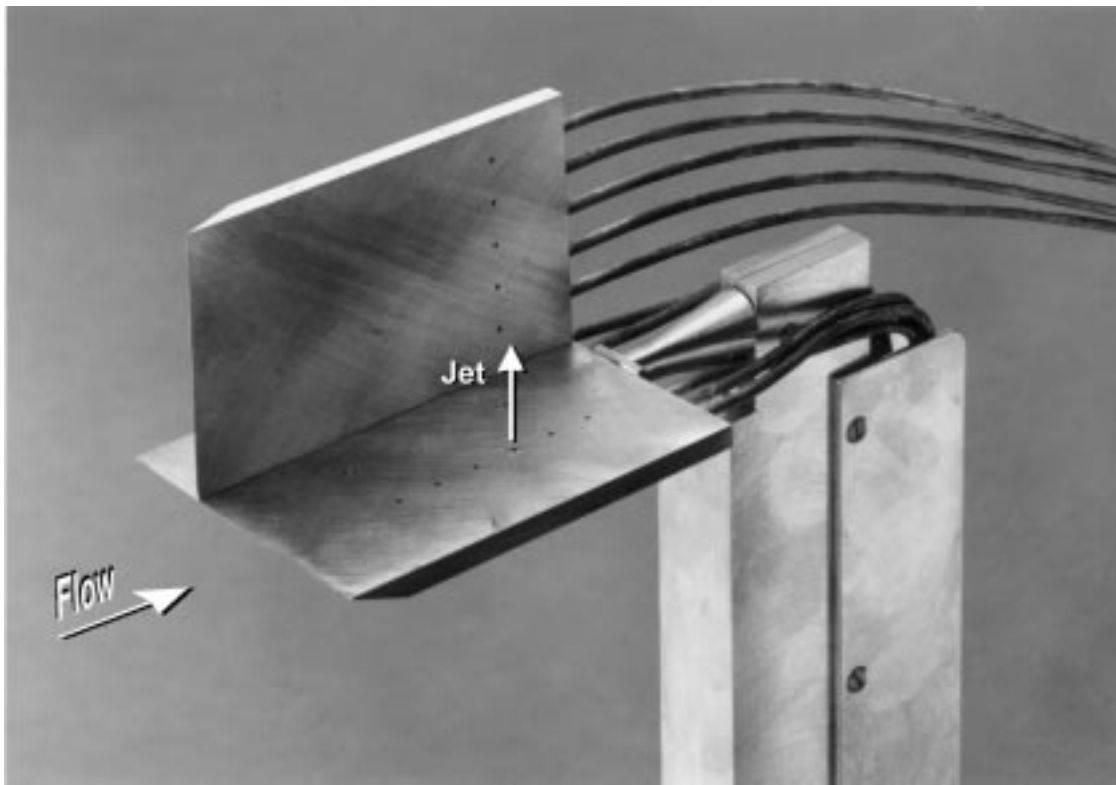


Fig. 1.1. Jet interaction corner flow model of Allègre and Raffin [3].

location, which represented a jet-type obstruction to the flow. CFD was applied to both configurations and DSMC was applied to the configuration with the circular disk attachment. It was determined that flow solutions from both axisymmetric CFD and DSMC simulations did not adequately model all of the flow and surface effects produced during the experiment. CFD provided good agreement in the high density vortical flow region upstream of the circular ring, and the DSMC solution was in good agreement elsewhere in the low density flow regions. These results are expected since the flow about the configuration is mixed; that is, it consists of a low density, rarefied flow over the forward portion of the body from the nose to a high density, vortical flow region in the vicinity of the circular ring protuberance. The Navier–Stokes equations, as applied by CFD, are appropriate to describe the flow field in the high density region; elsewhere in the rarefied flow region, the computational grid was sufficiently resolved to produce an accurate molecular simulation by the DSMC technique.

Additionally, Warburton [88] experimentally studied jet interactions with a sharp leading edge flat plate configuration in the LDT. Heated nitrogen gas was expanded to provide a free stream flow at a nominal Mach number of 9.84, static temperature of 65K, and static pressure of 5.4 Pa. The interacting jet was expanded from a plenum to a sonic condition at the nozzle exit and released perpendicular to the flat plate surface. As with the experiment of Gilmore and Warburton [28], the experiment of Warburton [88] offers an opportunity to study a jet interaction with a combination of both CFD and DSMC solution techniques because the free stream flow is rarefied and the interacting jet is continuum. However, the experiment of Warburton provides a three-dimensional

jet interaction rather than the axisymmetric jet interaction that was studied in the experiment of Gilmore and Warburton [28].

1.2.2.2 Computational Studies

Some of the experiments described in Section 1.2.2.1 have provided test conditions for numerical studies. Wilmoth and Tartabini [95] and Tartabini et al. [82] applied the DSMC technique to the French corner flow jet interaction experiment. For the simulation, the jet flow at the nozzle exit was “modeled as a circular disk contained within the horizontal surface across which molecules are injected by sampling from a streaming Maxwellian distribution” (Wilmoth and Tartabini [95]). Molecules were ejected from the surface with an average velocity and temperature based on calculated nozzle exit conditions. Results of the DSMC study showed the simulation produced higher jet induced wall pressure than was measured during the experiment. A similar modeling of jet flow was chosen by Rault et al. [65], Shane et al. [76], and Shane [77] for the DSMC simulation of both the Magellan and MGS during actively controlled planetary aerobraking maneuvers. If the jet plume flow near the nozzle is in a continuum state, application of the DSMC technique to the near nozzle exit flow is not appropriate. Instead, a mixed solution methodology, which captures the continuum flow by a CFD solution and the rarefied flow by a DSMC simulation, would yield the proper flow field solution.

Recent research efforts have focused on developing hybrid CFD and DSMC techniques to provide solutions for mixed flow regimes. Wadsworth and Ervin first developed a one-dimensional scheme [85], which was applied to a rarefied normal shock wave, then

a two-dimensional scheme [86], which was applied to rarefied flow through a slit. Issues such as the interface location, CFD to DSMC coupling techniques, and the extension of the technique to three-dimensional problems are discussed. Hash and Hassan [36] have also developed a hybrid CFD–DSMC solution technique to analyze the flow about an axisymmetric blunted cone configuration. Merits of a coupled and an uncoupled method to solve the flow field were compared, and Hash and Hassan [36] concluded that for the blunted cone configuration, the decoupled CFD–DSMC solution technique is appropriate. Garcia et al. [26] have studied flow about a microscopic sphere by embedding a fine scale DSMC patch within a CFD grid to study the mapping of coarse scale grid with fine scale grid properties through buffer cells. The most ambitious hybrid CFD–DSMC technique, however, has been accomplished by Roveda et al. [70] and [69]. The technique allows non-equilibrium flow regions to be embedded, and move in a time accurate manner, within an inviscid continuum flow regime. Roveda et al. [70] discuss the non-equilibrium–continuum interface location, frequency of coupling, and regridding to follow unsteady patch movement, and apply the technique to a two-dimensional unsteady rarefied slit flow [69].

Depending on the type of mixed continuum–non-continuum flow field, one of three interfaces between the regions can be used [70]: uncoupled, weakly coupled, and strongly coupled. If flow field information travels in the downstream direction only, an uncoupled technique is applicable, for example, the flow of an expanding plume moving downstream from the nozzle exit. Therefore, an uncoupled solution, with the continuum and rarefied regions uncoupled at the proper interface location, is sufficient to describe the entire flow

field. As discussed previously, Lumpkin et al. [47], Rault [64], and Rosenhauser et al. [68] have produced solutions for expanding plume flows using the uncoupled technique.

Recently, Glass and LeBeau [30] and Glass [29] have applied an uncoupled technique to a study of jet interactions with the geometric configuration based on the experiment of Warburton [88] and have obtained three-dimensional numerical results for the experimental test conditions. Although the technique was demonstrated and solutions were presented in the studies, no experimental results were available for comparison.

1.2.3 Continuum Flow Regime

Jet interactions for aeronautical applications have been most extensively studied for flows in the continuum regime. Cross-flow jet interactions are used in aeronautical vehicle power plants to mix fuel either in an internal combustion or turbojet engine, and more recently in research supersonic combustion ram jet (SCRAMjet) engines. The lateral transfer of fuel through an injector into air forms a mixture, which is compressed and ignited to produce power (Eastop and McConkey [20]). For hypersonic flight, cross flow interaction has been studied to define fuel mixing efficiency in SCRAMjet engines by Fuller [24]. Also, control devices on some aeronautical vehicles are cross-flow jets. Some high performance fighter aircraft use cross-flowing jets for lateral momentum transfer to increase maneuverability. The AV-8B Harrier can vector its thrust to rapidly change flight path. Vectored thrust is planned for use with the next generation fighter aircraft to decrease take-off distance and increase in-flight maneuverability (See Flinn [23] and Farley [22]). Thrust vectoring flight control may soon be available for commercial aircraft (Gal-Or [25]). High-speed interceptor-type missiles may use jet interaction for steering

control. At high-speed free stream conditions, a cross-flow jet produces both a “direct” thrust from the jet momentum flux and an “indirect” thrust as the jet interaction affects the local surface pressure distribution (Ward [89]). Amplification factor correlations are available for some high-speed continuum jet interactions (Spaid and Cassel [79]), but the correlations are geometry specific.

To complete the general discussion of jet interactions, a few types of low speed interactions are briefly discussed. Some more ordinary applications of cross-flow jet interactions are to transfer mass and heat into the atmospheric and aquatic environment. For example, the fireplace in a home, municipal trash burning, or burning coal or oil by heavy industry produce heat and smoke. The smoke is discharged as a low speed plume from a chimney or smokestack and mixes with and is convected away by the surrounding atmosphere. Heat is also transferred into the environment in water plumes. For example, coolant water, after being circulated through the heat exchanger of an electric power plant steam condenser, increases in temperature and in some cases is discharged as a low speed plume into a large moving body of water to transfer heat.

1.3 Summary

All of the above applications of cross-flow jet interactions have a common attribute. Either by experimentation, application of the integral or differential conservation laws, engineering approximations, or other numerical techniques, a base of information can be obtained to predict the mixing behavior and the effect of the interacting (or for free expanding, non-interacting) jet or plume or on the surrounding medium. In the continuum regime, wind tunnels, water tunnels, engineering approximations and

codes, and CFD adequately represent the flow process and its effects, which can then be factored into specific design criteria. In the free molecular regime, vacuum chamber experiments, collisionless flow analysis, and recently, DSMC simulations describe the expanding flow and surface impingement with confidence. Plume and jet interaction flow in the free molecular and continuum regimes have been studied extensively. See, for example, Dettleff [19] and Spaid and Cassel [79], respectively, for review papers on the subjects. However, jet interaction with a rarefied hypersonic flow has been less studied, and a database of fundamental knowledge of the phenomena and how best to quantify jet interaction effects for specific configurations is needed.

Chapter 2

Uncoupled CFD–DSMC Technique

As discussed in Chapter 1, a need exists to accurately model and understand effects of jet interactions in the rarefied flow regime for the next generation space vehicles, upcoming planetary exploration probes, and other vehicles that use active control because they will require RCS to maintain flight stability during atmospheric entry or aerobraking maneuvers. The present research effort is intended to develop a numerical strategy that can be applied to geometry specific problems and provide fundamental understanding of the interaction between a continuum jet and a rarefied flow for these problems.

2.1 Jet Interaction Flow Field

A jet interacting with a rarefied flow field consists of mixed flow regimes: an outer rarefied region, an embedded inner continuum jet plume region, and an interaction zone between the two regions. A solution to this mixed flow requires the use of both the CFD and DSMC techniques with an appropriate interface. Theoretically, a molecular simulation applied by the DSMC technique to the entire interacting flow field, including the continuum jet, should yield an accurate simulation of the resultant flow. However, because the jet flow begins as a high density, continuum gas in a plenum chamber and remains a continuum gas as it initially expands from the nozzle exit into the low pressure

rarefied region, implementation of the DSMC technique to the entire flow field is limited by current computer technology and DSMC algorithms. So accurate modeling of the higher density jet flow by a three-dimensional molecular simulation requires computational resources beyond the computer memory limits of today's supercomputers because grid resolution needed for the DSMC technique is of the order of the local mean free path. Therefore, for the present method, the continuum portion of the expanding jet flow field is described using CFD, and the other portions of the flow are modeled using DSMC.

2.2 CFD–DSMC Uncoupling at the Breakdown Surface

State-of-the-art hybrid flow solution techniques are presently being developed, which apply CFD and DSMC in applicable regions to produce solutions of mixed continuum and rarefied flow fields (See Section 1.2.2.2.). Roveda et al. [70] discuss issues associated with coupling the continuum and rarefied regions using uncoupled, weakly coupled, and strongly coupled techniques. For the present solution methodology, an uncoupled hybrid technique will be developed to simulate the jet interaction with a rarefied flow. This technique is appropriate for situations where the downstream jet flow is unaffected by the upstream region; that is, information is passed only in the expanding flow direction—from the high pressure region outward. For this circumstance, a CFD jet flow solution can then be used as an inflow boundary condition for the DSMC, which then applies a molecular simulation to describe the rarefied and interacting portions of the flow field. However, to implement such an uncoupled hybrid flow solution technique, a boundary must be established between the CFD and DSMC solution domains, which

allows the CFD solution to capture the continuum region of the plume that is relatively unaffected by the interaction.

Several methods exist to establish a boundary between the continuum and rarefied regimes, which have been discussed by Boyd et al. [13] and Bird [11]. Boyd et al. [13] use a gradient length local Knudsen number, $Kn_{GLL} = \lambda/L$, with the characteristic length, $L = \rho/\nabla\rho$, based on the local density gradient to determine the boundary between the continuum and rarefied regimes. Their study [13] concludes that for compression regions with large density gradients, such as near shock waves and stagnating flow, if $Kn_{GLL} > 0.05$, the continuum approach breaks down. Bird [11], however, defines a continuum breakdown parameter for expanding flow. Gradients in the macroscopic flow properties are sustained by collisions between molecules. As the number of collisions decreases, these gradients cannot be maintained. The Bird breakdown parameter, P , provides a numerical value, which is a measure of the number of molecular collisions in a characteristic time for an expanding flow. For $P > 0.02$, the local temperature departs from the continuum theory because the molecular collision frequency is too low to provide a local equilibrium condition [11].

Because the boundary defined by Boyd et al. [13] is based on local density gradient for flow compression and the Bird breakdown parameter is based on flow expansion considerations [11], the Bird breakdown parameter is used in the present study to determine the interface boundary between the expanding jet plume and the interaction with the rarefied flow field. Given a three-dimensional expanding flow solution, a Bird breakdown surface (Bird [9] and [11]) can be obtained. The breakdown surface provides a natural boundary between continuum and rarefied flow regions and, by varying the value of the

surface breakdown parameter, the applicable range of the Navier–Stokes equations in an expanding flow field can be shown.

To employ the Bird breakdown surface as a parameter to define the extent of the expanding jet flow when applied to a jet interaction, it will be shown that the appropriate value of breakdown parameter depends on both the jet and free stream flow conditions. The difficulty of the application is determining the breakdown surface that ensures the jet plume flow expands outward only and is not distorted by the interaction, thus allowing the jet and interaction to be uncoupled. Such a method will optimize the use of both the CFD and DSMC numerical techniques for a given problem without an iterative step to update the jet flow properties at the boundary. The present research provides a set of guidelines to define the proper breakdown boundary for this type of jet interaction in the transitional–rarefied regime. Numerical resources can then be best utilized to numerically simulate the jet interaction flow field by employing continuum and molecular flow analyses in the flow region where most appropriate.

Other approaches have been proposed and employed to numerically model and study a continuum jet interacting with a rarefied free stream. CFD and DSMC were applied separately to an experiment of an axisymmetric conical configuration with an annular ring attached to the surface that simulated the jet plume as solid obstruction to the flow (Gilmore and Warburton [28]). A comparison between the numerical and experimental results showed that both the CFD and DSMC numerical results lacked a complete description of flow structures and the surface effects seen experimentally. In addition, the simulation was performed on an axisymmetric model, which is not representative of three-dimensional interactions for complex geometric configurations.

Wilmoth and Tartabini [95] and Tartabini et al. [82] took another approach with their application of the DSMC technique to jet interaction corner flow studies. The jet was approximated as a molecular inflow boundary at the nozzle exit on the geometric surface of the flat plate. Although the grid cells used for the study were dimensioned about twice the free stream mean free path, the jet core, which has a much smaller mean free path, was not adequately resolved because of considerable computational requirements. Flow physics of the continuum portion of the jet may not be properly modeled by an insufficient number of cells because gradients and local collision rates are not defined accurately by poor grid resolution. Also, the macroscopic properties of the flow in the vicinity of the continuum jet core may influence any subsequent surface collisions of the molecule, which are used to calculate surface pressure, skin friction, and heat transfer.

An approach of combining CFD and DSMC similar to that proposed for modeling the jet interaction for the present method has been applied to study free expanding plume impingement (Lumpkin et al. [47] and Rault [64]). The jet plume for the free expanding plume impingement was first modeled using CFD. A breakdown surface and inflow boundary conditions for the DSMC technique were obtained from the CFD solution, and DSMC was applied to obtain a molecular simulation for the remainder of the computational space. Additionally, no significant free stream was present to interact with the expanding plume. Moreover, these studies (Lumpkin et al. [47] and Rault [64]) defined the extent of continuum flow at a plume breakdown surface of breakdown parameter value of 0.05. Rault [64] states the use of this breakdown value is valid because it is based on experimental data; however, Bird [11] suggests that breakdown parameter

values less than or equal to 0.02 be used to define the extent of the continuum regime for an expanding flow. Note that the larger the numerical value of the breakdown parameter the more rarefied the plume flow field. Consequently, the breakdown parameter value given by Bird [11] provides a more conservative evaluation of the continuum regime than that of Rault [64].

2.3 Numerical Methods

An overview of the uncoupled CFD–DSMC technique proposed for the present study of the mixed flow associated with jet interactions in the rarefied regime was discussed in the previous section. Presented in this section is a general discussion of the the CFD and DSMC numerical methods individually and the specific computer programs used to apply the numerical techniques for this study.

2.3.1 Computational Fluid Dynamics

Computational fluid dynamics (CFD) is a numerical approach employed to determine the motion of a continuum, Newtonian fluid. The Navier–Stokes equations, which describe the continuum fluid motion, are applied to a physical space that is divided into a grid of cells or volumes called the computational domain. Boundary conditions and specific algorithms are applied to the computational domain and allow solutions to be obtained for many flow situations, ranging from, for example, internal pipe flow to external hypersonic flow about a flight vehicle. Presented below is a brief history of the development of the governing set of equations, which describe the fluid motion, and numerical techniques used to solve the equation set.

2.3.1.1 Historical Perspective

CFD, as a discipline, enables solutions of the equations of fluid motion to be obtained using various numerical methods, and its history is linked to both the mathematical development of the equations and to the more recent and ongoing advancements in computational methods available to solve the equations. Because the equations and solution methods are so closely tied for this subject, presented in this section is a brief history of both.

The following historical account of the development of the theory and solutions of the equations of motion from the earliest description of fluid mechanics to the start of the 20th century is taken from the text by White [92]. The first exact solution to a fluid mechanics problem was given by Archimedes (~ 200 B.C.) and was developed as a result of his observations of buoyancy. The Romans, simultaneously, were building their city water supply system, which incorporated intuitive knowledge of flow resistance, but no mathematical relationships were derived to describe the fluid resistance in the system.

Leonardo da Vinci, in about 1500, developed the mass conservation equation for one-dimensional, incompressible, viscous fluid flow. His notes on the subject of fluid mechanics contained sketches and descriptions of various flow phenomena such as wave motion, free jets, bluff body eddy formation, etc. Two centuries later, Edme Mariotte, in the first wind tunnel, measured drag with a model balance system and directly studied friction from a fluid. This work was published in 1686 as the text, “*Traité du Mouvement des eaux.*” A year later, Sir Isaac Newton in his “*Principia*” proposed that the cause of viscous fluid behavior is a “ ... lack of lubricity in the parts of the fluid ... [which] is

proportional to the [fluid] velocity ...” [92]. This hypothesis leads to the linear law of viscosity and is why most common fluids are called *Newtonian* in honor of his insight into the viscous behavior of fluids.

In 1738, Daniel Bernoulli demonstrated that for inviscid flow, fluid acceleration is proportional to pressure gradient; and Leonhard Euler, in 1755, further refined Bernoulli’s observations and derived the so-called Bernoulli’s equation, which describes the flow properties of an inviscid fluid along a streamline.

The addition of viscous terms to Euler’s inviscid equations was the next significant step to define the full set of equations of fluid motion. In the early to mid 19th century, Navier, Cauchy, Poisson, St. Venant, and Stokes added friction by including viscous terms to the Euler inviscid equations. However, Stokes was the only one of the five to use the first coefficient of viscosity, μ , in his mathematical description, and the resulting equation set, in part bearing his name, are called the Navier–Stokes relationships. In general, these non-linear partial differential equations are not amenable to a direct analytical solution, except for some particularly simplified cases, because they are mathematically difficult. Therefore, the equation set, although complete in the mid 19th century, was of little use to the hydraulicists of that era.

The next major step in mathematically describing viscous fluid flow, proposed by Ludwig Prandtl in 1904, was the boundary-layer theory. In his approach, an outer flow is described approximately by the inviscid Euler equations and matched as a boundary condition to a viscous, near wall flow, which is defined by the boundary-layer equations, a simplified subset of the Navier–Stokes equations. Although the method works adequately for attached flows, it does not work for flow with regions of separation where the parabolic

nature of the boundary-layer equations does not allow information to pass in an upstream direction. The significance of Prandtl's boundary-layer theory was that it permitted the physics of the flow to be better modeled; thus, a greater number of fluid flow problems could be solved analytically.

Although general analytical flow field solutions about an arbitrary body by the full Navier–Stokes equations are still not possible because of the complexity of the equation set, the arrival of numerical techniques, which allow approximations of the Navier–Stokes equations, and high-speed digital computers with which to solve them, enable accurate continuum flow simulations of a Newtonian fluid to now be readily accessible. To better understand the equation solution techniques, Anderson et al. [6] provide a comprehensive historical perspective of the development of these algorithms from the first schemes, which required tedious hand calculations until about the mid 1970's, where modest supercomputers were available. Some of the highlights from their textbook are included next.

To solve Laplace's equation and determine the stress distribution in a dam, Richardson in 1910, devised a point iterative scheme, which is thought to be the first decisive numerical solution method. Also, he distinguished between problems requiring relaxation techniques and marching schemes. Leibmann improved Richardson's method in 1918, which decreased convergence time for solutions of Laplace's equation.

In 1928, mathematicians Courant, Friedrichs, and Lewy studied the uniqueness and existence of numerical solutions and developed what is now known as the CFL condition, which provides a criteria to determine the stability of a numerical technique

when applied to hyperbolic partial differential equations. The CFL condition is widely used to assess the time step size for current, state-of-the-art CFD algorithms.

Specifically for fluid dynamics problems, Southwell, in 1940, developed an iterative scheme for hand computing flow fields, and, in 1955, Allen and Southwell applied the technique to solve the incompressible, viscous flow over a cylinder. Moreover, during World War II, at Los Alamos National Laboratory, von Neumann developed methods for analyzing the stability of a time-marching scheme to predict high energy detonation shock waves for the war effort. Von Neumann's stability analysis was published in 1950 by O'Brien, Hyman, and Kaplan. Additionally in 1950, von Neumann and Richtmyer produced a scheme that employed artificial viscosity to capture shocks, which was first-order accurate and was the basic algorithm for early inviscid, compressible flow codes. Since the early weapons type, von Neumann–Richtmyer algorithms, there has been a steady increase in the number and order of accuracy of emerging schemes.

In 1954, Lax, with the governing equations written in the conservative form, developed a shock capturing scheme, and, in 1960, Lax and Wendroff produced a second-order scheme to calculate shock waves in a flow by adding numerical damping with artificial viscosity similar to the method used in the von Neumann–Richtmyer algorithms. In the late 1960's, MacCormick developed a second-order predictor-corrector scheme and was able to better predict flow fields with discontinuities and embedded shocks than the standard Lax–Wendroff algorithm.

Chapman [16], in 1979, presented the AIAA Dryden lecture, in which he summed up the state-of-the art at that time. Given next is a brief synopsis of Chapman's lecture. Although the first published numerical flow simulation was a weather prediction

accomplished on an ENIAC computer by Charney, Fjörtoft, and von Neumann in 1950 on a 15 x 18 grid, aeronautical applications have had the most impact on the overall development of CFD.

There are two primary motivations to exploit CFD for aeronautical applications. First, it can provide flight condition predictions not attainable experimentally in a wind tunnel. CFD predictions do not suffer with sting interference effects, free stream non-uniformities that effect transition to turbulence, and the dependence of flow separation and transition on flight vehicle motion. Secondly, Chapman [16] predicts that it will become economically cheaper to produce CFD simulations than experiments because computers will be less expensive and faster, algorithms more efficient, and model fabrication and wind tunnel testing will be more costly. Generally, these predictions are true; however, baseline experiments provide much credibility to CFD techniques, and in retrospect, wind tunnels still provide most of the aerodynamic data.

According to Chapman [16], CFD development can be categorized into four stages. Stage I, the linearized inviscid stage, is commonly called “panel methods,” which solve the potential wave equation on numerous surfaces that define a vehicle. In the 1960’s, 3-D aircraft analyses were performed using stage I techniques.

The next stage of CFD development, stage II, is the solution of the non-linear inviscid equations where the viscous terms of the Navier–Stokes equations are neglected. Stage II calculations are performed by so-called Euler codes. Primarily, most stage II calculations were accomplished at either transonic and hypersonic flow conditions. The first transonic solution for a lifting airfoil was presented in 1970 by Magnus and Yoshihara using a time dependent explicit technique. Also, during this time, hypersonic

Euler solutions were produced using the Lax–Wendroff “shock-capturing” technique to predict aerodynamics for the shuttle Orbiter during the hypersonic portion of an entry trajectory.

Stage III CFD techniques produce solutions for the Reynolds averaged Navier–Stokes (RANS) equations with all viscous terms included. The first such simulation, reported by Li in 1974, was of a steady, laminar flow about a body of revolution at angle-of-attack. In 1977, Levy reported the first unsteady solution of buffeting flow on a transonic airfoil. The inaccuracy of stage III CFD is in turbulence modeling where zero-, one-, or two-equation models are employed to describe turbulent flow behavior. Although no universal model is available for all flow situations, stage III turbulence models are still exercised in current state-of-the-art CFD.

A numerical technique, which is not discussed by Chapman [16], but bridges the gap between the stage III RANS, discussed above, and stage IV direct numerical simulation (DNS), discussed below, is the large eddy simulation (LES). Rather than simulating turbulence at the micro-scale, which involves a “large range of space and time scales (Schumann [75]),” the LES captures larger scale eddy phenomena with subgrid scale models to remove isotropic turbulent and diffusive subscale energy that cascades from the large scale features without the computational overhead of employing a micro-scale resolved grid. LES has been applied to flows from high Reynolds number homogeneous turbulence to channel and atmospheric boundary layers (For example, see Schumann [75], Speziale [80] and Zhang et al. [97].).

Stage IV CFD simulations produce turbulent flow simulations based on first principles using a DNS of the full Navier–Stokes equations. By refining the grid to the

Kolomogorov micro-scale, the turbulent eddies of a flow can be simulated. Early advances in stage IV CFD were from atmospheric simulation models in the 1960, which used Prandtl and von Kármán type eddy viscosity and mixing length models. Deardorff, in 1970, is credited with producing the first 3-D turbulent eddy simulation of a channel flow and planetary atmospheric flow using stage IV techniques. To adequately resolve turbulent flow on a flight vehicle, however, is still beyond computational capability. This technique is waiting to exploit computers with large memory capacity to perform such turbulent flow simulations.

Since the early 1970's, a tremendous amount of research on CFD techniques has been accomplished and the capabilities of each new generation of supercomputers has increased proportionally. An important aspect of the new techniques to solve the Navier-Stokes equations has been the introduction of higher order schemes for predicting compressible flows, which, rather than spreading a discontinuity such as a shock wave over several grid points as with previous methods, are able now to calculate sharp, oscillation free shock waves.

The most recent advances in CFD have been in the solution of compressible flow problems, and Hussaini et al. [38] have compiled an anthology of higher-order computational schemes for obtaining solutions for these problems. In particular, upwind and high-resolution techniques, which evolved from the early 1980's until the mid 1990's, were reported by computational scientists at the Institute for Computer Applications in Science and Engineering (ICASE) located at the NASA Langley Research Center and

are published as a collection of the original papers in the anthology. Presented subsequently are a few of the many events, which historically account the path to the current state-of-the-art CFD compressible flow solvers.

As discussed previously (See the text by Anderson et al. [6].), early compressible flow solution techniques added artificial viscosity terms to the governing equations to capture shock waves over several grid points, not as a discontinuity, but as a smeared shock. This shock smearing affects the adjacent numerically determined flow properties.

To more accurately define these discontinuities in the flow field, research was begun in the early 1980's on "high-resolution schemes." Two different approaches were taken: the first, by Boris, was called the Sharp and Smooth Transport Algorithm (SHASTA) and used a flux-corrected transport (FCT) method in a two step prediction-correction cycle to achieve second-order accuracy; the second, by van Leer was a modification to the Lax–Wendroff scheme, where he added flux limiters and high-order reconstruction to estimate flux values of nearby cells, which lead to his Monotone Upwind Scheme for Conservation Laws (MUSCL). This effort by van Leer also prompted other techniques that limit oscillation near a discontinuity by various higher order reconstructions and gave rise to the Essentially Non-Oscillatory (ENO) schemes.

At the same time, Roe began to investigate an approximate Riemann solver that used the technique of flux-difference splitting to divide the information passed through the grid into parts, one associated with waves moving forward and the other moving backward through the grid. Also, during this time, Harten formulated his Total Variation

Diminishing (TVD) scheme that he later combined with the ENO method for multi-dimensional applications that became known as the Total Variation Bounded (TVB) scheme.

The ICASE environment, which led to greater understanding of techniques to solve the compressible flow equations, also presented an opportunity for the development of industry standard CFD codes. One of these codes, CFL3D, resulted from a collaboration of ICASE scientists, one of whom was Walters. Later, Walters was instrumental in the development the GASP code [2] used in the present study.

2.3.1.2 Governing Equations

The set of equations, which govern the motion of a continuum, Newtonian fluid are derived as a consequence of applying the conservation of mass, momentum, and energy to a control volume about a small fluid element. In this section, the integral form of the equations of motion are presented for flow of a single species for completeness (For more comprehensive details, see text by White [92] or Kundu [43].).

The time rate of change of mass in a fixed volume equals the sum of the mass flow into and out of the fixed volume. This statement describes the conservation of mass, which, in integral form, can be written as:

$$\int_V \frac{\partial \rho}{\partial t} dV = - \int_A \rho \mathbf{u} \cdot d\mathbf{A} \quad (2.1)$$

A statement of the conservation of momentum is obtained by applying Newton's second law to the small control volume. That is, the sum of all forces acting on the volume and the net flux of momentum through the surface of the volume equals the time rate of change of its momentum (which equals the mass of the volume times the acceleration). Acting on the volume are body and surface forces: (1) Body forces are those produced by a conservative field such as a gravity, an electrostatic, or a magnetic field; (2) Surface forces are those acting on the boundary of the volume such as normal forces (pressure forces) and shear stress (frictional forces). In integral form, the conservation of momentum can be written as:

$$\int_V \frac{\partial}{\partial t}(\rho u_i) dV + \int_A \rho u_i u_j dA_j = \int_V \rho g_i dV + \int_A \tau_{ij} dA_j \quad (2.2)$$

where index, or Einstein, notation is used for its compactness.

Similarly, a statement of the conservation of energy, the first law of thermodynamics, for a small control volume can be expressed as the time rate of change of energy stored, which equals the sum of all work done and heat added to the volume. This relationship, written in integral form, is:

$$\frac{D}{Dt} \int_V \rho \left(e + \frac{u_i^2}{2} \right) dV = \int_V \rho g_i u_i dV + \int_A \tau_{ij} u_i dA_j - \int_A q_i dA \quad (2.3)$$

where $\frac{D}{Dt}$ is the substantial derivative.

Closure of Equations 2.1, 2.2, and 2.3 is obtained by decomposing the shear stress tensor, τ_{ij} , into normal and tangential components and associating them with pressure, shear stresses, and spatial derivatives of the velocity vector; relating the internal energy and heat flux vector to the temperature with the constant volume specific heat, C_V , and thermal conductivity, k , respectively; and using a state equation such as the perfect gas law, $P = \rho RT$, to interrelate thermodynamic variables.

Finally, as a consequence of the second law of thermodynamics, which requires entropy of irreversible processes to increase, the coefficient of viscosity, μ , and thermal conductivity, k , are positive.

2.3.1.3 Solution Method

CFD for this study is provided by the General Aerodynamic Simulation Program (GASP) (McGrory et al. [49] and AeroSoft [2]). A commercially available software product of AeroSoft, Inc., GASP, is a three-dimensional finite-volume CFD algorithm, which solves the time-dependent, Reynolds averaged Navier–Stokes (RANS) equations. Also, steady, one-dimensional, two-dimensional, axisymmetric, thin-layer, parabolic space marching, and Euler subsets of the RANS are solved by GASP. The equation set solved by the code is presented in the technical reference section of the user manual [2] and is given in this section. The finite volume formulation of the GASP code is for an unsteady, multi-dimensional, multi-species, reacting chemistry model. By ignoring unneeded terms, the equation set is simplified to match the specific problem.

Although not presented in compact vector form in the previous section, the Navier–Stokes equations for the finite volume formulation of GASP are first written in integral form as:

$$\underbrace{\frac{d}{dt} \int_V \mathbf{Q} dV}_{\text{Time Derivative}} + \underbrace{\int_A [\mathbf{F}(\mathbf{Q}) \cdot \hat{\mathbf{n}}] dA}_{\text{Inviscid Fluxes}} = \underbrace{\int_A [\mathbf{F}_v(\mathbf{Q}) \cdot \hat{\mathbf{n}}] dA}_{\text{Viscous Fluxes}} + \underbrace{\int_V \mathbf{S} dV}_{\text{Source Term}} \quad (2.4)$$

where the terms of the equation are separated by the braces from below and designated by their function.

A cell-averaged, finite-volume formulation for Equation 2.4 with the volume denoted as V , a cell face area as ΔA , and with the application of the chain rule to obtain the time derivative of primitive rather than conserved variables can be written as:

$$V \left(\frac{d\bar{\mathbf{Q}}}{d\mathbf{q}} \right) \frac{d\mathbf{q}}{dt} + \sum_A (\mathbf{F} \cdot \hat{\mathbf{n}}) \Delta A = \sum_A (\mathbf{F}_v \cdot \hat{\mathbf{n}}) \Delta A + V \bar{\mathbf{S}} \quad (2.5)$$

The conservative variable vector, \mathbf{Q} , and primitive variable vector, \mathbf{q} , respectively, are:

$$\mathbf{Q} = \left\{ \begin{array}{cccccccccccc} \rho_1 & \rho_2 & \dots & \rho_N & \rho u & \rho v & \rho w & \rho_1 e_{n_1} & \rho_2 e_{n_2} & \dots & \rho_M e_{n_M} & \rho e_0 \end{array} \right\}^T \quad (2.6)$$

and

$$\mathbf{q} = \left\{ \begin{array}{cccccccccccccc} \rho_1 & \rho_2 & \dots & \rho_N & u & v & w & e_{n_1} & e_{n_2} & \dots & e_{n_M} & p \end{array} \right\}^T \quad (2.7)$$

The variables of the vectors represented by Equations 2.6 and 2.7 are the unknowns that describe the flow field. Either vector can be used, but for simplifying some calculations, GASP seeks solutions for the primitive variables.

The next vector in Equation 2.5 is the inviscid flux vector, $\mathbf{F} \cdot \hat{\mathbf{n}}$, which is expanded as:

$$\mathbf{F} \cdot \hat{\mathbf{n}} = \left\{ \begin{array}{c} \rho_1(\mathbf{V} \cdot \hat{\mathbf{n}}) \\ \rho_2(\mathbf{V} \cdot \hat{\mathbf{n}}) \\ \vdots \\ \rho_N(\mathbf{V} \cdot \hat{\mathbf{n}}) \\ \rho u(\mathbf{V} \cdot \hat{\mathbf{n}}) + \hat{n}_x p \\ \rho v(\mathbf{V} \cdot \hat{\mathbf{n}}) + \hat{n}_y p \\ \rho w(\mathbf{V} \cdot \hat{\mathbf{n}}) + \hat{n}_z p \\ \rho_1 e_{n_1}(\mathbf{V} \cdot \hat{\mathbf{n}}) \\ \rho_2 e_{n_2}(\mathbf{V} \cdot \hat{\mathbf{n}}) \\ \vdots \\ \rho_M e_{n_M}(\mathbf{V} \cdot \hat{\mathbf{n}}) \\ \rho h_0(\mathbf{V} \cdot \hat{\mathbf{n}}) \end{array} \right\} \quad (2.8)$$

This portion of the Navier–Stokes equations represents the convection terms, that is, the terms that provide for the bulk motion of mass, momentum, and energy through the boundaries of a cell. Note that \mathbf{V} is the local velocity and $\hat{\mathbf{n}}$ is the outward directed surface normal of a cell face.

The viscous flux vector, $\mathbf{F}_v \cdot \hat{\mathbf{n}}$, is the next vector in Equation 2.5 and expands as:

$$\mathbf{F}_v \cdot \hat{\mathbf{n}} = \left\{ \begin{array}{c} -\rho_1 \vec{\nu}_1 \cdot \hat{\mathbf{n}} \\ -\rho_2 \vec{\nu}_2 \cdot \hat{\mathbf{n}} \\ \vdots \\ -\rho_N \vec{\nu}_N \cdot \hat{\mathbf{n}} \\ \\ \mathcal{T} \cdot \hat{\mathbf{n}} \\ \\ -\nabla q_{n_1} \cdot \hat{\mathbf{n}} \\ -\nabla q_{n_2} \cdot \hat{\mathbf{n}} \\ \vdots \\ -\nabla q_{n_M} \cdot \hat{\mathbf{n}} \\ -(\nabla q + \mathcal{T}\mathbf{V}) \cdot \hat{\mathbf{n}} \end{array} \right\} \quad (2.9)$$

This vector contains the portion of the Navier–Stokes equations responsible for species diffusion, momentum reduction from viscous stress, and conduction of heat. In Equation 2.9, $\vec{\nu}_i$ is the mass diffusion coefficient of the i th species, ∇q is the heat flux

gradient, and \mathcal{T} is the viscous stress tensor, which is defined as:

$$\mathcal{T} \equiv \begin{bmatrix} \tau_{xx} & \tau_{xy} & \tau_{xz} \\ \tau_{yx} & \tau_{yy} & \tau_{yz} \\ \tau_{zx} & \tau_{zy} & \tau_{zz} \end{bmatrix} \quad (2.10)$$

For a Newtonian fluid, the shear stress tensor is linearly dependent on the strain rate through the viscosity coefficient, μ .

Finally, the chemical source vector of Equation 2.5, \mathbf{S} , is expanded as:

$$\mathbf{S} = \left\{ \begin{array}{c} \dot{\rho}_1 \\ \dot{\rho}_2 \\ \vdots \\ \dot{\rho}_N \\ 0 \\ 0 \\ 0 \\ \dot{\rho}_1 e_{n_1} + \rho_1 \dot{e}_{n_1} \\ \dot{\rho}_2 e_{n_2} + \rho_2 \dot{e}_{n_2} \\ \vdots \\ \dot{\rho}_M e_{n_M} + \rho_M \dot{e}_{n_M} \\ 0 \end{array} \right\} \quad (2.11)$$

The chemical source vector consists of the species and non-equilibrium production terms. The source terms in Equation 2.11 are needed to compute high temperature flows with reacting chemistry. Generally, for a non-reacting or a single species gas flow, this vector does not contribute to the Navier–Stokes flow field solution. For the present study, the chemical source term was not needed in the CFD calculations.

The solution of Equation 2.5 requires knowledge of the cell face variables to evaluate fluxes in and out of the cell. However, only cell averaged values are available from the discretized finite volume computational domain. The method, applied to extract the cell face variables using cell averaged values, is called reconstruction. The variable reconstruction method used in GASP is the Monotonic Upstream centered Scheme for Conservative Laws (MUSCL) and is given by the following formulation:

$$\begin{aligned}\mathbf{q}_{i+1/2}^l &= \mathbf{q}_i + \frac{\phi}{4}[(1 - \kappa)(\mathbf{q}_i - \mathbf{q}_{i-1}) + (1 + \kappa)(\mathbf{q}_{i+1} - \mathbf{q}_i)] \\ \mathbf{q}_{i-1/2}^r &= \mathbf{q}_i - \frac{\phi}{4}[(1 + \kappa)(\mathbf{q}_i - \mathbf{q}_{i-1}) + (1 - \kappa)(\mathbf{q}_{i+1} - \mathbf{q}_i)]\end{aligned}\tag{2.12}$$

where ϕ defines the overall scheme accuracy as either 1st order ($\phi = 0$) or higher order ($\phi = 1$) and κ defines the higher order reconstruction spatial accuracy. With $\phi = 1$, for example, $\kappa = -1$ produces a backward gradient, 2nd-order upwind scheme, $\kappa = 0$ yields Fromm’s scheme, which is 2nd-order accurate and uses a symmetric gradient, $\kappa = 1/3$ produces a 3rd-order, quadratic scheme, and $\kappa = 1$ generates a forward gradient, central difference scheme. Note that the right face of a cell ($i = 1/2$) is given by $\mathbf{q}_{i+1/2}^l$, and the left face of a cell ($i = -1/2$) by $\mathbf{q}_{i-1/2}^r$ in Equation 2.12.

To effectively apply the MUSCL scheme and obtain solutions of a flow field with shock wave discontinuities, limiting of the higher order portion to values near those of adjacent cells is required. Limiting allows a solution to remain bounded and controls oscillations of the cell values near the discontinuity.

After properly discretizing the governing equations (See Equation 2.5.), applying the secondary equations to close the governing equation set, and specifying the initial and boundary conditions to the computational domain, the computationalist needs a numerical method to yield a solution of the flow field. For the present application, the implicit Jacobi time integration provided the iterative scheme to produce the converged solution.

Other applications of the GASP code are presented subsequently. Olynick and Henline [57] report a benchmark study using GASP to predict heating for thermal protection systems for the RLV vehicle. Olynick and Tam [58] have validated the GASP predicted heating by comparing their results with Shuttle Orbiter surface heating measurements obtained during the STS-2 flight. GASP has also been applied to a number of high priority NASA studies recently: Gnoffo et al. [31] review the CFD algorithms that have been used for studies of hypersonic aerothermodynamics for various vehicles and cite that GASP has provided high quality, low cost solutions quickly for X-33 thermal protection system (TPS) sizing. The X-33 vehicle is a concept demonstrator for the RLV. Additionally, the GASP algorithm has been applied to the X-38 vehicle, a NASA Johnson Space Flight Center concept for an emergency crew return vehicle from the International Space Station (ISS). The X-38 studies provided code validation by comparing with Mach 6 and 10 wind tunnel aerodynamic and aerothermodynamic results

and predictions of the radiation equilibrium surface temperature along the projected flight profile for TPS sizing (Campbell et al. [14] and Loomis et al. [46]).

Holden et al. [37] have applied GASP to validate the Large Energy National Shock Tunnel (LENS) test stream at 5 MJ/kg and 10 MJ/kg enthalpy levels for planetary probe entry studies. Also reported by Holden et al. [37] was a comparison of the GASP laminar and turbulent film cooling results for a hypersonic interceptor-seeker aperture with experimental results obtained from the LENS. Another recent application of the GASP has been to provide a numerical solution for an experimentally simulated fuel injection and mixing SCRAMjet engine study (Fuller [24]). After Helium was injected at Mach 1.7 into a Mach 6 free stream nitrogen-oxygen mixture, a comparison of the CFD solution with the experimental results showed a generally good agreement (Fuller [24]).

2.3.2 Direct Simulation Monte Carlo

In contrast, a solution of rarefied and free-molecular flow requires a different approach than that of the continuum regime. The solution must account for the molecular behavior consisting of the random motion of individual molecules colliding with one another. Because the properties of a rarefied or free-molecular flow depend on the statistical nature of molecular motion rather than by the average control volume approach of a continuum flow, the CFD technique is not, in general, applicable to flow in the rarefied regime. The Knudsen number, Kn , is a useful non-dimensional parameter to quantify the rarefaction of a flow. The Kn is the ratio of the molecular mean free path, λ , to a characteristic length scale, L . The rarefied regime is defined by flow with $0.001 < Kn < 10$ (Haas et al. [35]).

Numerical studies based on a statistical molecular model are required for a rarefied or free molecular flow solution because the complex construct of the Boltzmann equation, which describes fluid motion by the kinetic theory, does not yield analytic solutions for real gases. Before discussing the present numerical solution method, a historical perspective of the development of the governing Boltzmann equation is presented.

2.3.2.1 Historical Perspective of Kinetic Theory

A thorough history of the events, which lead to the present understanding of molecular gas dynamics, is given in the classic text by Chapman and Cowling [17]. A summary of some significant milestones, taken from their textbook [17], are presented in this section.

In early, ancient Greece, Democritus and Epicurrus and later Lucretius, first realized that matter consisted of particles at the atomic scale. But little advancement occurred until, from about 1650 to 1750, some aspects of the kinetic theory were being studied independently by Gassendi, Hooke, and D. Bernoulli. It was not, however, until the mid-1800's to early 1900's that progress toward defining the kinetic theory was revived by Clausius, Maxwell, and Boltzmann, who developed a physical description of gases at the atomic level, which is the basis of our current understanding. Hence, Clausius, Maxwell, and Boltzmann are now known as the founders of the kinetic theory of gases.

Maxwell proposed a law for a uniform gas in an equilibrium state, which characterized the molecular velocity distribution. Discussions with others at that time led to the science of statistical mechanics and some developments in the quantum theory. In

1866, Maxwell mathematically described a non-uniform gas by deriving the equations of transfer. These equations stated that the rate of change of a molecular property is divided into molecular collision effects, the molecular motion from one point to another, and contributions from external forces. Further, he modeled molecules as a single point, center of force with the force varying with distance to the power $1/n$; Maxwell incorrectly assigned n as 5 for gases as later experiments would prove. However, this early work lead to the first accurate theory to determine viscosity, thermal conductivity, and diffusion coefficients for gases.

Boltzmann, in 1872, developed his H -theorem, which showed that if a gas is allowed to proceed to a steady state condition, regardless of the initial condition, it would arrive at Maxwell's velocity distribution. As a consequence, the theorem strengthened the results of the early work of Maxwell. Additionally, during this time, Boltzmann introduced his famous integro-differential relationship that describes the velocity distribution function for a non-uniform gas. Bird [11] presents the Boltzmann equation as:

$$\frac{d}{dt}(nf) + \mathbf{c} \cdot \frac{d}{d\mathbf{r}}(nf) + \mathbf{F} \cdot \frac{d}{d\mathbf{c}}(nf) = \int_{-\infty}^{\infty} \int_0^{4\pi} n^2 (f^* f_1^* - f f_1) c_r \sigma d\Omega d\mathbf{c}_1 \quad (2.13)$$

The terms of the Boltzmann equation are developed for a phase space element of dimensions $d\mathbf{c}d\mathbf{r}$. The leading term on the left-hand-side of Equation 2.13 accounts for the time rate of change of molecules in the element. The next two terms, $\mathbf{c} \cdot \frac{d}{d\mathbf{r}}(nf)$ and $\mathbf{F} \cdot \frac{d}{d\mathbf{c}}(nf)$, are surface convection terms that describe the effect of molecular velocity and external forces, respectively, on molecules, which move across the element face. Finally,

the total rate of increase of class \mathbf{c} molecules because of collisions is given by the integral relation on the right-hand-side of the Boltzmann equation.

Returning to the historical account given by Chapman and Cowling [17], Maxwell, in 1879, presented results for a rarefied gas that showed stress would result from a temperature difference and the velocity distribution function would take the form $f = f_o(1 + \Phi)$, where f_o is the equilibrium portion of f and the function Φ accounts for perturbations from the equilibrium state. The functional form of Φ was also determined from Maxwell's equations of transfer. In 1880, Boltzmann reviewed Maxwell's results and remarked that solutions for the integral form of f could not easily be obtained for molecules represented by "elastic spheres"; instead, solutions could only be obtained if Maxwellian molecules ($n = 5$) were assumed.

The next advancement in the description of a non-uniform gas was made by Lorentz in the early 1900's. He extended the theory to a mixture of heavy and light molecules by ignoring collisions between light molecules. His solution of the Boltzmann equation was exact and was a limiting case, which he used to describe electron motion in a metal. When Bohr generalized Lorentz's theory, he found that electrical and thermal conductivity could be established as the solution of a Fredholm type integral equation.

Chapman and Cowling [17] further explain that Enskog, in 1911, also followed Lorentz's gas mixture model to calculate thermal diffusion for a Lorentzian gas with a temperature gradient. In addition, he discovered that results based on the expansion of $f = f_o(1 + \Phi)$ by Boltzmann lead to complex calculations for a simple gas and a gas mixture. For the mixture, it required molecules to be unsymmetric.

Other early twentieth century developments in solving Boltzmann's equation were being pursued [17]. For a rigid spherical molecule, Hilbert, in 1912, theorized that the solution of the Boltzmann equation should be in the form of an infinite series of linear integral equations. However, he did not obtain a solution. In 1915, Pidduck employed Hilbert's transformation and obtained the first accurate solutions for the diffusion coefficient of a non-Maxwellian or non-Lorentzian gas. But the solution was specific and labor intensive and required repeating all calculations for each case.

Chapman, independent of Enskog, in 1912 used Maxwell's functional form of $f = f_o(1 + \Phi)$ to produce a general expression for the viscosity and conduction coefficients of both a simple gas and a gas mixture. The functional form of Φ was of third degree in velocity components. In 1933, Burnett further expanded the solution method of Chapman and Enskog using Sonine polynomials to describe f . Chapman and Cowling [17] suggest that Burnett's contribution was one of the final improvements to the general kinetic theory of non-uniform, dilute gases. Since the last publication of their text [17] in 1952, however, many advances in the solution of non-uniform, dilute gas flows have taken place. The most notable, which has gained wide acceptance, is the direct simulation Monte Carlo (DSMC) method developed by Bird [9] and [11].

In his text, Bird [11] provides a history of the more recent techniques to obtain solutions to non-uniform gas flows. The following account of some of these techniques is taken from Bird [11].

Except for the application to special cases, the complexity of the Boltzmann equation (See Equation 2.13.) precludes an analytic solution of a general flow field. Additionally, flows with reacting chemistry and thermal radiation components cannot

be solved by the Boltzmann equation because it was not developed for these flow types. Therefore, some indirect approaches have been formulated for approximate analytic solutions of special cases. For example, Cercignani, in 1969, presented a solution method for small perturbations, which linearizes the Boltzmann equation. However, the linearized Boltzmann equation has limited practical application.

Some solution methods rely on assuming certain properties or functional forms of the velocity distribution function and are known as moment methods. A common approach is to multiply the Boltzmann equation by a molecular quantity, Q , and integrate over the velocity space. The five moment Navier–Stokes equations are obtained by assigning $Q = m$, mV , and $\frac{1}{2}mV^2$ and arguing that mass, momentum, and kinetic energy are conserved in a collision. By adding other quantities to Q (shear stress and heat flux), Grad developed his Thirteen Moment Equations.

In addition to indirect approaches, direct numerical procedures have been attempted using finite difference and finite element formulations to discretize the Boltzmann equation as outlined by Bird [11]. Nordsieck, Hicks, and Yen, in the early 1970's, produced a solution to a simple one-dimensional, steady-state problem by applying finite differences to the “fluid-like” terms on the left side of Equation 2.13 and Monte Carlo sampling to the collision term on the right side. Systematic errors lead to some difficulty; however, the results proved to be satisfactory. Recently, around 1990, two-dimensional, steady flow problems were attempted independently by Tcheremissine and Tan. Although adequate solutions were obtained, a computational difficulty was encountered in specifying a grid to bound velocity space, which extends from zero to infinity.

The first techniques to physically simulate the flow were the molecular dynamics (MD) methods developed by Alder and Wainwright in 1957 (See Bird [11].). Their method required that the number of simulated molecules be inversely related to the actual number of local molecules. Therefore, the method is better suited for simulating dense flow rather than rarefied flow, where a typical problem may require tracking 10^{20} simulated molecules.

The first probabilistic simulation method, developed by Davis in 1960 and Haviland and Lavin in 1962, has been named the test-particle Monte Carlo method [11]. The scheme requires an estimate of the velocity distribution function for the entire flow field, which serves as an initial target distribution. Trajectories of many test particles are calculated from the target velocity distribution and collide with target particles. The resulting test particle velocity histories collectively produce a new target velocity distribution. The process is repeated until the current and resulting velocity distribution functions converge. Note that simulations with this method are best suited for highly rarefied or collisionless flows. For the later, molecular reflections are mainly from surface interactions and molecule-to-molecule collisions, which are computationally intensive, can be ignored.

A refinement to the test particle method is to simultaneously track, in time, a large number of simulated molecules. Rather than computing the distribution function in velocity space for a large number of resultant test particle collisions, computations of the movement and collision of individual simulated molecules are made in physical space composed of a network of cells, which bound the flow field. This technique is called

the direct simulation Monte Carlo (DSMC) method. The principle limiting assumption of the DSMC method is that the simulated molecule movement can be uncoupled from molecular collisions by introducing a movement time step smaller than the mean time between collisions. Bird, in 1962, was the first to implement such a method (See Bird [11].).

The DSMC method has some of the same limitations as the Boltzmann equation: that is, the method was developed for binary collisions, when molecular collisions are treated as discrete events, and when the gas is in a state of molecular chaos (See Bird [11].). Also, implicit with DSMC is that the gas is dilute with small intermolecular forces, which are therefore usually negligible. A difference between the Boltzmann equation and DSMC method is that the dependent variable for the Boltzmann equation is the velocity distribution function in phase space for an infinitely large population of molecules, whereas, DSMC requires only the tracking of motion and collisions for a discrete number of simulated molecules, which represent the motion of real molecules. Other significant differences between the two are that the DSMC method does not rely on inverse collisions and it allows for application to multi-species chemically reacting flows, which are not attainable by the Boltzmann equation.

Additionally, Bird [11] discusses some specific issues associated with the DSMC method. First, a large number of samples are required in a simulation to reduce statistical fluctuations, which are inversely proportional to the square root of the number of samples. But recent computer advancements have, to some degree, minimized this concern because of the rapid computational speed increase. Next, the DSMC method may introduce random walks into a solution because molecular quantities are conserved on the average,

but may not be conserved exactly for each discrete event. Also, round-off errors in the velocity components and energies exist because of the discrete arithmetic of computers. Lastly, if an inadequate number of simulated molecules are in a cell, the extremes of the distribution function may not be accurately approximated by the small sample set of molecules.

2.3.2.2 Application of the Solution Technique

As discussed in the previous section, the DSMC technique is valid for any flow field simulation of a dilute gas that is not influenced by a highly ionized plasma because it is developed directly on relationships, which form the basis of the kinetic theory of gases (Bird [9] and [11]). The DSMC method does not solve a set of equations to produce a solution of the flow field, but rather it statistically tracks movements and collisions of simulated molecules, each of which represent an average of many molecules. The velocity and position of simulated molecules are allowed to change within and through the boundaries of a fixed number of cells in a discretized computational space as time is advanced. Statistical probability determines post-collision velocities of interacting molecules. After many time steps, average macroscopic gas properties of the simulated molecules in each cell produce a flow solution within the boundaries of the domain. Likewise, surface properties are determined by averaging many molecular wall collisions, which exchange momentum and energy at the wall boundary (See Bird [9] and [11] for a complete description of the technique.).

Two programs are used to apply the DSMC simulation for the present study: The G2 code of Bird [10] is used for a molecular simulation of the plate flow with no

jet interaction to determine the degree of rarefaction of the plate flow. The DSMC Analysis Code (DAC) of LeBeau (LeBeau [44], Glass and LeBeau [30], and Wilmoth et al. [94]) is used to apply the DSMC simulation for the jet interaction simulations. The Larsen-Borgnakke model (Borgnakke and Larsen [12]) is used in G2 and DAC to account for energy transfer between kinetic and molecular internal energy modes. For DAC, domain boundaries of vacuum, free stream, and symmetry, and wall boundaries of solid, outgassing, inflow, and outflow are currently available. Multiple species simulations with variable wall molecular reflectivity and variable temperature are also available. Presently, DAC is a beta version research computer program under development and references for the program are few; however, early results are quite promising. Results reported by Wilmoth et al. [94] show good agreement between DAC and other DSMC implementations.

DAC is not a single DSMC solution program but rather a series of computer programs: a geometry, grid, and boundary condition preprocessor (*predac*); a program to execute the molecular simulation in serial or in parallel (*dac* and *ddac*, respectively); and solution post-processors (*slice* and *sprop*) (In parenthesis are the DAC executable names.). The parallel DAC execution program is written with message passing interface (MPI) (See Message Passing Interface Forum [50].) subroutine calls in the software algorithms, which allows it to take advantage of memory and parallel processing capabilities of program execution on multi-processor and multiple-networked computers. For the present study, DAC employs the use of the Local Area Multicomputer (LAM) (Ohio Supercomputer Center [56]) version of MPI to provide code execution on local SGI workstations with R10000 processors and the Cray Message Passing Toolkit (MPT)

software for code execution on the massively parallel processor (MPP) SGI/Cray T3E at the NASA Goddard Space Flight Center.

Given in the next two chapters, specific details of the present hybrid uncoupled CFD-DSMC technique will be presented and the technique will be applied to two different jet interactions: a flat plate experiment performed by Warburton [88] and an actively controlled aerobraking maneuver of the Mars Global Surveyor (MGS), which was previously studied by Shane et al. [76] and Shane [77]. Application of the method to these two problems will show the suitability of the uncoupled technique to predict jet interactions at the two distinctly different rarefied free stream conditions. The Knudsen number based on jet exit diameter is $Kn_d = 0.038$ for the flat plate experiment and $Kn_d = 49$ for the MGS aerobraking maneuver. It is important to note that for jet interactions in the rarefied flow regime, the free stream density may change over several orders of magnitude depending on the altitude; therefore, the magnitude of Kn_d will likewise change.

Chapter 3

Jet Interaction with Transitional–Rarefied Flow over Flat Plate

A numerical simulation of a jet interaction experiment on a flat plate test apparatus, which was performed by Warburton [88], is presented in this chapter. The experiment was conducted with a free stream flow at the overlap between the transitional and rarefied regimes. Because jet interactions are influenced by the flow properties of both the free stream and jet, modeling this experimental test condition provides a unique opportunity to establish the extent of the jet interaction influence with a free stream flow in the overlap transitional–rarefied flow regime. Understanding gained in modeling the experiment can be extended to modeling jet interactions on flight vehicles at similar flow conditions.

3.1 Discussion of the Jet Interaction Experiment

The present three-dimensional numerical study models the geometry and test conditions of an experiment recently completed in the Low Density Tunnel (LDT) at the DERA in Farnborough by Warburton [88]. A sonic jet was released through a circular nozzle exit on the planar surface of a sharp leading edged flat plate at zero incidence. The jet interacted with a rarefied nitrogen free stream at Mach 9.84, which produced a three-dimensional jet interaction flow field. Static temperature and static pressure of the free stream were 65K and 5.4 Pa, respectively. Four jet gases were used during the

experiment: helium, nitrogen, argon, and carbon dioxide at plenum or total temperature of 300K and plenum or total pressures of 17.4, 34.5, and 51.7 kPa (2.5, 5.0, and 7.5 psia), which provides 12 jet interactions of varying strength. The free stream flow of the experiment was fixed and had a mean free path, λ , of approximately 0.2 mm. The altitude with an equivalent mean free path is about 60 kilometers above the earth surface (COESA [18]). The Knudsen number, Kn_d , is 0.038 based on the free stream mean free path and the orifice diameter of 4 mm. This Knudsen number is at the transitional overlap between the continuum and rarefied flow regimes, and for the present study, the regime is termed the transitional–rarefied regime. A sketch showing the test apparatus and pertinent geometric dimensions of the flat plate model used for the experimental study is shown in Figure 3.1.

A brief outline of the current solution methodology for a cross-flow jet interacting with a transitional–rarefied flow is given next in this section; complete details of the method are presented in Section 3.3.2. To uncouple the continuum jet from the surrounding rarefied flow and interaction region, a boundary between the two regions must be established. The Bird breakdown parameter defines such a surface boundary as a function of flow field rarefaction. The breakdown surface can be determined from a CFD solution of an expanding nozzle flow. Because the experiment of Warburton consisted of 12 different jet interactions of various strengths, by applying CFD to each of the jet interaction cases and analyzing the extent of the breakdown surface of the expanding jet before the interaction interface between the jet and free stream fluid, a functional relationship between a correlation parameter and the Bird breakdown parameter can be obtained for this $Kn_d = 0.038$ condition. Although CFD does not strictly apply in the

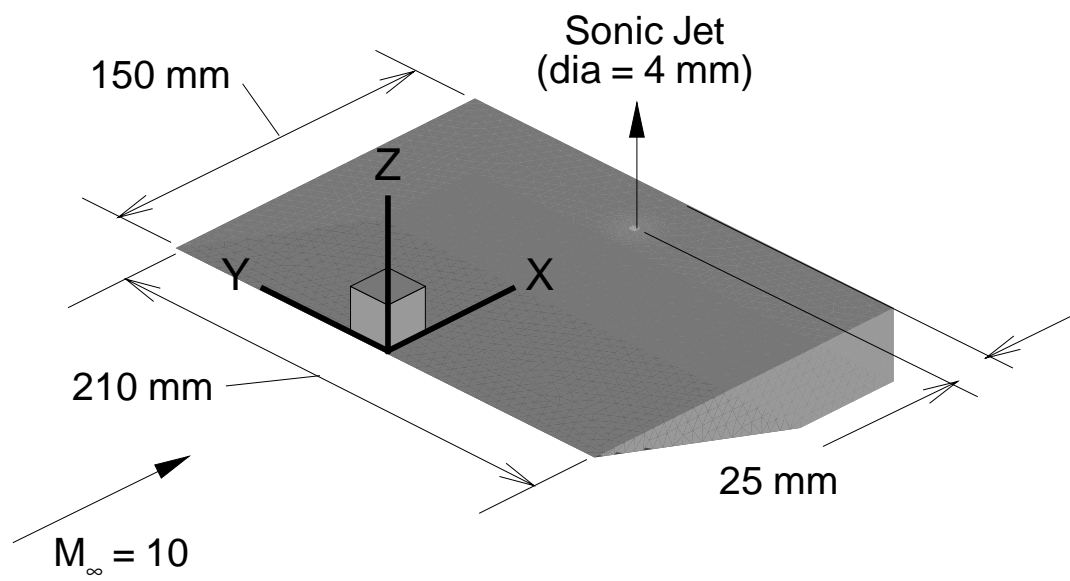


Fig. 3.1. Schematic diagram of the jet interaction flat plate model.

rarefied regime of the flow field, it does apply in the continuum jet plume region. The key to uncoupling the jet from the rest of the external flow is to determine a breakdown parameter number, P , for the jet plume prior to the interaction interface within which the jet plume flow is not influenced by the interaction. After the appropriate correlation of the jet strength as a function of P is determined, an uncoupled CFD–DSMC solution can be obtained.

The proposed method is to first apply CFD to all of the interacting jet cases of Warburton [88], analyze each solution in the near jet plume region, and establish a functional relation for the plume breakdown parameter value where the CFD–DSMC interface should be placed. Once the functional relation is determined, an axisymmetric solution of the expanding jet by CFD can be analyzed and a surface defined for an appropriate breakdown parameter value that assures the breakdown surface is not in the interacting regime. This breakdown surface can then be used as a jet inflow boundary condition for a DSMC solution of the outer and interacting flow regions.

It is important to note that by allowing the continuum portion of the higher density jet flow external to the nozzle exit to be determined by CFD, significant computational savings can be realized by not having to simulate that flow with DSMC. Thus, by obtaining a CFD solution for an expanding jet, determining the flow properties on a suitable breakdown surface, and applying those jet plume flow properties and the geometry of the breakdown surface as an inflow boundary to a DSMC solution, the two flow regimes are uncoupled and an accurate simulation of the jet interaction can be obtained.

3.2 Assessment of 2-D Flat Plate Flow

The free stream nitrogen flow about the sharp leading edged flat plate of the Warburton [88] experiment has a nominal Mach number of 9.84, static temperature of 65K, and static pressure of 5.4 Pa, which results in a free stream unit Reynolds Number, Re_∞ of 105971/m or a Reynolds number based on the plate length, Re_L of 15,900. A hypersonic, low Reynolds number flow over a flat plate will exhibit viscous interaction, and, for this case, if the viscous interaction is strong enough, a degree of flow rarefaction. To determine the strength of the viscous interaction and extent of rarefaction, flow over the flat plate with no jet interaction is analyzed. First an evaluation of the flat plate flow based on the two common viscous interaction parameters $\bar{\chi}$ and \bar{V} is given; then, an application of the DSMC technique to the flat plate flow by the G2 code (Bird [10]) is presented to provide an assessment of the flow rarefaction based on the velocity slip and temperature slip at the edge of the Knudsen layer of the flat plate flow. The Knudsen layer is the non-continuum gas layer one local mean free path from a surface (Gupta and Simmonds [33] and Gupta et al. [34]).

3.2.1 Common Viscous Interaction Parameters

A viscous interaction occurs for a hypersonic flow when the developing boundary layer displaces and interacts with the free stream and causes a compression, which interacts with the boundary layer. For low density, hypersonic flows with a strong interaction between the free stream and developing viscous layer, the two regions become coincident

and merge. Flow rarefaction in a merged layer is significant because the velocity slip and temperature jump are large in the region (Moss et al. [52]).

The $\overline{\chi}$ viscous interaction parameter provides an indication of the strength of the induced pressure change on the surface of the flat plate because of the boundary layer displacement of the free stream flow and resultant flow compression. $\overline{\chi}$ is defined as:

$$\overline{\chi} = \frac{M_\infty^3}{\sqrt{Re}} \sqrt{C} \quad (3.1)$$

where C is the Chapman-Rubesin constant (Moss [52]). The other viscous interaction parameter, \overline{V} , is defined as:

$$\overline{V} = \frac{\overline{\chi}}{M_\infty^2} \quad (3.2)$$

and is more appropriate for correlating pressure coefficient and force coefficients because these coefficients are normalized by the dynamic pressure, which is directly proportional to the square of the free stream Mach number.

Both viscous interaction parameters, $\overline{\chi}$ and \overline{V} , given by Equations 3.1 and 3.2 were calculated for the zero incidence flat plate with the free stream flow conditions of the experiment (Warburton [88]) to evaluate the strength of the viscous interaction of the flat plate flow. The results of the calculations are presented in Figure 3.2. Anderson [7] states that $\overline{\chi}$ greater than 3 is a strong viscous interaction region, and Moss et al. [52] state that a value of \overline{V} greater than 0.15 is a merged layer region. Using these criteria, Figure 3.2 shows that the flow over the plate is entirely dominated by a strong viscous interaction; that is, the local induced pressure is much greater than the inviscid value of

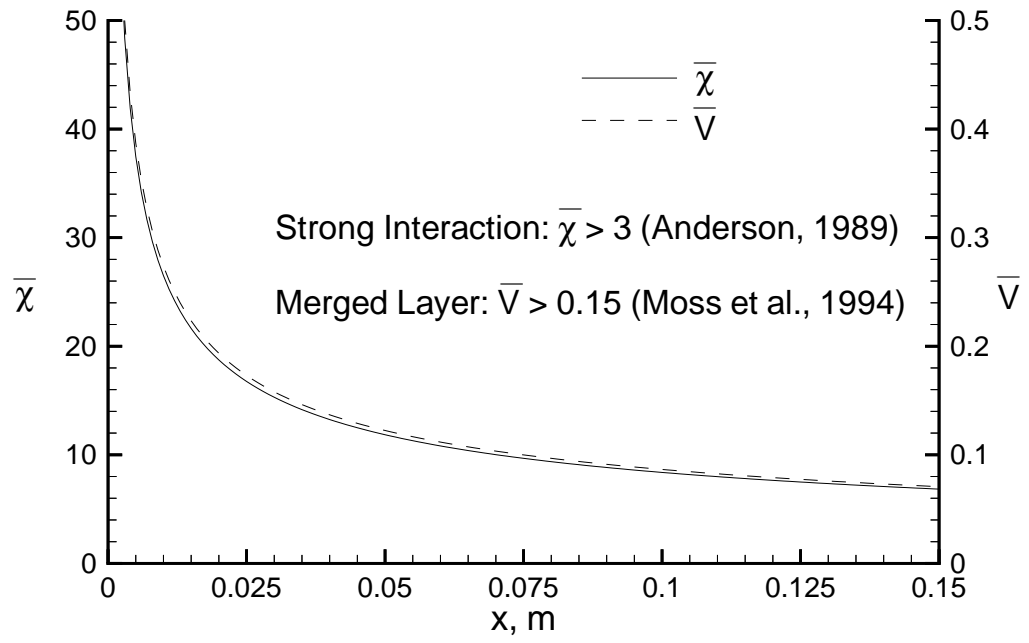


Fig. 3.2. Viscous interaction parameters of the upper flat plate surface flow with no jet interaction.

the free stream static pressure, and the forward 22% of the flat plate flow is a merged layer region where the compression shock and viscous boundary layer are indistinguishable. Thus, the analysis based on viscous interaction parameters shows, with no jet interaction, a significant portion of the flat plate flow will have rarefaction effects present.

3.2.2 DSMC Modeling by the G2 Code

To further quantify the extent of the flat plate flow rarefaction, a two-dimensional molecular simulation of the flow over the upper portion of the flat plate at the experimental test condition has been performed using the Bird G2 code (Bird [10]). Free stream flow conditions used are a bulk velocity, V , of 1617.1 m/s, static temperature, T , of 65K and number density, n , of 6.018×10^{21} molecules/m³. The nitrogen free stream gas was modeled as a variable hard sphere (VHS) with a reference diameter of 4.07×10^{-10} m at 300K, a temperature-viscosity coefficient of 0.75, and a molecular mass of 4.65×10^{-26} kg. Also, two degrees of freedom were included in the rotational portion of the energy balance because nitrogen is a diatomic molecule. The ratio of real to simulated molecules was 3.01×10^{13} and the cell dimension normal to the wall was at least one-quarter of the free stream mean free path, which yielded normal cell spacing of 50 μm and a simulation time step of 0.25 μsec . Moss et al. [53] performed a grid sensitivity study with the G2 code on viscous interactions and showed grid independence was achieved for normal cell resolution of 0.35 of the local mean free path. Therefore, the grid spacing normal to the wall for the present two-dimensional DSMC implementation is sufficient to capture the local viscous effects and allow an analysis of the velocity slip and temperature slip at the edge of the Knudsen layer.

The DSMC calculation proceeded in time for 0.5 msec (or 2000 time steps) to allow the number of simulated molecules in the domain to become constant at about 1.8 million. Then, the sampling registers were cleared and steady state sampling began. Steady state sampling continued for another 4.0 msec (or 16 thousand time steps) until greater than 10,000 surface samples were obtained at each cell interface with the plate boundary to reduce statistical scatter. The statistical fluctuations associated with the DSMC technique decrease approximately with the inverse of the square root of the number of samples (Bird [11]); therefore, for example, 10,000 surface samples will produce a solution with statistical fluctuations of about one percent in the surface quantity being sought.

Shown in Figure 3.3 are number density contours from the G2 two-dimensional molecular simulation of the flat plate flow. The number density has been normalized by Loschmidt's number, n_o , which is the standard number density of air at a pressure of 101,325 Pa and a temperature of 0°C. The compression wave shown in the figure above the zero incidence upper surface is caused by the free stream flow being turned by the developing viscous boundary layer near the wall.

The region occupied by the DSMC solution domain is shown by the number density contours in Figure 3.3. Note that modeled in the domain are the regions forward of the plate sharp leading edge, adjacent to the plate, and behind the plate. The free stream condition is applied to all domain boundaries except the solid surface of the plate, which is held at a constant temperature of 300K and treated as diffuse with full momentum and thermal accommodation. The horizontal boundary behind the plate

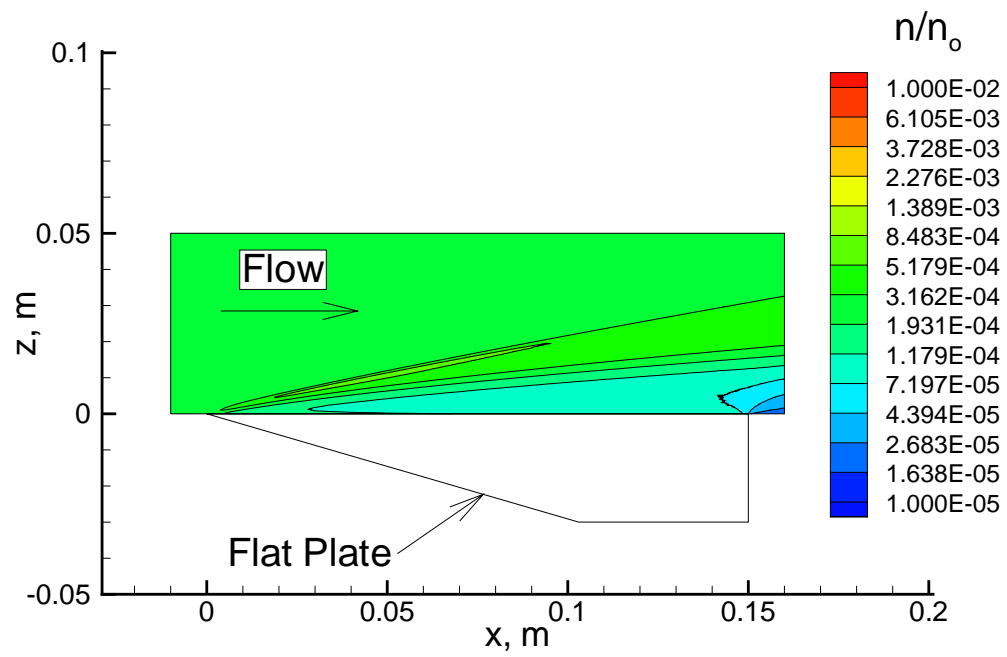


Fig. 3.3. Number density contours of the flat plate flow from the G2 DSMC solution.

surface has a vacuum boundary condition that simulates the effect of the plate wake region on the flow.

The extent of the viscous boundary layer above the flat plate is shown in Figure 3.4. An analysis of the local flow field was performed to determine the boundary layer edge, $\delta_{0.99}$, defined as the location above the plate surface with a velocity that is 99% of the free stream velocity (or $0.99 V_\infty$). The location of the boundary layer edge is shown in Figure 3.4 by the solid line. Boundary layer growth is nearly constant over the plate from the leading edge to the trailing edge where the boundary layer is about 0.030 m thick. Such a steady thickening of the boundary layer, as shown in the figure, substantiates the merged layer and strong interaction behavior predicted by the viscous interaction parameters, $\bar{\chi}$ and \bar{V} , respectively, which was discussed previously and shown in Figure 3.2.

The local Knudsen number, Kn_l , of the upper surface flat plate flow is also shown in Figure 3.4 as a dashed line. The local Knudsen number is defined as:

$$Kn_l = \frac{\lambda_l}{\delta_{0.99}} \quad (3.3)$$

and indicates the percentage of the viscous layer occupied by the Knudsen layer next to the wall. Near the sharp leading edge, the Knudsen layer is greater than 10% of the viscous layer thickness. The percentage of the Knudsen layer in the viscous layer decreases downstream of the leading edge to about 2% of the total thickness at the plate trailing edge; however, note that the local mean free path has increased from the free

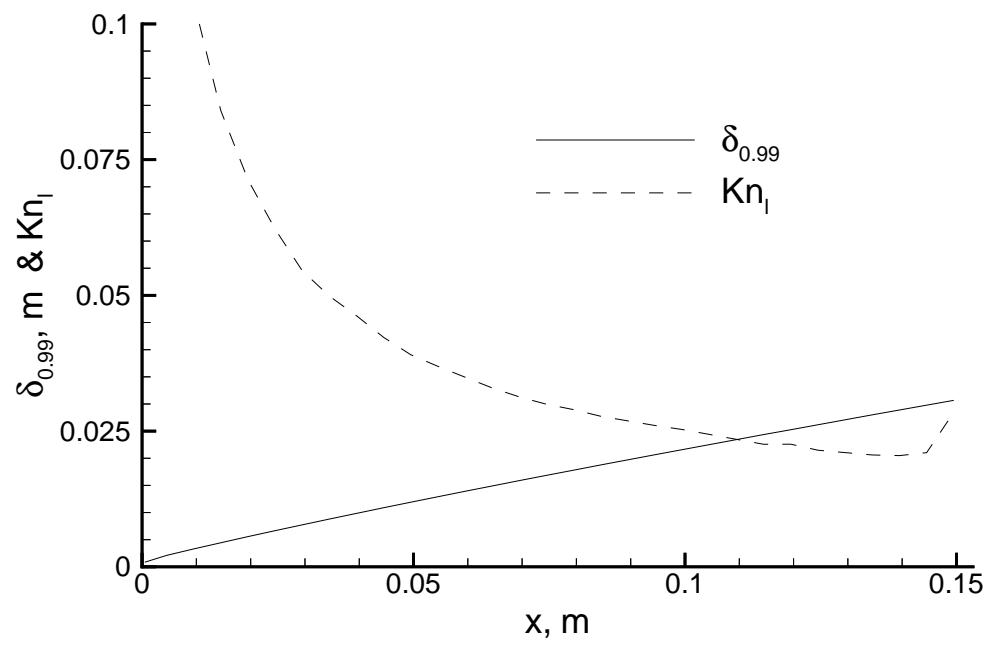


Fig. 3.4. Boundary layer edge and local Knudsen number of the upper surface flat plate flow with no jet interaction.

stream value of about 0.2 mm at the plate leading edge to a value greater than 0.6 mm at the plate trailing edge.

The cell resolution of the DSMC domain was set to at least one-quarter of the local mean free path normal to the plate surface to ensure grid independence of the solution and allow the velocity and temperature at the edge of the plate flow Knudsen layer to be evaluated. To quantitatively evaluate the velocity slip, the temperature slip, and determine the relative degree of flow rarefaction, two variables, the normalized Knudsen layer edge velocity, V_{Kn}^* , and the normalized Knudsen layer edge temperature, T_{Kn}^* , are defined, respectively, as:

$$V_{Kn}^* = \frac{V_{Kn}}{V_{\infty}} \quad (3.4)$$

and

$$T_{Kn}^* = \frac{T_{Kn}}{T_{wall}} \quad (3.5)$$

where the subscripts Kn , ∞ , and $wall$ in Equations 3.4 and 3.5 refer to the properties at the edge of the Knudsen layer, in the free stream, and at the wall, respectively. The definitions given as Equations 3.4 and 3.5 show that in the continuum limit V_{Kn}^* goes to zero, and T_{Kn}^* goes to one. Variance from these continuum limits indicates the degree of rarefaction of the flow in the viscous layer near the wall.

Figure 3.5 shows the results of the flow field analysis at the edge of the Knudsen layer. Plotted as a function of distance from the plate leading edge are the slip indicators: normalized Knudsen layer edge velocity and temperature (V_{Kn}^* and T_{Kn}^* , respectively).

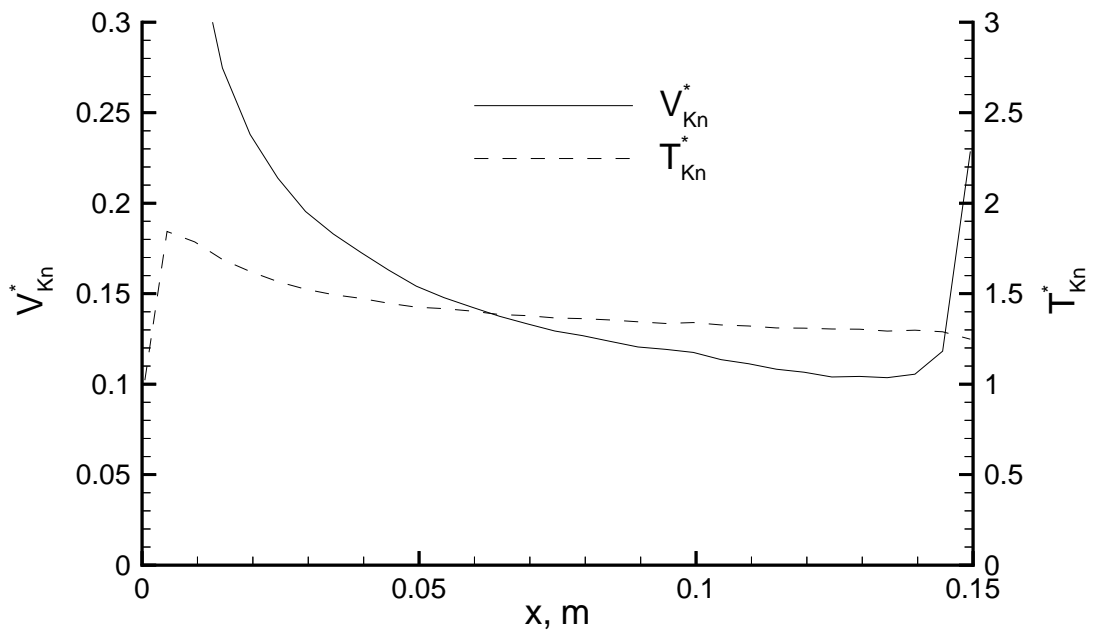


Fig. 3.5. Rarefaction of the flat plate upper surface flow with no jet interaction.

The velocity at the edge of the Knudsen layer is greater than thirty percent of the free stream velocity near the plate leading edge and decreases to about ten percent of the free stream velocity near the aft end of the plate. The temperature at the edge of the Knudsen layer is almost twice the wall temperature near the leading edge and decreases to about one and one-quarter times the wall temperature over the aft region of the plate. Results of the analysis shown on Figure 3.5 show that there is significant velocity and temperature slip over the forward portion of the plate, which moderates as the viscous layer develops. Therefore, the analysis of the flat plate flow molecular simulation at the experimental test condition with no jet interaction shows slip at the wall is significant and must be properly modeled numerically to capture the wall viscous effects for the jet interaction flow simulation.

3.3 Uncoupled Technique for Transitional–Rarefied Flow

Two types of flow solutions are presented for the flat plate jet interaction problem: a complete CFD solution and an uncoupled CFD–DSMC solution. The CFD solution of the interacting flow is from a direct application of the GASP (AeroSoft [2]) computer program to the given boundary conditions of the problem, which provides a suitable jet flow field solution that is analyzed to determine the appropriate uncoupling surface between the continuum jet and interacting flow. The approach taken to produce a CFD–DSMC solution is to uncouple the plume of the jet from the rest of the external flow field at the continuum surface and solve the interacting flow by the DSMC method. By uncoupling the jet flow, a molecular simulation is not applied to the high density continuum jet

plume just outside of the nozzle exit, thus reducing computational requirements. However, the difficulty for the uncoupled CFD–DSMC solution in the transitional–rarefied flow regime is defining the location of the surface boundary where the jet begins to interact with the rarefied free stream. The goal is to avoid a coupled CFD–DSMC solution, which would require iterative steps between the CFD and DSMC.

3.3.1 CFD Modeling of the Jet Interaction

An isometric drawing showing the volume of the CFD computational domain is given in Figure 3.6. The domain extends 0.1 m behind the flat plate and includes the region under the plate. Any effect on the upper flat plate flow from the lower plate wake influence should be captured by including the lower plate and wake regions in the computational domain. Additionally, the computational domain includes the subsonic portion of the nozzle from the plenum chamber boundary condition to the nozzle exit at the flat plate surface. The nozzle has a no slip wall boundary condition, which provides for nozzle boundary layer development. The flat plate is 0.150 m long and 0.210 m wide; however, because symmetry exists along the x-z plane midway of the plate, only one-half of the flow field was modeled computationally. Figure 3.6 shows the x-z plane of symmetry.

The CFD domain contains six zones (also called blocks). By dividing the domain into smaller regions, fewer computer memory resources are used when processing a solution as compared to a domain without such a multi-zone (or multi-block) arrangement. The multi-zone arrangement also allowed for the nozzle zone and zone above the nozzle, which are constructed using a cylindrical coordinate system, to be connected to adjacent

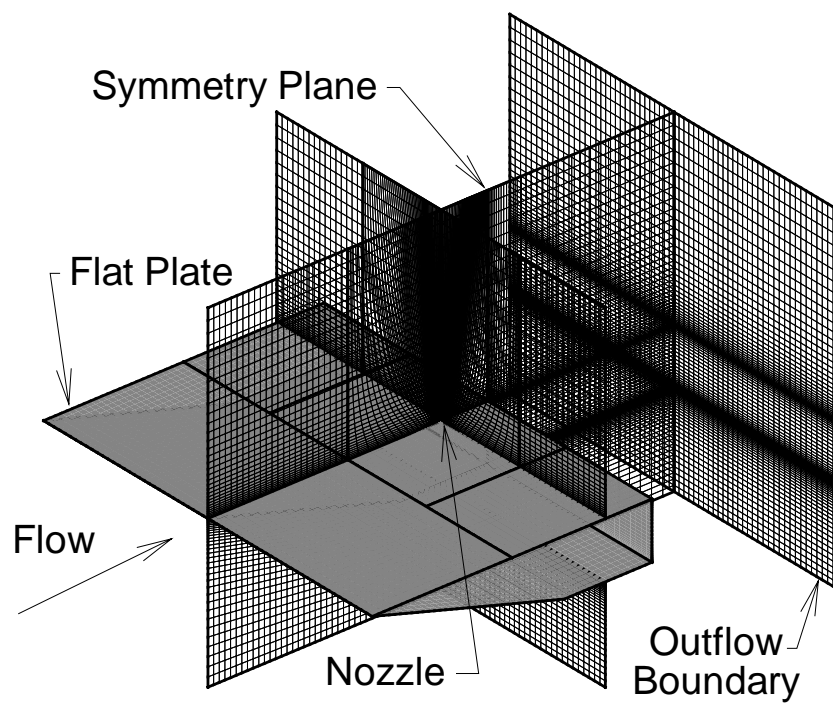


Fig. 3.6. Selected grid planes of the CFD computational domain.

zones described by a Cartesian coordinate system. A total of 319,488 cells are used to describe the flow domain; the maximum number of cells in any one zone is 98,304. During the numerical time integration of a solution, flux vector information was allowed to pass in both directions between boundaries of zones to ensure that no information was lost between zones.

The number of cells in each direction of a zone is divisible by four to allow mesh sequencing to be applied to the computational solution. Within the structure of the GASP CFD program, a coarse mesh solution can be interpolated as an initial condition to a finer mesh. For the jet interaction problem, three levels of mesh sequencing are used. Mesh sequencing can drastically reduce the time required to iterate a CFD solution to convergence (McGrory et al. [49] and AeroSoft [2]).

The computational solution from the GASP requires inviscid and viscous flux models, chemistry, and boundary conditions be specified. The inviscid flux scheme of Roe is applied to the nozzle zone, and the inviscid flux scheme of van Leer is applied to all other zones. Reconstruction with flux limiting is accomplished using the method of van Albada with third-order, upwind biased accuracy. The laminar viscous flux model with all thin layer and cross flow terms (full Navier–Stokes approximation) is applied for the solution scheme. A second-order accurate gradient applies to wall calculated quantities (that is, heat flux, skin friction, etc.). Sutherland’s law with Wilke’s mixing model specifies viscosity and conductivity transport properties for closure of the momentum and energy equations. Flow chemistry is modeled as a two-species, frozen mixture in translational and rotational equilibrium. The nozzle gas is modeled as one of the species and the free stream gas as the other species even when both gases are the same. The

solid wall boundary conditions of temperature at 300K and no slip are applied to all zones in contact with the flat plate or nozzle. All outflow boundaries are calculated as first-order extrapolated from the neighboring interior cells of the domain.

Solutions were obtained using global iterations of all zones with mesh sequencing and convergence was based on the value of the solution L_2 norm, which provides a measure of numerical convergence by showing the root mean squared difference between flux values of two consecutive iterative steps normalized by the flux values assigned to the grid prior to starting the numerical solution. After the L_2 norm decreased to a value of about 1×10^{-9} based on the initial condition, the solution was assumed converged as the L_2 norm no longer decreased and the change between iterations was judged close to machine round-off error. Each CFD solution for the present study was accomplished on a single processor of the decommissioned NASA Langley Cray Y-MP supercomputer (Sabre) using about 44 million bytes (Mbytes) of random access memory (RAM) for the fine grid time integration and required about sixty hours to reach the level of L_2 norm convergence indicated previously.

Figure 3.7 shows the flow field streamlines for the CFD solution of the argon jet-free stream interaction for a jet plenum pressure of 34.5 kPa (5 psia). Since the CFD solution was integrated numerically to a steady state condition, the arrowed lines on the figure represent flow streamlines. Each streamline is tangent to the flow velocity vector by which it passes and traces the path of a fluid element through the flow field. The free stream flow is from left to right, and the sonic argon jet is injected normally through a nozzle located 0.125 m downstream of the flat plate leading edge on the upper flat plate surface. Normalized number density at the symmetry plane for the argon jet interaction

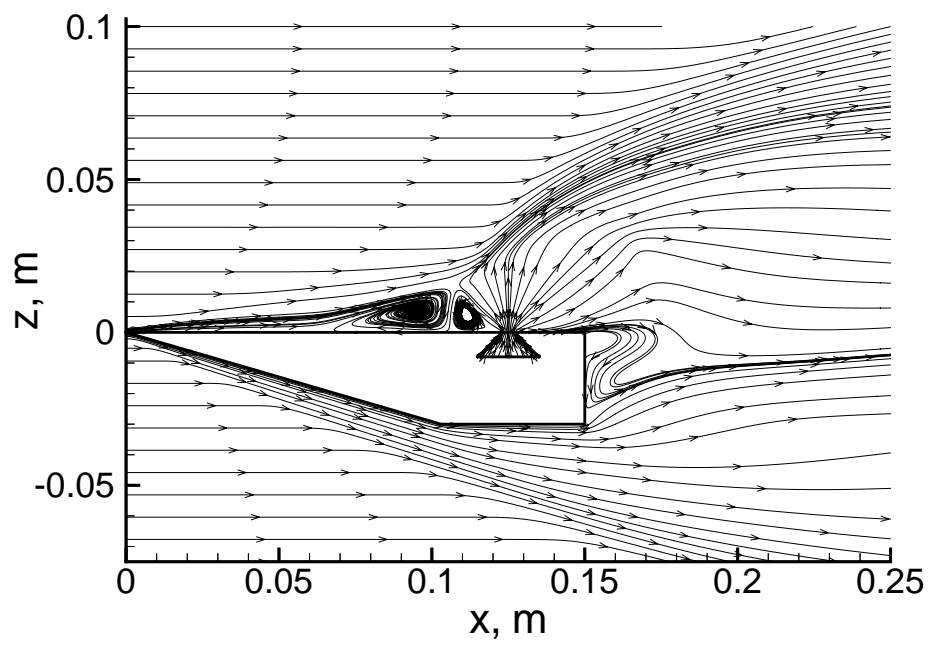


Fig. 3.7. Flow field streamlines on the symmetry plane from the CFD solution.

flow field is shown in Figure 3.8. The number density contours presented on the figure are normalized by Loschmidt's number, n_0 .

3.3.2 Non-Interacting Continuum Jet Plume Surface

To produce an uncoupled CFD–DSMC jet interaction solution, the present approach is to define a surface boundary between the non-interacting portion of the continuum jet plume and the interacting flow surrounding the plume, similar to that of a breakdown surface. To determine the departure of an expanding flow, such as the jet, from a continuum flow condition, Bird [11] proposes that a breakdown surface be defined with an associated breakdown parameter, P , of numerical value 0.02. In this section, the theory and mechanics of producing a breakdown surface from known flow field quantities, such as from a CFD solution, are developed and presented.

The approach for modeling the jet plume for the present study is similar to one that has been applied previously to study free expanding plume impingement (Lumpkin et al. [47] and Rault [64]). The jet plume of that study was modeled using a CFD solution; then, a breakdown surface and flow properties at the breakdown surface were derived from the CFD solution. Outside the breakdown surface, DSMC was applied with the breakdown surface as an inflow boundary to a molecular simulation.

In the study of expanding jet flow from the Shuttle Orbiter Primary Reaction Control System (PRCS) thrusters (Rault [64]), a parameter, N , was used to determine the boundary between the continuum and rarefied regime. The parameter is given as:

$$N = \nu\tau \tag{3.6}$$

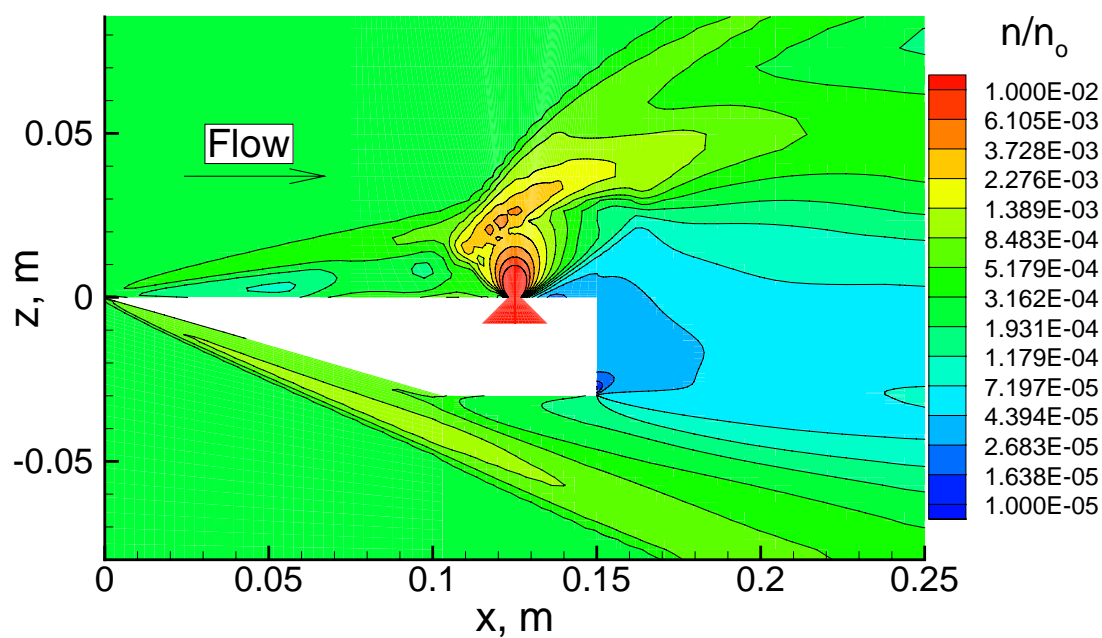


Fig. 3.8. Number density contours on the symmetry plane from the CFD solution.

where ν is the frequency of intermolecular collisions and τ is a characteristic time between collisions in the jet plume. Therefore, N is the number of intermolecular collisions in a characteristic time. Expanding the definition further, Rault [64] presents the characteristic time as:

$$\tau = \frac{L}{\vec{V}} \quad (3.7)$$

with length, L , defined as:

$$L = \frac{\rho}{\vec{\nabla}\rho} \quad (3.8)$$

where ρ is the local density of the gas. Therefore, substituting Equations 3.7 and 3.8 into Equation 3.6:

$$N = \frac{\nu\rho}{\vec{V} \cdot \vec{\nabla}\rho} \quad (3.9)$$

The breakdown parameter, P , of Bird [11] is just the inverse of N :

$$P = \frac{1}{N} = \frac{\vec{V} \cdot \vec{\nabla}\rho}{\nu\rho} \quad (3.10)$$

Using definitions given by Bird [11], the intermolecular collision frequency, ν , can be expressed as:

$$\nu = \left(\pi d^2 n\right) \left(\frac{16kT}{\pi m}\right)^{\frac{1}{2}} \quad (3.11)$$

Equations 3.10 and 3.11 provide a formulation for the breakdown parameter as a function of macroscopic flow field variables, which can be calculated from a CFD solution.

For application to the jet interaction with a transitional–rarefied flow field, it will be shown that the value of P chosen to describe the appropriate breakdown surface for the uncoupling of the continuum and non-continuum regions is sensitive to a combination of jet and free stream conditions. The difficulty is to define the boundary between the two regions to optimize the use of both CFD and DSMC numerical techniques.

3.3.3 Analysis of the Non-Interacting Jet Plume Surface

Given the definition of the breakdown parameter in the previous section, a scheme is implemented in the present section to calculate the breakdown surface from the jet interaction CFD solutions. A computer program that applies Equation 3.10 to a PLOT3D CFD flow field solution file has been written. PLOT3D is a common file format to represent a computational grid and solution (Walatka et al. [87]). A central differencing operator in the program calculates the density gradient term except at boundaries where a single-sided operator is used. The mass and diameter of the expanding gas species molecule are supplied as constants input to the program. The output of the program is a PLOT3D formatted solution file containing the breakdown parameter, P , as a spatial variable of the analyzed flow field.

A breakdown surface can then be obtained from the solution file as an isosurface to define the geometry of the breakdown surface for various values of P . A commercially available flow visualization and analysis program, EnSight (See CEI [15].) is used to

produce an isosurface corresponding to a constant value of breakdown parameter. An isosurface is created with the EnSight program by interpolation between the appropriately valued grid cell edges to define a point on the cell face. Points with the desired isovalue are connected and displayed as triangulated surface elements. The program provides, as an ASCII text output file, the cloud of points, which spatially describe the geometry of a given isosurface. For the present study, the cloud of points are the spatial boundary points of the Bird breakdown surface for a given value of the breakdown parameter.

This technique was applied to PLOT3D solution files of the twelve CFD jet interaction cases for various isosurface values. As an example, results of analyzing the calculated breakdown parameter field for the argon jet interaction at a jet plenum pressure of 34.5 kPa are shown in Figure 3.9. Isosurfaces at two values of the breakdown parameter are shown on the figure. At $P = 0.01$, the surface appears as a smooth body of revolution normal to the plane of the plate surface (shown by the darker flat region in the figure) even though the breakdown parameter was calculated from a CFD solution of a complex jet interaction (See Figures 3.7 and 3.8.). At $P = 0.02$, however, the breakdown surface extends further from the plate surface and begins to show evidence of the free stream interaction, as indicated by the nearly diagonal jagged cut through the upper portion of the breakdown surface. The irregularity of the cut is because a gradient type operation (Equation 3.10) is used by the flow visualization program to produce the isosurface from the breakdown parameter solution file, and small numerical disturbances are amplified. Effectively, a Laplacian operation has been applied to discrete flow field values of the CFD solution and produces the irregular cut shown on the

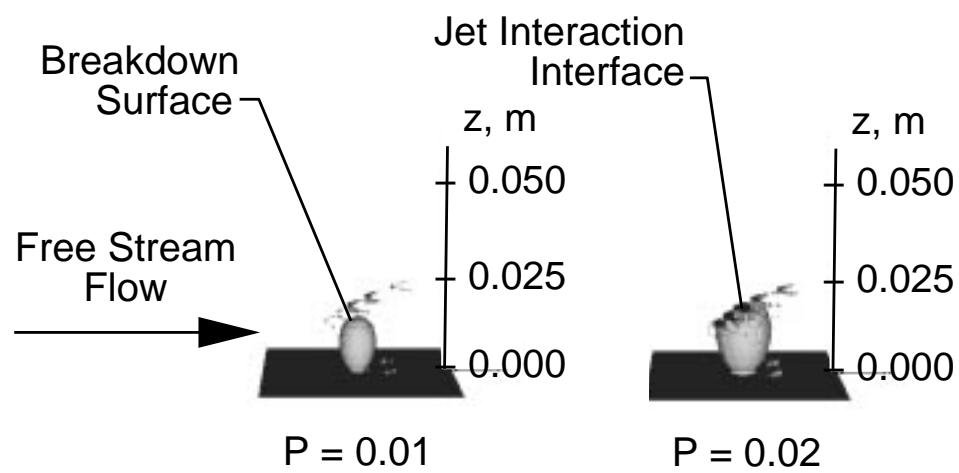


Fig. 3.9. Jet breakdown surface from CFD solution (P is the Bird breakdown parameter).

breakdown surface for the $P = 0.02$ case in Figure 3.9. Also note that the breakdown surface calculations for both $P = 0.01$ and 0.02 extend from the nozzle exit location outward. The extent of $P = 0.02$ surface at the nozzle exit, however, is larger than for the $P = 0.01$ surface and includes a portion of the region where the jet is influenced by the free stream.

For each interaction case analyzed, the breakdown parameter was varied to identify the value when the breakdown surface changed from a regularly shaped body of revolution (assumed to be unaffected by the free stream) to a body of revolution with a diagonal cut. The breakdown parameter value where this change occurs shows the interface of the expanding jet with the free stream interaction.

Because the breakdown parameter value at the interface differed for the various jet gas type and jet plenum pressure combinations, a correlation using the breakdown parameter values at the interaction interface was sought. To derive the correlating parameter, it was assumed that the physical mechanism active at the interface between the jet and free stream interaction was a ratio of flux-based quantities. By dimensional analysis, a ratio of the number density flux, nV , with the molecular collision probability flux, $\frac{\nu}{\lambda d}$, was found to provide a correlation with the breakdown parameter value at the interaction interface. The non-dimensional correlation parameter, G , is given as:

$$G = \frac{nV}{\left(\frac{\nu}{\lambda d}\right)} \quad (3.12)$$

where n is the number density, V is the characteristic flow velocity, ν is the collision frequency, λ is the mean free path, and d is the molecular diameter. Note that the molecular quantities of Equation 3.12 are taken as the hard sphere values for convenience.

Figure 3.10 shows the relationship of the breakdown parameter, which corresponds to the breakdown surface at the jet interaction interface as a function of the non-dimensional parameter, G_{jet}/G_{∞} for a free stream Knudsen number based on the orifice diameter of $Kn_d = 0.038$. Free stream influence on the relationship is obtained by normalizing the non-dimensional jet number, G_{jet} , at the jet nozzle exit conditions by a non-dimensional free stream number, G_{∞} , at the free stream gas conditions. Shown on Figure 3.10 as symbols are the breakdown parameter values determined from the twelve jet interaction CFD solutions where the isosurface of P began to be distorted by the interaction. These results span the transition from the continuum to rarefied regime based on the continuum breakdown criteria defined by Bird [11] ($P = 0.02$), which is included on Figure 3.10 as a dashed line. Above the dashed line, expanding flow at the breakdown parameter value is rarefied, whereas, below the dashed line, the expanding flow is continuum.

A solid line is drawn through the symbols in Figure 3.10. Although scatter exists between the symbols and the solid line, a general boundary between the undisturbed jet breakdown surface (region to the lower right of the solid line) and the interacting jet breakdown surface (to the upper left of the solid line) is suggested by these results. For example, the interface of the carbon dioxide jet interaction with the free stream occurs in the continuum regime, but the interface of the helium jet interaction occurs in a more rarefied regime. The solid line in Figure 3.10 is significant because it shows

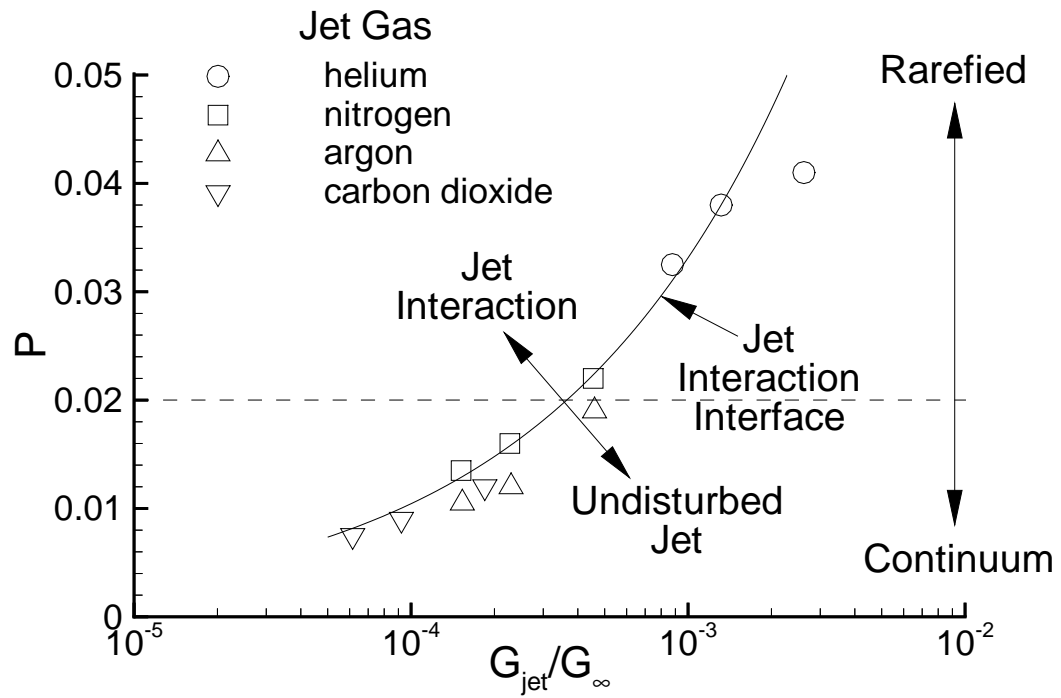


Fig. 3.10. Correlation of breakdown parameter value at jet plume breakdown surface interface with interaction for $Kn_d = 0.038$.

that a breakdown surface corresponding to a breakdown parameter value (P) in the region below the curve has not been disturbed by the interaction. Thus, the expanding jet flow can be uncoupled from the interaction at that breakdown parameter value. By uncoupling the jet flow from the interaction, a continuum flow solution of the jet can be separated from a molecular flow solution of the free stream and interaction region.

A more general correlation, including effects of wall curvature, nozzle orientation with respect to the surface and free stream, etc. may be required to define the interaction interface of more complex geometric configurations in the transitional-rarefied flow regime. However, for the present flat plate configuration with $Kn_d = 0.038$, the correlation of breakdown parameter value at the interaction interface with the non-dimensional parameter G_{jet}/G_∞ shown in Figure 3.10 can be made.

3.4 Uncoupled CFD–DSMC Jet Interaction

A detailed discussion of the steps used to produce the uncoupled CFD–DSMC solution for the jet interaction problem is given next. The continuum jet plume portion of the flow is generated by CFD, and the molecular simulation of the jet interaction by the DSMC technique. For the present study, the GASP computer program, discussed previously, applies the CFD, and the DSMC method is applied by DAC (LeBeau [44], Glass and LeBeau [30], and Wilmoth et al. [94]).

3.4.1 CFD Modeling of the Continuum Jet

The uncoupled solution for the jet interaction first requires a CFD solution for the expanding jet, which is modeled as axisymmetric and freely expanding into a vacuum. The expanding jet solution is obtained by the GASP computer program used previously for the full CFD interacting jet solution. Although the GASP program is a finite volume three-dimensional CFD solver, two-dimensional and axisymmetric solutions can be obtained by defining the computational domain with two symmetric grid planes and proper symmetry boundary conditions on the planes (McGrory et al. [49] and AeroSoft [2]). This was done for the present axisymmetric jet solutions. The GASP jet solutions used the full Reynolds averaged Navier–Stokes equations.

Modeling of the axisymmetric nozzle is similar to the nozzle modeling for the interacting jet cases. That is, flow at the plenum temperature and pressure was allowed to expand through a converging nozzle to the sonic condition at the exit. However, rather than interacting with a free stream flow, the jet flow from the nozzle exit was allowed to expand further as a plume into an outer computational domain, which simulated an infinite vacuum. A first-order extrapolation from the interior was specified as the outflow boundary condition for the computational domain. Wall temperature was held constant at 300K and a no-slip condition was applied to the nozzle and outer region walls.

One of the symmetry planes of the computational domain for the expanding axisymmetric jet is shown on the left side of Figure 3.11. Shown on the right side of the figure are normalized number density contours from the CFD solution. Note that along the outflow boundary, the number density is reduced by at least four orders of magnitude

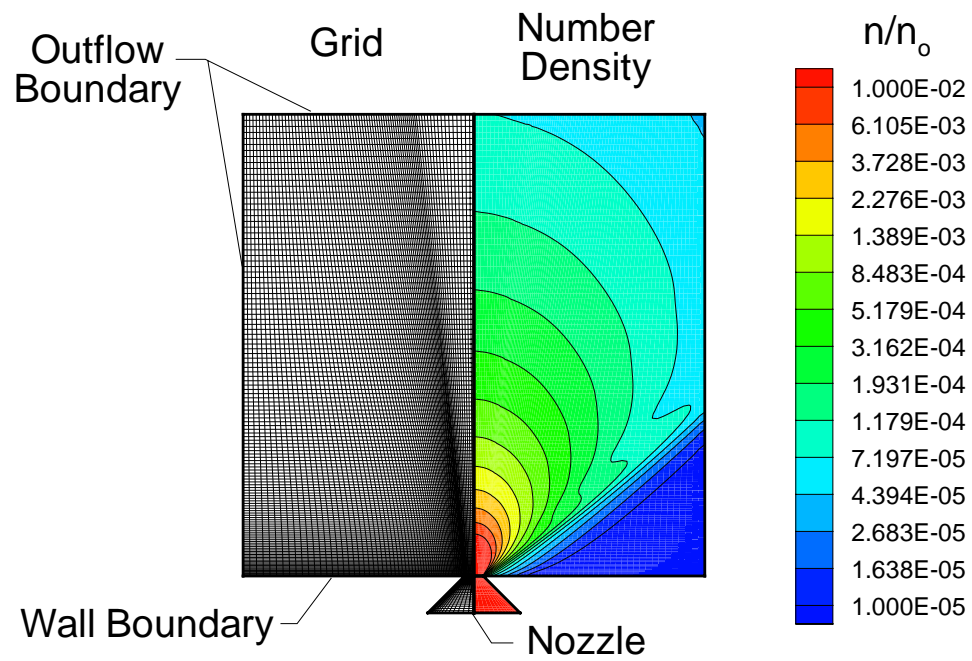


Fig. 3.11. CFD grid and number density contours for axisymmetric free expanding jet.

from the plenum condition. The extent of the upper computational zone was chosen so that the expanding jet transitioned from continuum to rarefied flow before reaching the outflow boundary, which assured that a jet plume continuum surface could be defined within the computational domain.

3.4.2 Surface Triangulation for DSMC

A non-interacting plume surface for the expanding jet is obtained from the CFD solution, which was first processed to produce a breakdown parameter PLOT3D solution file. The breakdown parameter value was chosen so that the plume did not extend into the interaction region for the free stream flow with a Knudsen number of $Kn_d = 0.038$. Based on results from Figure 3.10, a value of $P = 0.01$ fit this criteria. An analysis of breakdown parameter file by the EnSight program (CEI [15]) provides the geometry of the non-interacting plume surface as a cloud of points.

Although the pointwise description given by the EnSight program correctly maps the continuum jet plume at the proper Bird breakdown parameter value, the format is not compatible as a DAC geometric surface description. The preprocessor program of DAC requires a description of all surface geometries as groups of triangulated surfaces. To create the geometry file for the present solution, the flat plate geometry and the non-interacting plume surface must be merged together in a format readable by the DAC preprocessor program.

Several software packages were required to process the geometry of the flat plate model and jet plume to produce the proper triangulated format. First, the cloud of points representing the jet plume surface was transformed to an initial graphics exchange

specification (IGES) format (Smith et al. [78]), one that is common for most computer aided design (CAD) programs. A commercially available software program, Surfacr (Imageware [39]), was utilized to produce IGES formatted surface descriptions.

To create the geometry of the flat plate model and combine it with the jet iso-surface, another computer program, GridTool (Samareh [73]), was used. GridTool allows external geometric descriptions of different formats (IGES, GRIDGEN, LaWGS, PLOT3D) to be merged together with geometries created within the GridTool program. The program generates a group of surface patches with the same format that describe the entire surface geometry of interest. For the present study, the flat plate geometry, created with the GridTool program, was merged with the IGES jet plume surface obtained with the Surfacr program. A FELISA (Peirò et al. [60]) input file is generated as an output option by the GridTool program. FELISA is an unstructured finite element surface and volume grid generation program (See Peirò et al. [60] for a complete discussion of FELISA.). For the present application, however, only the FELISA surface triangulation routine was used. Triangulation density of the surface is controlled by distributing sources with the GridTool program, which are read by the FELISA surface triangulation routine.

One final step was necessary to provide a compatible DAC formatted surface description for the molecular simulation. An author written translation and boundary condition application computer program, *ftodac*, was applied to the FELISA output file. All surface points, the number of triangles of the surface, and triangle connectivity are rewritten from a FELISA to DAC type format by *ftodac*. Additionally, appropriate solid wall and jet plume surface boundary conditions are assigned to each triangle. All

solid walls of the flat plate are treated as non-catalytic, fully diffuse surfaces with full momentum and energy accommodation. The jet plume surface is treated as an outgassing boundary with the number density, velocity, and temperature of the jet assigned to the proper boundary location. The outgassing boundary condition of the plume also assures that molecules outside the plume that are moving toward the plume surface are allowed to pass out of the DSMC domain and are removed from the simulation. Boundary conditions for the jet plume surface are interpolated from the original structured grid GASP PLOT3D solution file by a weighted distance squared subroutine of the *ftodac* program.

Shown in Figure 3.12 is the triangulated surface description of the flat plate and jet plume surface for the argon jet interaction that was generated by the FELISA program. Shown in the figure is the full geometry; however, for the simulation, only half of the geometry was used because of symmetry at the plate center line. In the right upper corner of the figure is a closeup view of the argon jet plume surface, which consists of 7,200 triangles (of which 3,600 were used because of symmetry). Note the dense surface triangulation of the surface near the jet exit. The closely spaced triangles allow a more detailed geometric and boundary condition description of the jet plume surface in the region where flow gradients are high. Also, the flat plate (to one side of the symmetry plane) was described by 25,000 triangles with over 12,000 triangles on the upper surface to produce the desired surface sampling about the jet interaction region.

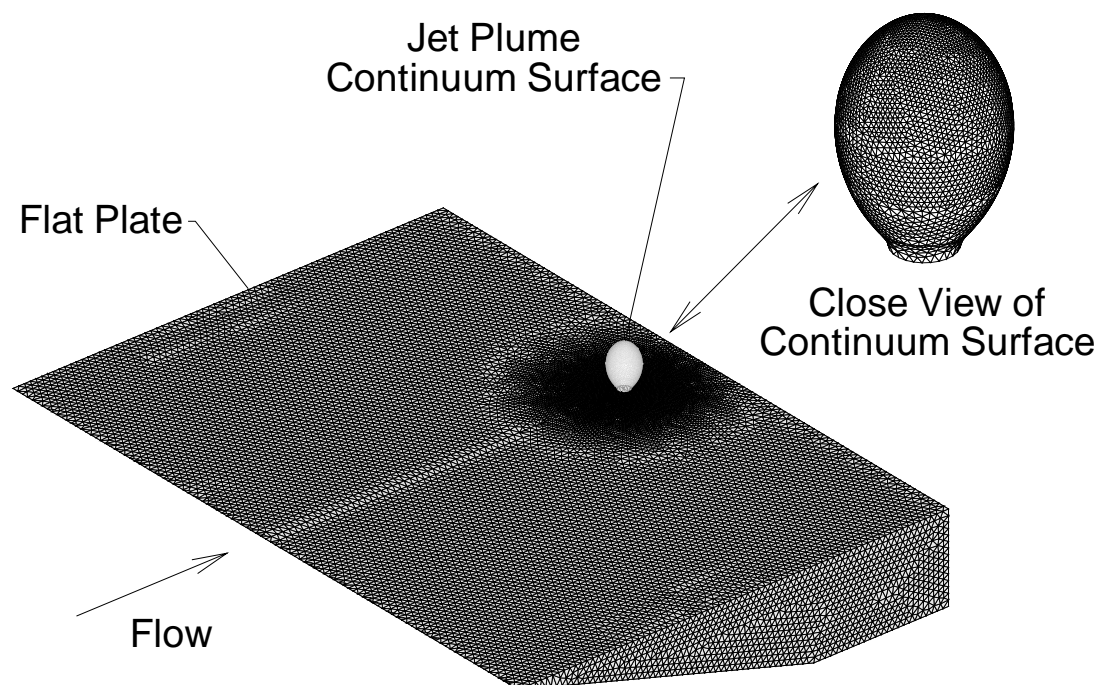


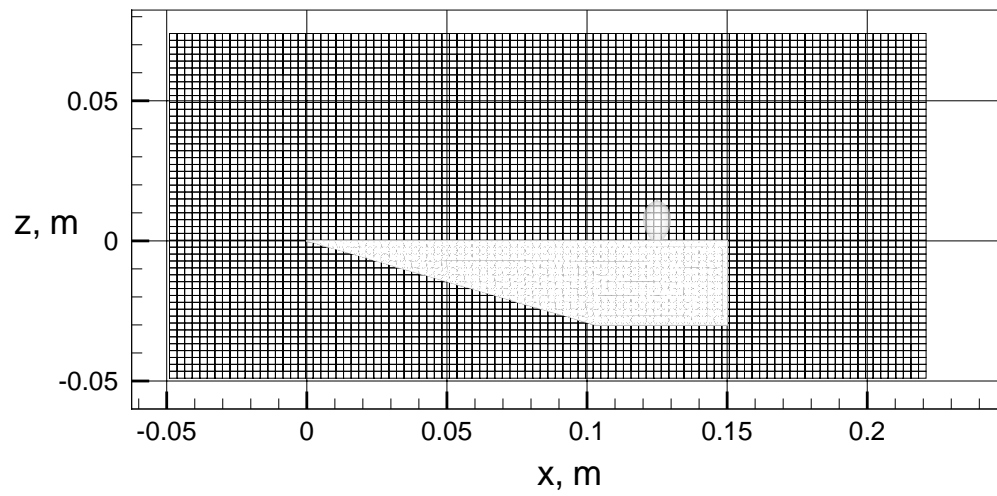
Fig. 3.12. Triangulated flat plate and jet plume continuum surface geometries.

3.4.3 DSMC Modeling of the Interacting Flow Field

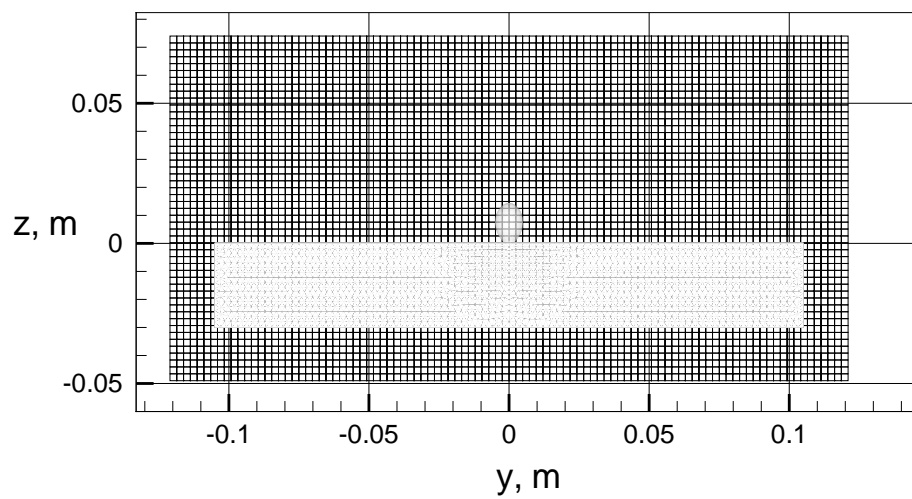
After the geometry and boundary conditions of the surface for the molecular simulation are defined, the DSMC domain size and the domain boundary conditions must be specified. The DSMC domain size was chosen to entirely surround the flat plate model (above, below, and to the side) to simulate the experimental conditions more closely than if just the upper portion of the plate flow field were modeled. The extent of the DSMC domain is shown in Figure 3.13. A free stream boundary condition is applied to all domain boundary faces except the symmetry plane where a symmetry boundary condition was applied.

To produce the DSMC solution, the grid adaptation scheme provided by the DAC series preprocessor (*predac*) is employed. The *predac* program initially generates a uniformly spaced Cartesian grid of so-called level I cells for the initial molecular simulation. Triangulated surfaces that model the geometry clip the Cartesian grid, and the volumes of the clipped Cartesian cells are determined for use in computing flow properties. The uniform grid solution, which is produced from the initial simulation, resolves large scale flow field features. Level II cells with finer grid spacing in regions of high number density are generated for subsequent adaptation cycles based on the previous grid solution. Level II cell spacing within level I cells is controlled by user input to the *predac* program. The grid adaptation process may be applied as needed to each flow field solution to produce the desired degree of cell resolution.

A uniform grid and three grid adaptation cycles were applied to produce the present DSMC jet interaction molecular simulation. The uniform Cartesian grid for the



a) Side view, grid at $y = 0.000 \text{ m}$.



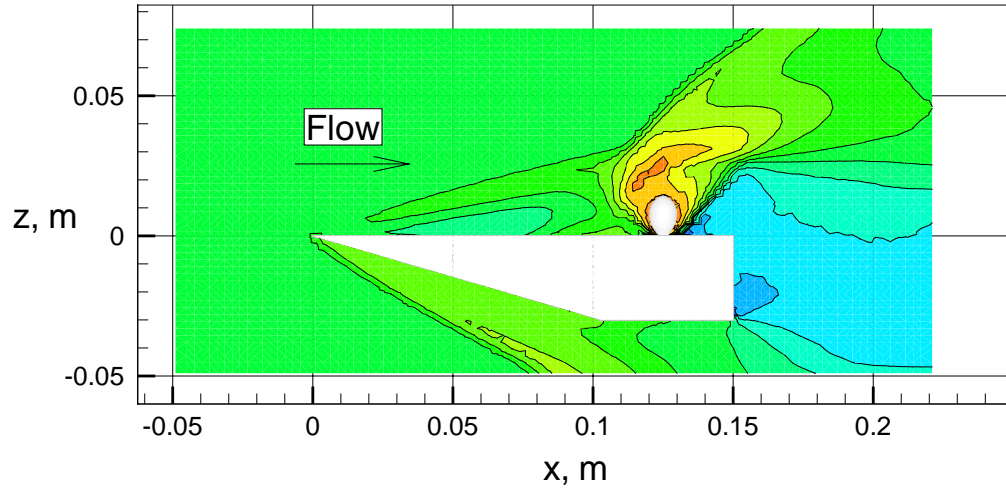
b) End view, grid at $x = 0.125 \text{ m}$.

Fig. 3.13. Uniform grid for DSMC jet interaction simulation.

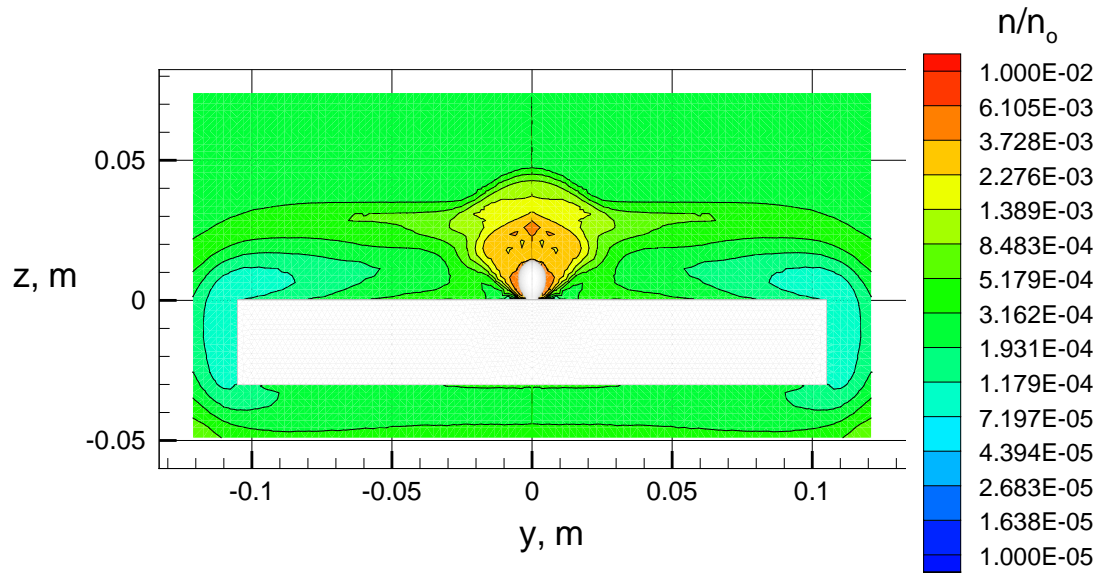
simulation is shown in Figure 3.13. Two planes of the Cartesian grid are shown: a cross flow grid that intersects with the jet breakdown surface at $x = 0.125$ m and a streamwise grid along the symmetry plane at $y = 0$ m. Note that the flat plate and non-interacting jet plume surfaces are shown colored white in the foreground of the figure on the grid.

The uniform Cartesian grid consisted of 250,000 cells; however, the volume of the flat plate and plume continuum surface clip out about 15,000 cells of the domain resulting in about 235,000 active cells for the simulation. About 2.64 million simulated molecules were necessary to fill the cells with an average of about ten molecules per cell. After an initial transient period to equalize the number of inflow and outflow molecules in the DSMC domain, approximately five thousand time steps were performed before the simulation was stopped, which allowed 2,500 sampling cycles to be obtained. Typically, sampling is performed every other time step in DSMC to avoid a bias from the random number generation process. The uniform grid simulation required 300 Mbytes of computer memory and executed for 232 node hours using SGI R10000 CPUs.

Number density contours from the uniform grid solution are shown in Figure 3.14 at the same planar locations as the grid shown in Figure 3.13. These contours reveal the large scale features of the flow field. Upper and lower plate shock waves that originate at the plate leading edge, the higher number density region near the continuum jet plume surface, and the low number density region in the wake downstream of the flat plate are evident in Figure 3.14a. Also note that these same general features on the symmetry plane are shown by the CFD solution presented in Figure 3.8. The end view cross flow plane at the jet nozzle location (See Figure 3.14b.) shows the extent of the jet interaction



a) Side view, grid at $y = 0.000$ m.



b) End view, grid at $x = 0.125$ m.

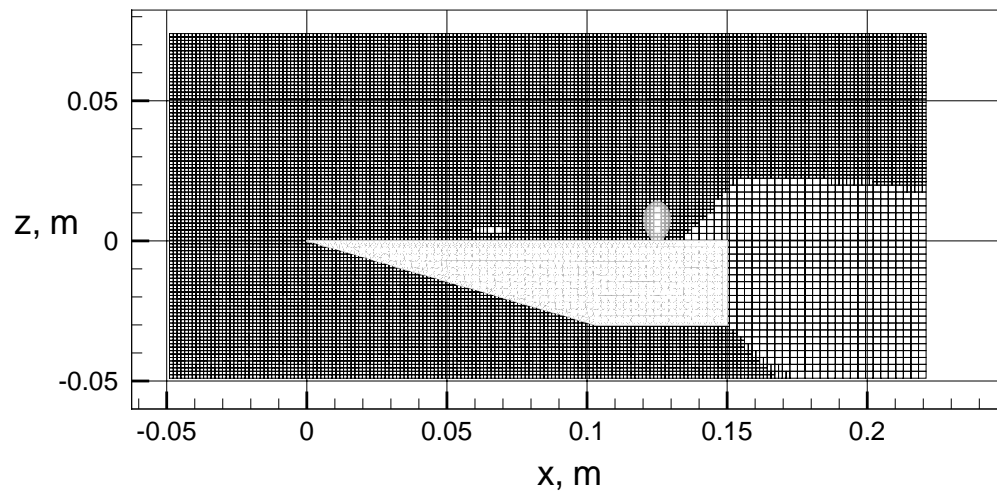
Fig. 3.14. Number density contours from the uniform grid solution.

disturbance above the plate, the flow about the plate side walls, and the flow under the plate.

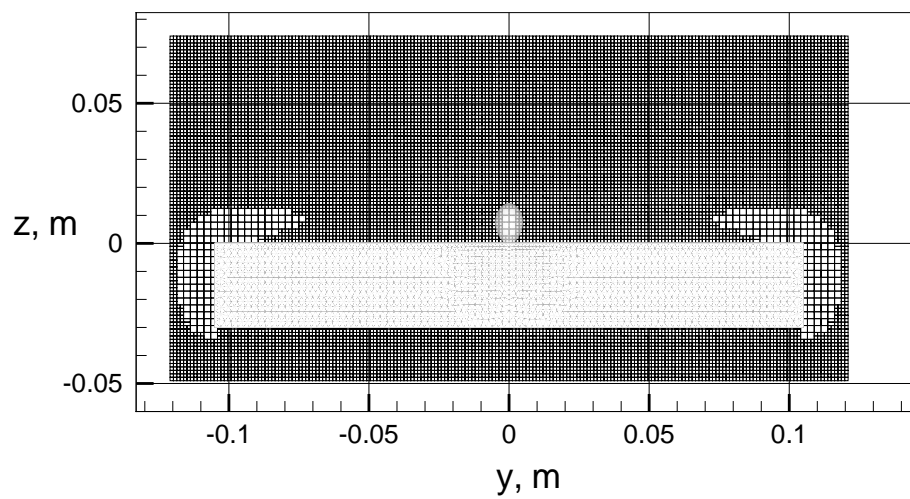
Based on the uniform grid solution, the first adapted grid was produced by *predac* with the same number of level I cells as the uniform grid; however, the adaptation process allowed level II cells (inner cells) to be created within the level I cells. The resulting DSMC domain consisted of about 1.6 million level II cells with about 26 thousand cells clipped out because of the volume occupied by the flat plate and breakdown surface. Grid planes at $y = 0$ m and $x = 0.125$ m are shown in Figure 3.15. Generally, the result of the first grid adaptation was to increase grid density uniformly throughout the computational domain, except, for example, in the plate wake and side wall regions where the number density of the uniform grid simulation was lower than the free stream.

The DSMC method was then applied to the adapted grid. Simulated molecules within the cells of the DSMC domain numbered about sixteen million. The simulation was run for five thousand time steps after a steady condition was met to collect samples and required 1.25 Gbytes of computer memory and executed for 971 node hours on SGI R10000 CPUs. Number density contours corresponding to the grid plane locations of the previous figure are shown in Figure 3.16. The number density contours reveal similar flow features as the uniform grid solution, except more of the fine detail is apparent. In comparing Figures 3.14 and 3.16, the near jet flow field gradients are shown in greater detail for the adapted grid solution than for the uniform grid solution.

Because the memory requirements for the next grid adaptation and simulation cycle exceeded the available memory of the local SGI R10000 CPUs, an alternate computer system was employed. The computer system consists of two computers: the first

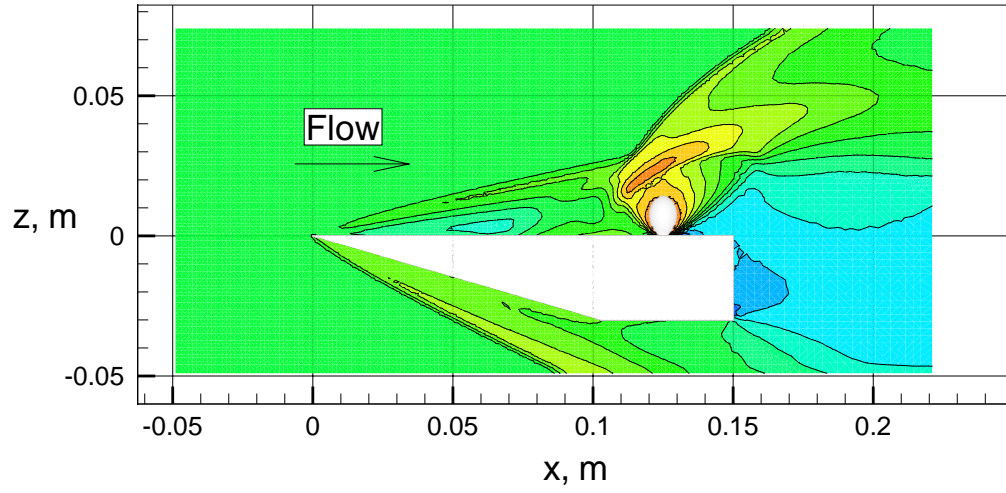


a) Side view, grid at $y = 0.000 \text{ m}$.

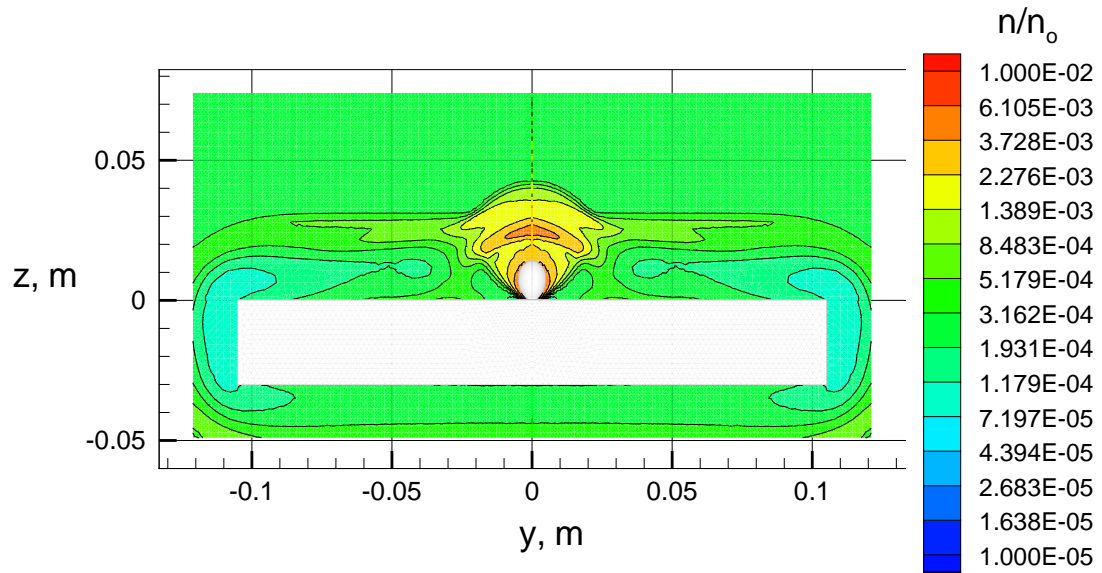


b) End view, grid at $x = 0.125 \text{ m}$.

Fig. 3.15. Grid after first adaptation for DSMC jet interaction simulation.



a) Side view, grid at $y = 0.000$ m.



b) End view, grid at $x = 0.125$ m.

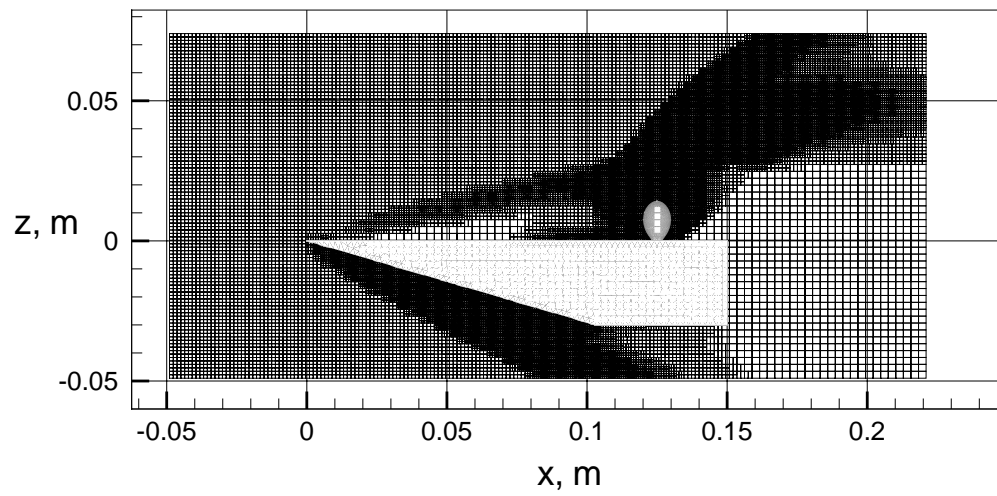
Fig. 3.16. Number density contours from first adapted grid solution.

is an SGI Onyx CHALLENGE with two Gbytes of main memory to execute *predac*, the DAC series preprocessor, and the other is part of the NASA High Performance Computing and Communications (HPCC) Program, a 1024 processor element SGI/Cray T3E to execute *ddac*, the parallel version of the current DSMC code. Each processor element of the T3E multi-processor computer is a Digital Equipment Corporation Alpha RISC chip. Both computers are located at the NASA Goddard Space Flight Center.

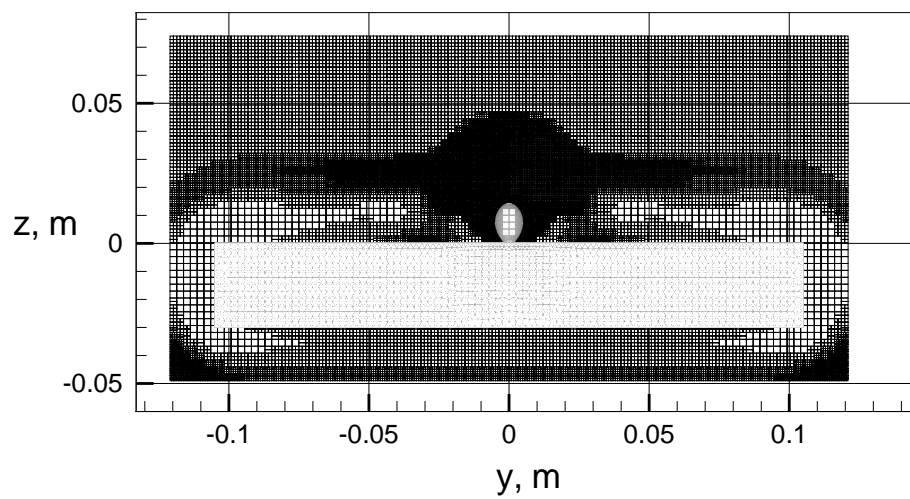
The second grid adaptation, based on the results from the first adapted grid simulation, was performed on the alternate computer system. The number of level I cells was held constant, but the maximum number of level II cells in each level I cell was increased by a factor of two in all coordinate directions. Two planes, which represent the resulting grid resolution from the second adaptation, are shown in Figure 3.17. The DSMC domain for the second adaptation consists of 3.35 million level II cells with 85 thousand cells clipped because of the volume occupied by the flat plate and continuum jet plume.

For this adaptation cycle, note that the grid shown in Figure 3.17 better represents the number density contours from which it was derived (See Figure 3.16.) than for the the previous adaptation cycle (Compare Figures 3.15 and 3.17.). The difference between the two grid cycles results because the first adaptation cycle was based on a uniform grid simulation with coarse resolution of the flow field and a greater number of level II cells within each level I cell was allowed for the second adaptation cycle.

A simulation was performed on the second adapted grid, which required 34 million molecules and about 3.5 Gbytes of computer memory. Computer execution time was 1980 node hours on the SGI/Cray T3E using either 128 or 256 processor elements, depending



a) Side view, grid at $y = 0.000$ m.



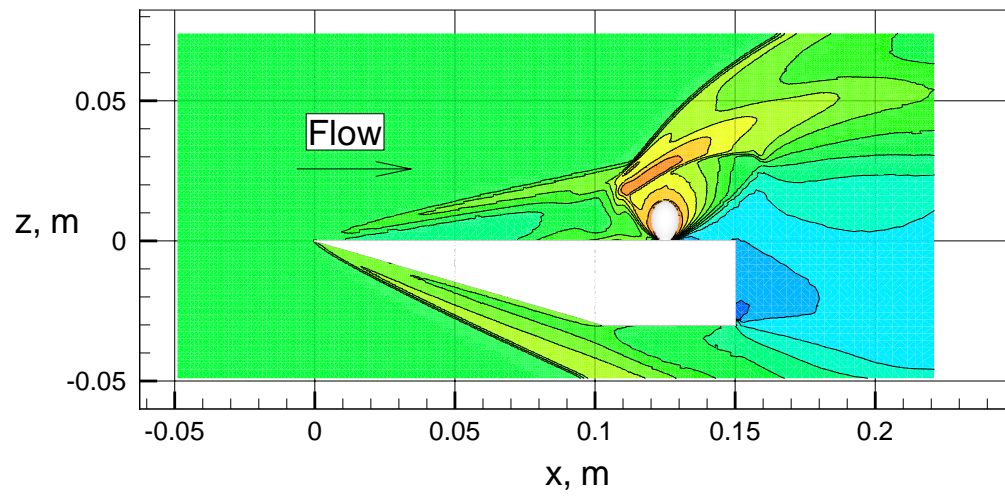
b) End view, grid at $x = 0.125$ m.

Fig. 3.17. Grid after second adaptation for DSMC jet interaction simulation.

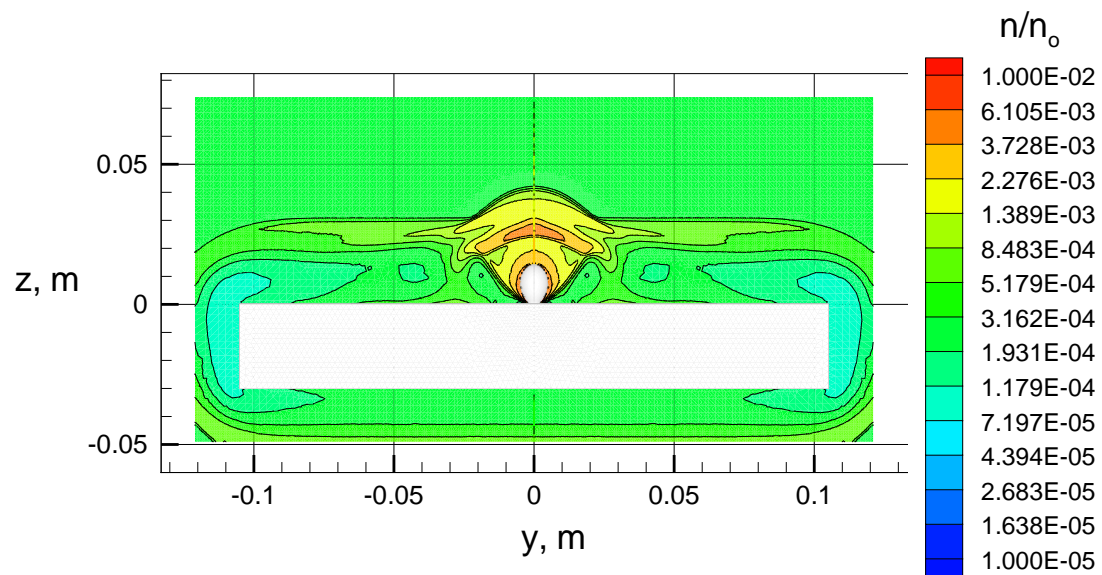
on the computer queue availability. Execution of the simulation was stopped after 2500 steady-state samples were obtained.

Number density contours from the simulation on the second adaptation grid at the grid cut planes of Figure 3.17 are shown in Figure 3.18. Greater detail is shown by the number density contours in the near jet region than with the previous solutions. The forward jet interaction compression region shown in Figure 3.18a is more pronounced with a stronger density gradient than the previous solution, which is evidenced by closer spaced number density contours than before.

Based on the memory requirements of the second grid adaptation and simulation cycle and on several trial attempts with the DAC preprocessor, grid refinement for the third adaptation was chosen to maximize the number of level II cells near the upper wall surface to increase solution confidence in this region by minimizing the number of cells elsewhere. To accomplish this, the *predac* program was modified so that cells of one mean free path normal and two mean free paths lateral to the upper plate surface were allowed for the first four level I cells closest to the upper plate surface to concentrate fine grid in this region. Below the second level I cell in the $-z$ -direction from the plate surface, no level II cells were allowed, and elsewhere in the domain, level II cells were limited to a minimum of four mean free path spacing in all directions. Although cells less than one mean free path are recommended by Moss et al. [53] to resolve hypersonic viscous interaction surface properties with the Bird G2 DSMC code [10], for the present simulation, larger cell spacing based on the study by Moss et al. [53] was unavoidable because the resultant number of simulated molecules would cause the problem to be intractable, even on the SGI/Cray T3E, one of the largest multi-processor computer systems available. Therefore,



a) Side view, grid at $y = 0.000$ m.



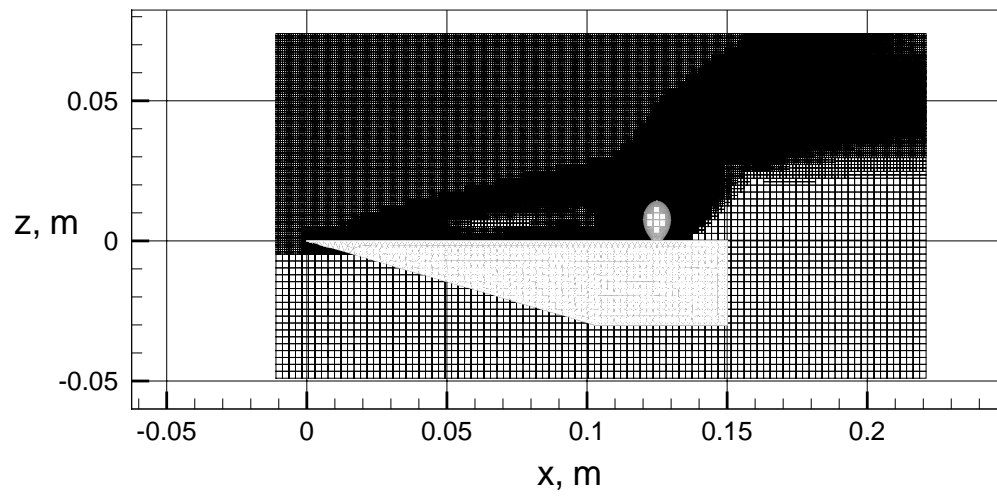
b) End view, grid at $x = 0.125$ m.

Fig. 3.18. Number density contours from second adapted grid solution.

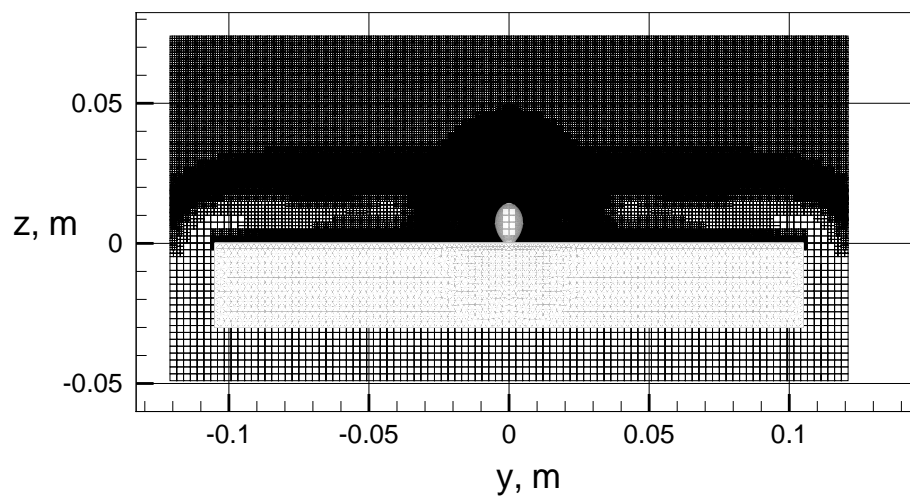
a trade-off of modifying the grid to provide smaller dimensioned grid spacing normal to the plate surface was made by sacrificing grid resolution elsewhere as described previously to maximize accuracy of sampled surface properties on the upper portion of the plate obtained from the molecular simulation.

The resulting grid is shown in Figure 3.19a and b at the symmetry plane ($y = 0$ m) and at the nozzle centerline from the end view ($x = 0.125$ m), respectively. Fine spacing of the plate leading edge compression wave location is shown in Figure 3.19a. Also, fine grid is shown in Figure 3.19a and b along the location of the flat plate boundary layer and near the jet plume and interaction regions. Note that in some regions along the surface, cell spacing is more coarse than at other regions. These regions are above the plate surface nearly midway between the plate leading edge and jet nozzle (Figure 3.19a, $x \approx 0.06$ m), near the plate side wall (Figure 3.19b, $y \approx \pm 0.1$ m), and under the plate upper surface. Cell spacing variation in the region above the upper plate surface was affected by changes in the local mean free path of the flow field, which was based on the previous adapted grid solution; however, coarse cell spacing below the plate surface was caused by the modifications to the DAC preprocessor code, which allowed no level II cells at a designated z-location below the plate surface.

Preprocessing for this grid adaptation cycle produced nearly 14 million cells with about 640 thousand cells clipped because of the triangulated jet plume and flat plate geometry. A molecular simulation was performed on the grid, which is shown in Figure 3.19. The simulation required 14 Gbytes of computer memory for the 134.5 million molecules at the steady state condition. Computer execution time was 21 thousand node



a) Side view, grid at $y = 0.000$ m.



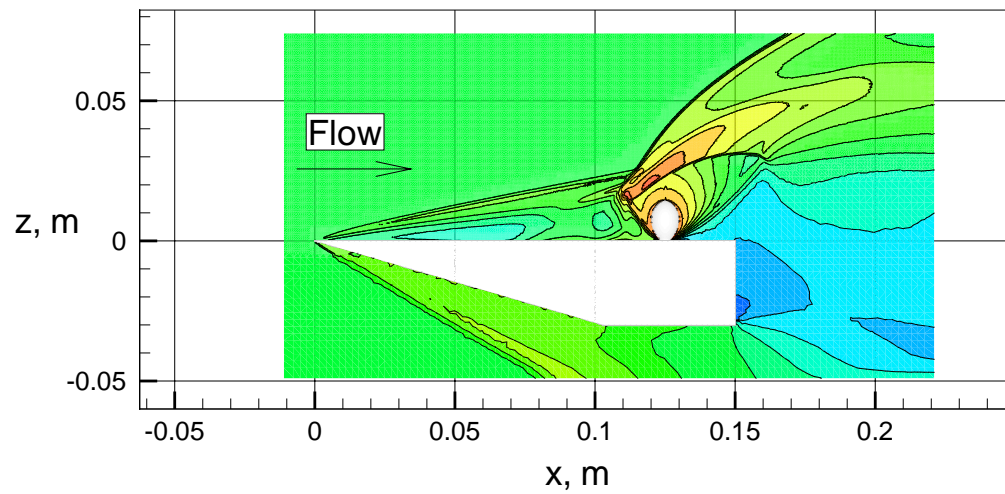
b) End view, grid at $x = 0.125$ m.

Fig. 3.19. Grid after third adaptation for DSMC jet interaction simulation.

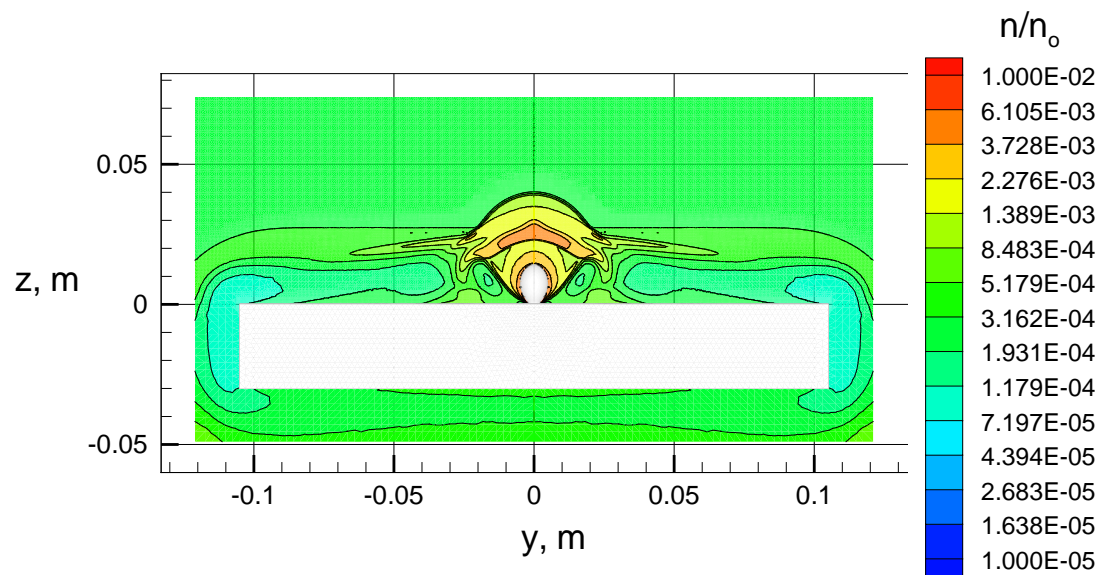
hours on the SGI/Cray T3E using 512 processor elements. After 2500 steady state time step samples were obtained, execution of the simulation was halted.

Number density contours are shown in Figure 3.20 at the same planar locations as the grid shown in Figure 3.19. Flow features similar to those produced by the previous adaptation cycle are shown by the present simulation. Above the plate, large scale flow features such as the jet interaction compression, the plate leading edge compression, and the jet expansion aft of the plume are nearly the same; however, detailed fine features, which are just present with the second adaptation, are more prominent with the third adaptation. For example, the low density region forward of the jet plume and the low density structure to the side of the jet plume are resolved better for the third adapted grid solution (Compare Figure 3.18 with Figure 3.20.).

Although the DSMC portion of the jet interaction simulation at the experimental test condition required an extensive amount of computational resources, it is important to note that if the continuum fluid inside the plume breakdown surface were included in the molecular simulation, many more cells and simulated molecules would be needed. A calculation using properties of the continuum portion of the jet flow inside the $P = 0.01$ surface was performed with the local mean free path as a guide to determine the estimated DSMC resources for such a simulation. To model the continuum portion of the jet to the symmetry plane with mean free path resolution, 0.33 trillion (0.33×10^{12}) cells and 3.3 trillion simulated molecules would be required, which clearly exceeds current and near future computational capabilities. Thus, by providing a CFD solution to the $P = 0.01$ jet breakdown surface, the problem size is reduced considerably.



a) Side view, grid at $y = 0.000$ m.



b) End view, grid at $x = 0.125$ m.

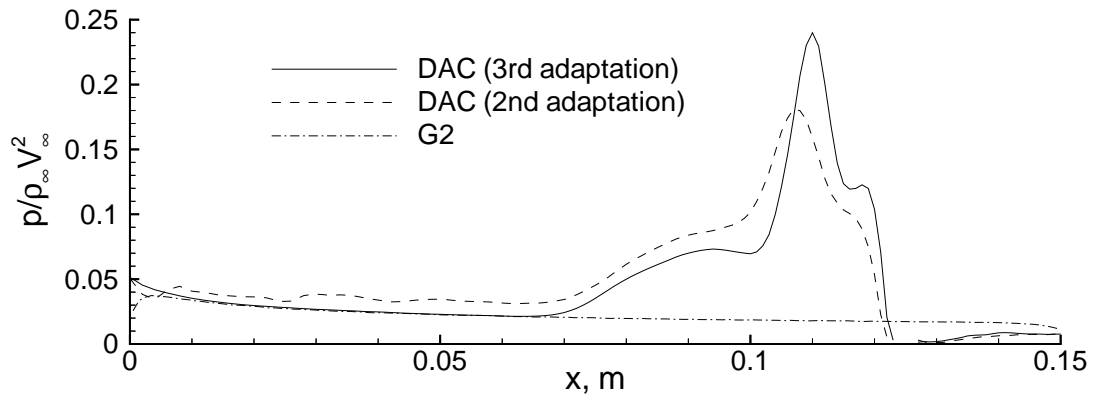
Fig. 3.20. Number density contours from third adapted grid solution.

3.4.4 Analysis of DSMC Results

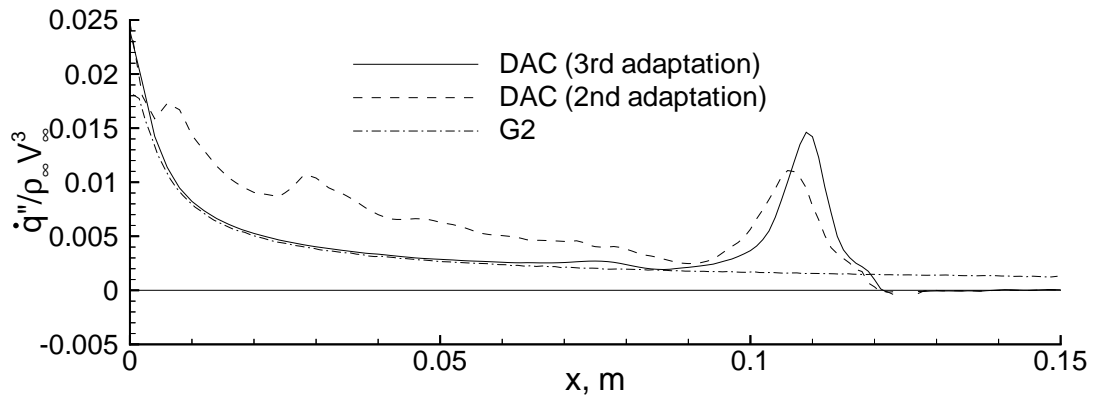
An analysis of the uncoupled CFD–DSMC flat plate jet interaction solution is presented in this section. Comparisons are made between the 2–D G2 flat plate no-jet solution, the second adapted grid solution, and the third adapted grid solution. These comparisons help to validate the present solution technique as producing a credible jet interaction solution. It will be shown that the third adapted grid provides an adequate simulation of the flat plate jet interaction. Also presented is a discussion of the jet induced flow separation and attachment on the plate surface and the character of the local jet interaction flow field.

A further comparison of the present numerical results with the experimental data of Warburton [88] was sought. Unfortunately, the data were not available at the time of this writing. Therefore, only those comparisons discussed above are presented subsequently in this section. Nonetheless, given in the Appendix is a tabulation of the normalized number density, velocity components, and temperature on the symmetry plane and the normalized pressure, shear stress components, and heat flux on the upper plate surface from the present jet interaction numerical study that can be compared with the experimental results of Warburton when they become available.

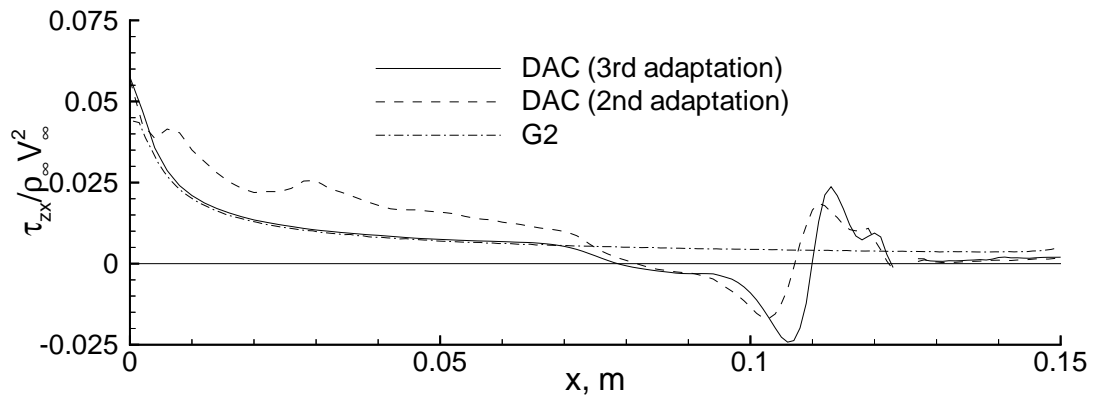
Surface pressure, heating, and shear stress from the 2–D G2 flat plate no-jet solution, the second adapted grid solution, and the third adapted grid solution on the symmetry line of the upper flat plate surface are presented, in Figure 3.21a, b, and c. In the figure, uncoupled CFD–DSMC results of the third adapted grid are shown by a solid line; results of the second adapted grid are shown by a dashed line, and the G2 DSMC



a) Normalized pressure.



b) Normalized heating.



c) Normalized shear stress.

Fig. 3.21. Comparisons of pressure, heating, and shear stress on the flat plate surface at the symmetry line.

results are shown by the dot-dashed line. Pressure and shear stress are normalized by the free stream momentum flux, $\rho_\infty V_\infty^2$, and heat flux is normalized by twice the free stream kinetic energy flux, $\rho_\infty V_\infty^3$. The heat flux vector is positive for heat flow from the fluid to the plate surface and negative for heat flow from the plate surface to the fluid. For the wall shear stress, τ_{zx} , a positive value indicates a shear force in the positive x-direction, that is, in the direction of the free stream flow.

As the free stream flow encounters the plate leading edge, a viscous boundary layer develops. The three results shown in Figure 3.21 differ in this leading edge region. The second and third adapted grid solutions predict higher leading edge pressure, heating, and shear stress than does the G2 code. The G2 code provides a more accurate simulation in the region near the plate leading edge because cell resolution normal to the plate surface was at least one-quarter of the local mean free path, which allowed better resolution of the highly rarefied flow about the sharp leading edge (See the discussion in Section 3.2.2.).

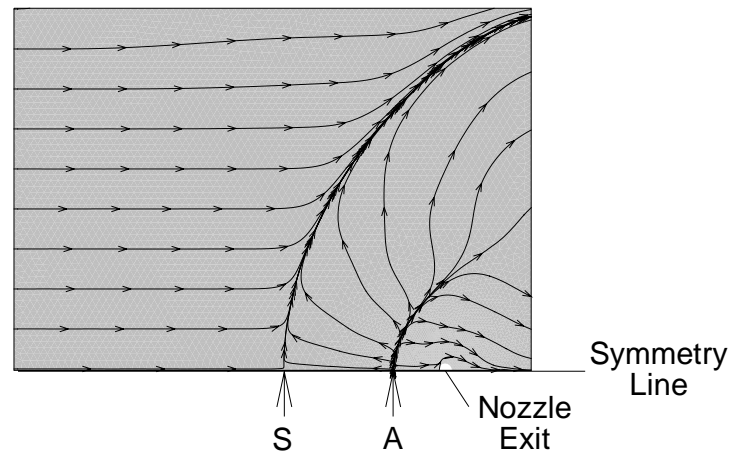
Away from the influence of the sharp leading edge, good agreement exists between the G2 code and third adapted grid uncoupled CFD-DSMC simulations. As shown in Figure 3.21, downstream of the plate leading edge to a location of $x \approx 0.07$ m, the normalized surface pressure, heating, and shear stress predictions are nearly identical for the two solutions. The results of the second adapted grid simulation, however, do not compare well, and for each surface quantity (pressure, heating, and shear stress), a greater value is predicted than from the other two simulations. Inadequate cell resolution of the second adapted grid case probably allowed simulated molecules to encounter the wall with too much momentum and energy. With adequate cell resolution near the wall, molecules collide sufficiently within the cells to properly balance the local momentum

and energy before striking the wall. Additionally, because the third adapted grid and G2 code solutions agree over the forward portion of the plate, cell spacing of one mean free path normal to the wall for the third adapted grid simulation is shown to be adequate for the present simulation.

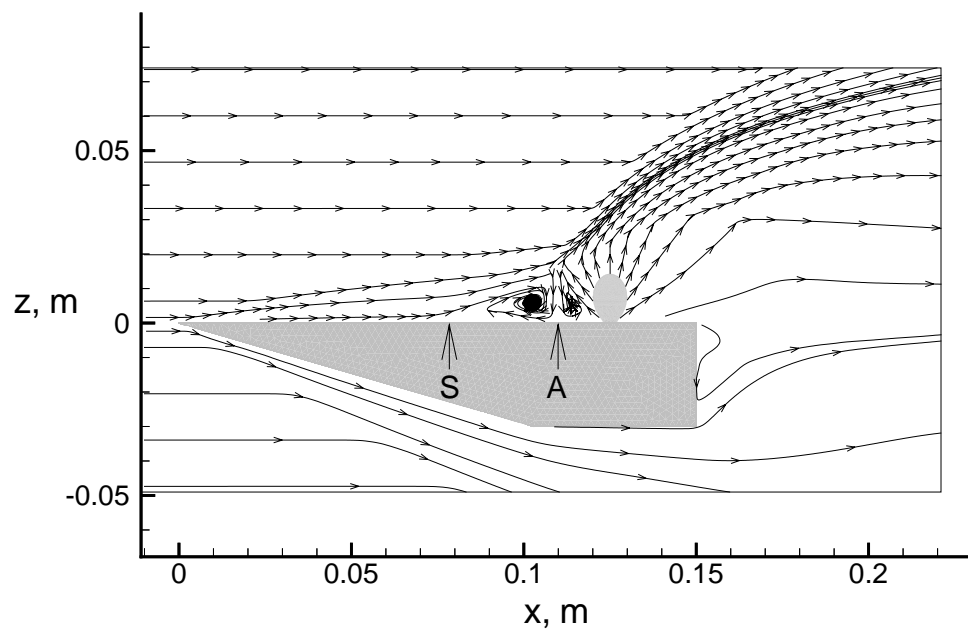
For an x location greater than about 0.07 m, results in Figure 3.21 show the G2 code prediction of pressure, heating, and shear stress changes little to the end of the plate because the simulation is for a flat plate with no jet interaction. However, as shown by the results for the uncoupled CFD–DSMC simulation, the local pressure, heating, and shear stress are greatly influenced by the jet interaction as indicated by the rapid increase in pressure and heating ahead of the jet nozzle exit location at $x = 0.125$ m. Shear stress, however, decreases to a negative value for $0.078 < x < 0.110$ m before becoming positive closer to the nozzle exit. Wall shear stress indicates the local flow direction; reversal of the shear stress indicates flow separation.

The wall shear stress direction is shown more clearly with the aid of Figure 3.22a, simulated oil flow streaks on the plate surface and Figure 3.22b, flow streamlines at the symmetry plane. To create the surface oil flow pattern in the figure, wall shear stress from the molecular simulation in the x and y directions, τ_{zx} and τ_{zy} respectively, define surface vectors on the flat plate, and streamlines, introduced on the plate surface by the visualization software [5], follow the local shear stress vector field. Thus, the lines show the direction of the local skin-friction.

Peake and Tobak [59] have assembled an extensive glossary and explanations for the topology of many skin-friction patterns on bodies, which encounter high speed flow. Based on their topological rules, two distinct features are noticeable on Figure 3.22a: At



a) Simulated oil flow on starboard flat plate surface (top view of x-y plane).



b) Flow streamlines at symmetry plane (side view of x-z plane).

Fig. 3.22. Flow separation and attachment caused by the flat plate jet interaction.

the point on the symmetry line where the oil flow lines converge (labeled S), a line of separation is apparent; Also, the symmetry plane streamline figure (See Figure 3.22b.) shows that at point S, streamlines lift from and separate off the plate surface just upstream of two counter-rotating vortices. Peake and Tobak [59] explain that the flow along a line of separation leaves the surface as a free shear layer. A line of attachment is also shown in Figure 3.22a and is labeled as point A at the symmetry line. Along the line of attachment, oil flow lines diverge because the local flow is directed downward at the surface and spreads laterally. At the point labeled A, shown in Figure 3.22b, the shear layer flow between the counter-rotating vortices impinges on the plate surface and the flow on either side is directed upstream and downstream respectively.

The jet, injected at the $P = 0.01$ plume surface, acts as a three-dimensional protuberance to the incoming free stream causing the flow to separate and creating the counter-rotating vortices (See streamlines in Figure 3.22b.) located within a separation region on the upper flat plate surface just upstream of the jet plume. The forward vortex turns the free stream flow above the local jet interaction region, and a jet induced vortex (just aft of the forward vortex) entrains the jet gas. These two vortices are shown by the streamlines in Figure 3.22b just above the upper plate surface and upstream of the nozzle exit location.

The streamlines of Figure 3.22b show that the jet flow also has a prominent influence on the upper free stream flow. The flow above the flat plate is turned and the streamlines are compressed by the jet. Flow turning of the free stream caused by the jet is maintained until it exits the computational domain. Likewise, the jet flow streamlines are compressed by the interaction with the free stream. Jet streamlines are

abruptly turned downstream by the interaction. Also, flow directly behind the jet on the symmetry plane is at a lower pressure than the flow beneath the plate as evidenced by the streamlines passing below the flat plate turning upward through the plate wake region.

As shown by the number density contours of Figure 3.20, the nitrogen free stream inflow condition is about four orders of magnitude less dense than the standard number density. As the free stream encounters the upper flat plate surface, it is initially compressed by the boundary layer displacement to create a leading edge shock wave. Over the upper portion of the flat plate past the leading edge, the gas density decreases as a boundary layer develops and the gas temperature near the wall increases from viscous dissipation (Note, however, that the density within the Knudsen layer will increase because of the lower wall temperature.). The density of the near wall gas then increases at the separation region as it recompresses before either being directed above the separation region or entrained into the forward vortex upstream of the jet plume.

Initially, the jet flow just outside the non-interacting plume surface expands as shown in Figure 3.20. However, as the jet encounters the free stream flow, it compresses as shown by the higher number density region just above the jet. This higher density region is caused by the interaction between the free stream flow and jet. As discussed previously, the jet flow turns the free stream. The resultant compression can be seen in the figure as the outer curved number density contour, which intersects the upper computation domain near the downstream boundary. In addition, number density in the region downstream of the nozzle exit just above the flat plate surface decreases with

distance, indicating a low pressure wake has formed behind the jet and high density interaction compression.

Number density contours below the plate show the influence of the underside compression surface. Flow beneath the plate is initially compressed by the shock wave created by the wedge geometry of the lower surface leading edge; however, as the flow reaches the end of the lower wedge compression surface, it expands, and the number density decreases. The flow then exits either through the lower or downstream computational boundary.

From this analysis of the interacting flow field, the pressure and heating distributions along the symmetry line (See Figure 3.21a and b.) can be better explained. As the local flow over the plate encounters the separation line, it is turned upward away from the plate and compressed as shown in Figure 3.22b, hence the rise in pressure at $x \approx 0.07$ m. The maximum surface pressure occurs at the flow attachment point ($x = 0.110$ m), and is influenced by both the free stream compression from the jet interaction above and the flow impingement at the attachment line of the counter-rotating vortices. As shown in Figure 3.21b, with increasing distance from the leading edge, heating in the separated flow region first has a lower maxima and decreases at the forward vortex location; at the vortex attachment, heating increases to a higher maxima. One possible explanation is that the forward vortex gains kinetic energy by momentum transfer from the free stream as it traverses the upper portion of its path. An energy balance occurs between the forward and jet induced vortices during the path down toward the flow attachment point where energy is released as a heat flux to the wall causing the higher maxima. As the

vortical flow traverses from the attachment line upstream and downstream, the heating distribution on either side of the higher maxima is produced as shown in Figure 3.21b.

Cross flow planes of the uncoupled CFD–DSMC simulation are presented in Figure 3.23a, b, and c at x locations of 0.100, 0.125, and 0.150 m, respectively. Each figure is arranged with cross flow streamlines above the plate superimposed on normalized number density contours at each plane. Although the molecular simulation was for one-half of the plate to the symmetry plane, shown on the figure is a full plate width view with a mirror of the half-plate solution, which provides a better perspective of the cross flow features. Note that the region occupied by the plate is masked white to show its position in the simulation domain. Additionally, shown masked in white in Figure 3.23b is the jet non-interacting plume surface.

Shown in Figure 3.23a, the $x = 0.100$ m plane, are cross flow streamlines, which indicate an upward and sideward flow direction. The flow is directed up and to both sides because of the forward vortex. Note that the forward vortex center is located downstream of the $x = 0.100$ m plane and has an upward velocity component on the symmetry plane at this x location (See Figure 3.22b.).

Number density contours also show the effect of the forward vortex. A higher density region is shown in Figure 3.23a centered at $y = 0$ m and about 0.015 m above the plate. This region has a higher density than the surrounding region because it is located where the forward vortex is elongated from the compression of the free stream flow turning upward over the separation zone (Again, see Figure 3.22b at the $x = 0.100$ m location.). Also, on both the sides of this high density region, the number density decreases showing the three-dimensional nature of the separation wrapping about the

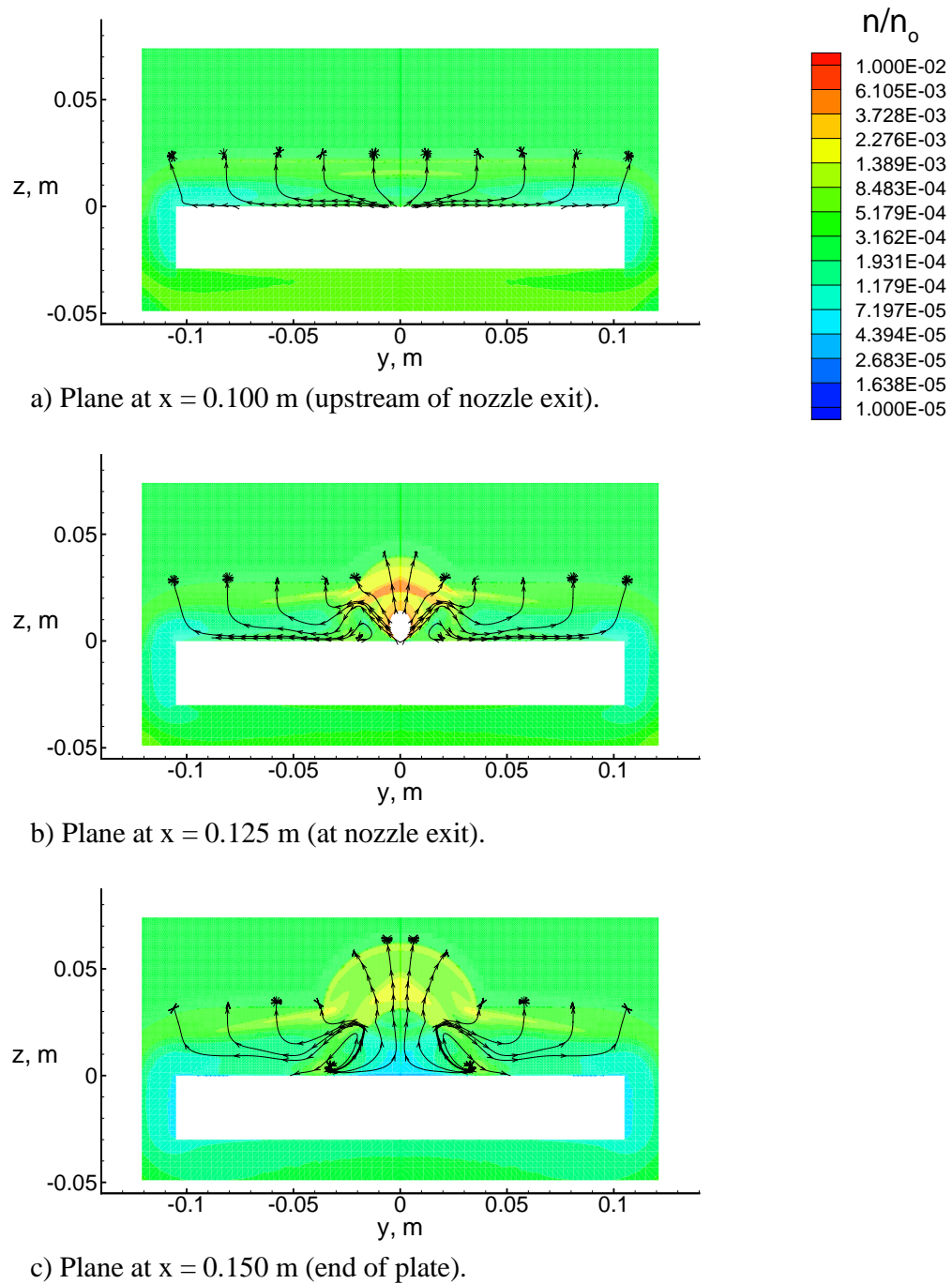


Fig. 3.23. Jet interaction flow field at various cross flow planes.

jet. Finally, note the streamlines shown in Figure 3.23a end above the higher density contoured region at $z \approx 0.025\text{m}$ because the velocity components in the y and z directions become zero. The end points of the cross flow streamlines occur in the undisturbed free stream and therefore indicate the extent of the viscous layer above the plate.

Shown in Figure 3.23b is the cross flow plane at $x = 0.125\text{ m}$. Flow streamlines in the figure and the simulated oil flow pattern at the plate surface (See Figure 3.22a.) indicate that the jet induced vortex structure has moved the free stream gas away from the wall on either side of the symmetry plane at this cross section location. The jet induced vortex (just upstream of the jet nozzle exit in Figure 3.22) has turned about the jet and emerges from this cross flow plane as the vortex structure shown in Figure 3.23b.

Number density contours at the $x = 0.125\text{ m}$ plane are also shown in Figure 3.23b. A complex flow interaction region is shown above the jet plume surface and extends about 0.04 m above the plate surface. Jet flow initially expands outward, as evidenced by the decreasing number density near the plume surface, until being compressed by the interaction with the free stream. The interaction causes the number density to increase as the jet and free stream flow are compressed and turned from the original flow direction.

The final cross flow plane is shown in Figure 3.23c at the plate trailing edge ($x = 0.150\text{ m}$). Flow streamlines in the figure show that the vortices at the previous cross flow plane (see Figure 3.23b) persist to the plate trailing edge; however, the vortices become elongated and less organized rising further above the flat plate surface because of mixing as angular momentum is transferred to the surrounding fluid. Also, flow at the symmetry plane is directed upward away from the plane surface as the upward jet injection still affects the flow at the trailing edge cross flow plane.

The number density contours at the $x = 0.150$ m location, given in Figure 3.23c, show that the jet interaction region has become larger than at the previous planar location and extends about 0.06 m above the plate surface. Also, a high density lobe is shown near the surface at $y \approx \pm 0.04$ m, which corresponds to the vortex attachment line location at the plate trailing edge shown in Figure 3.22a. The vortex structure is larger and more diffused than at the $x = 0.125$ m cross flow plane (See Figure 3.23b.). Note that the simulation domain extended far enough from the upper plate surface to capture the entire density gradient field of the interaction at this plane.

3.4.5 Effect of DSMC Grid on Flow and Surface Properties

The molecular simulation on the third adaptation grid for the transitional–rarefied jet interaction presented in Section 3.4.3 required extensive computational resources, which were close to the capacity of the HPCC SGI/Cray T3E, one of the largest multi-processor computers available. A DSMC solution on a finer adaptive grid with more cells for this jet interaction condition is not possible at this time because it would exceed the existing computational resources. However, the current simulation on the fine grid did produce detailed flow features of the transitional–rarefied free stream interacting with a continuum jet, the quality of which can be assessed by comparing the fine grid results with those from the other more coarse grids, that is, from the simulations performed on the uniform, first adapted, and second adapted grids. These flow field results were presented previously in Section 3.4.3.

For this grid convergence analysis, several significant features of the flow field are identified and tracked for each grid solution. First, the locations on the symmetry plane

of the upstream edge of the compression waves generated by both the flat plate sharp leading edge and the jet interaction, at $x = 0.02$ m and 0.03 m, respectively, above the plate surface are obtained as a function of the grid adaptation. These two locations in the flow field are labeled in Figure 3.24 as point 1 and point 2. Next, the surface pressure and heating and location of the forward separation and vortex attachment points on the symmetry plane are presented as a function of grid adaptation. These locations are given by the letters S and A, respectively, in Figure 3.24. By comparing and analyzing flow features such as these for simulations with various grid spacing, an assessment of the quality of the final adapted grid simulation can be performed.

To locate the leading edge of a compression wave as its position varied with grid adaptation cycle, flow variables along horizontal line cuts at the appropriate height above the flat plate were extracted from the flow field and examined to reveal the position where the local number density increased to a value ten percent above that of the free stream value. This ten percent position provides a consistent measure of the flow field compression wave location at points 1 and 2 where local flow properties are obtained for the analysis.

Point 1, shown in Figure 3.24, is the leading edge of the flat plate compression wave 0.02 m above the plate surface. The normalized location, x/L of this flow field feature is presented as a function of the local ratio of cell spacing (ds) to mean free path (λ) in Figure 3.25a. The ratio, ds/λ , decreases by about an order of magnitude from its value for the initial uniform grid solution to its value for the third grid adaptation. Also, it is well documented (See Moss et al. [53].) that DSMC solutions asymptotically approach grid convergence as this ratio falls below unity. Therefore, an exponential curve

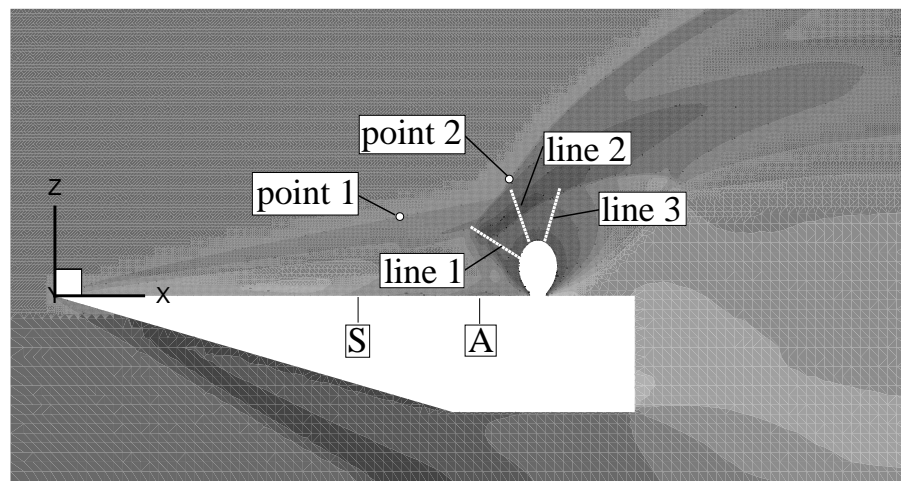
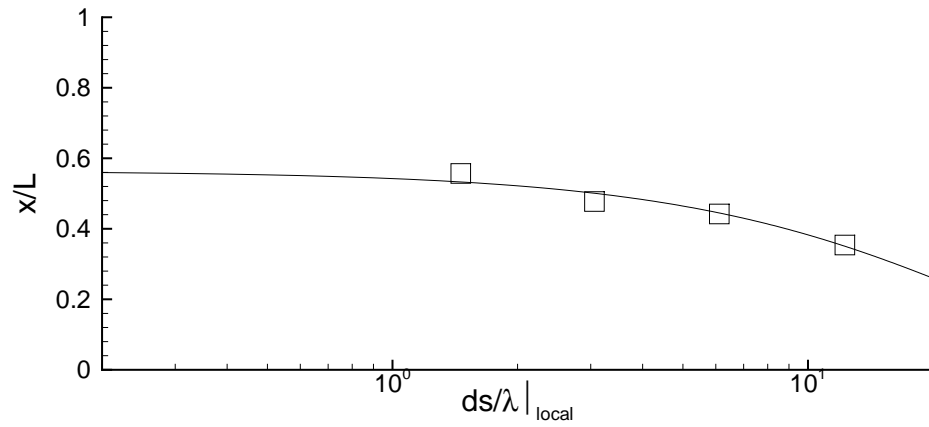
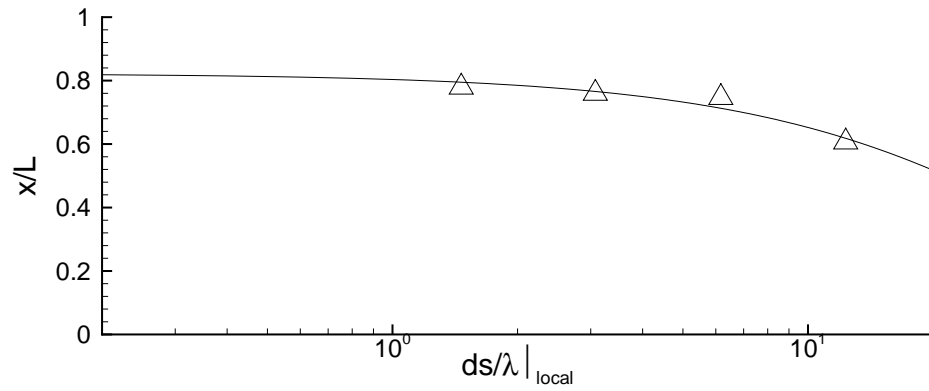


Fig. 3.24. Symmetry plane number density contours from the $P = 0.01$ uncoupled CFD-DSMC solution showing key locations for comparisons.



a) Flat plate leading edge compression wave, point 1.



b) Jet interaction compression wave, point 2.

Fig. 3.25. Effect of DSMC grid on location of compression wave flow field features.

has been fit through the discrete points given by the square symbols, which represent locations taken from the uniform, first, second, and third adapted grid simulations. For the curve fit, a boundary condition was imposed that the slope of the curve approach zero in the limit as $ds/\lambda|_{\text{local}} \rightarrow 0$. However, the slope requirement of the curve fit may be too restrictive as an end boundary condition because Moss et al. [53] have shown that DSMC grid independence is achieved for $ds/\lambda|_{\text{local}} \leq 0.35$.

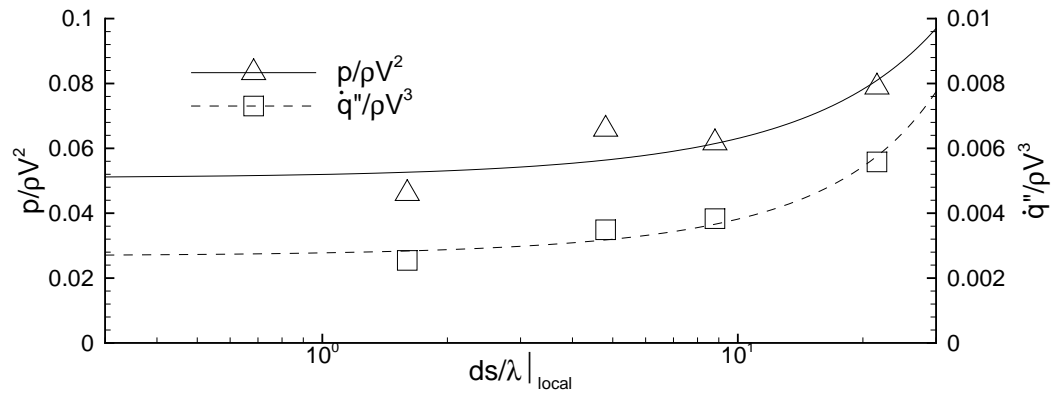
Although the discrete points presented in Figure 3.25a show some scatter about the curve, the trend of the curve illustrates that with coarse cell spacing, the flat plate compression wave leading edge is further upstream than with fine cell spacing. At the zero cell size limit, the curve fit shows the location of the compression wave leading edge at $x/L \approx 0.55m$, close to the value obtained with the third adapted grid simulation. A similar trend is shown in Figure 3.25b for the leading edge location of the jet interaction compression wave, that is, with decreasing cell spacing, the leading edge of the compression wave initially moves downstream and then its location becomes stationary as cell size is further decreased. Based on these observations, local cell spacing of the third adapted grid ($ds/\lambda|_{\text{local}} \approx 1.5$) may be adequate to locate the position of compression waves in the flow field.

Next, along the flat plate center line, surface pressure and heating at the flow separation and attachment points and the extent of flow separation associated with the jet interaction are analyzed to determine the effect of cell spacing on the forward separation region. The interacting jet causes a forward separation region consisting of two counter-rotating vortices as discussed previously in Section 3.4.4 and shown by the simulated oil flow and stream lines in Figure 3.22. The simulation for each of the

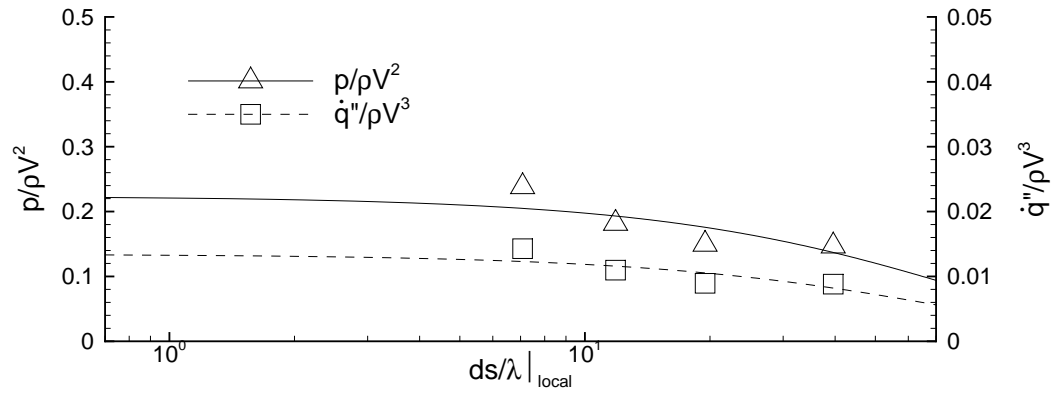
four grids showed these same general flow features; however, the flow separation and attachment point surface pressure and heating and the location of the separation and attachment change with cell spacing. By presenting the variation of these surface values as a function of the ratio of cell size to mean free path (ds/λ) for the four grids, an assessment of the grid quality in the flow separation region can be made.

Figure 3.26 shows surface property variation at the flow separation and attachment points with $ds/\lambda|_{\text{local}}$. At the flow separation point, pressure and heating decrease as local cell spacing is refined (See Figure 3.26a.). Note that, similar to Figure 3.25, an exponential curve is fit though the pressure and heating results to aid with determining the trend for local cell spacing finer than $ds/\lambda|_{\text{local}} \approx 1.5$ from the third adapted grid. Normalized pressure tends to a value of 0.046 and normalized heating tends to 0.0024, which are close to the present fine grid result.

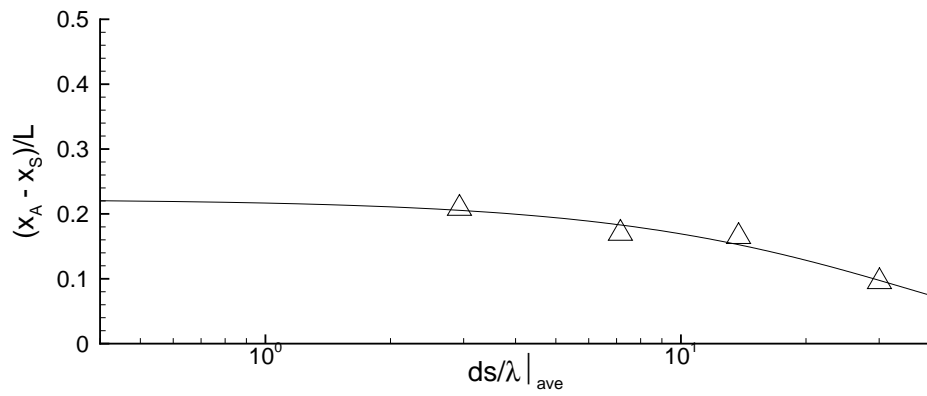
Flow attachment pressure and heating at the center line as a function of cell spacing is shown in Figure 3.26b. Flow from both counter-rotating vortices impinges on the plate at the attachment point and causes a local high density region (See, for example, the number density contours in Figure 3.20 near the upper plate surface at $x = 0.11m$, which is the attachment point.). Because of the high density region in the vicinity of the attachment point, the finest local cell spacing for the third adapted grid in this region is $ds/\lambda|_{\text{local}} \approx 7$. As shown in Figure 3.26b, the pressure and heating increase with decreasing cell spacing as the flow impingement region is better resolved. The curve fit shows normalized pressure tends to a value of 0.22 and normalized heating tends to about 0.013 as the cell spacing goes to zero. Although scatter exists between



a) Flow separation, S.



b) Flow attachment, A.



c) Extent of separation.

Fig. 3.26. Effect of DSMC grid on center line surface properties.

the data and curve fit, the curve fit shown in Figure 3.26b does provide a reasonable estimate of the attachment point pressure and heating in the grid-converged limit.

The final comparison presented to determine the effect of the DSMC grid spacing in the forward separation region is the normalized distance between the flow separation and attachment points, $(x_A - x_S)/L$, as a function of the average normalized cell spacing, $ds/\lambda|_{ave}$, which is shown in Figure 3.26c. Although the extent of forward separation is usually defined for this type of flow as the distance from the flow separation point to the jet, presently it is represented as $(x_A - x_S)/L$ to include the influence of the flow attachment location in the definition.

Figure 3.26c shows the results for simulations performed on the four grids. Note that for the finest cell resolution (the third adapted grid), the average cell spacing relative to mean free path is approximately three. However, less scatter exists between the exponential curve fit and the individual points for this comparison than for the previous two comparisons of Figures 3.26a and b with pressure and heating. Probably because the extent of separation is a quantity associated with larger scale flow phenomena than local pressure and heating at the separation and attachment points, it is affected less by cell spacing, hence, better agreement of the individual points with the curve fit. The curve shows that as cell spacing decreases, the extent of separation indicated by $(x_A - x_S)/L$ tends to a value of 0.22, which is close to the result from the finest grid simulation.

Generally, a molecular simulation with cell resolution less than the local mean free path is desired. However, for the present jet interaction simulation, this desired cell resolution was not achievable. Nonetheless, a comparison of several key flow field and surface features from the molecular simulations performed on the four grids with various

cell resolutions has shown that application of the DSMC technique to the third adapted grid provides a reasonable description of the transitional–rarefied free stream interacting with a continuum jet.

3.4.6 Effect of Bird Breakdown Parameter

In this section, the effect of the Bird breakdown parameter value on the DSMC portion of the uncoupled solution is investigated. Three issues will be explored: (1) Is the uncoupled $P = 0.01$ surface a sufficient boundary between the CFD and DSMC solutions so that there is no need to iterate between the two domains; (2) Is the correlation given in Figure 3.10 credible in determining the uncoupling surface for the present transitional–rarefied jet interaction; (3) What is the consequence of using an uncoupling surface between the CFD and DSMC portions of the flow field with a value greater than that shown by the correlation in Figure 3.10?

To address the first issue, a comparison between the CFD expanding jet solution presented in Section 3.4.1 and the DSMC third adapted grid solution presented in Section 3.4.3 is made near the $P = 0.01$ surface. A $P = 0.011$ breakdown parameter value was used for the comparison instead of $P = 0.01$. Flow properties at $P = 0.01$ cannot be accurately extracted from the DSMC flow solution because of cell clipping effects at the triangulated jet plume surface. Number density, pressure, and velocity were obtained at three locations: on the symmetry plane forward of the jet exit, on the cross flow plane at the jet exit ($x = 0.125m$), and on the symmetry plane aft of the jet exit. These results are presented in Figures 3.27, 3.28, and 3.29, respectively. The flow quantities number density, pressure, and velocity were chosen for the comparison because they are

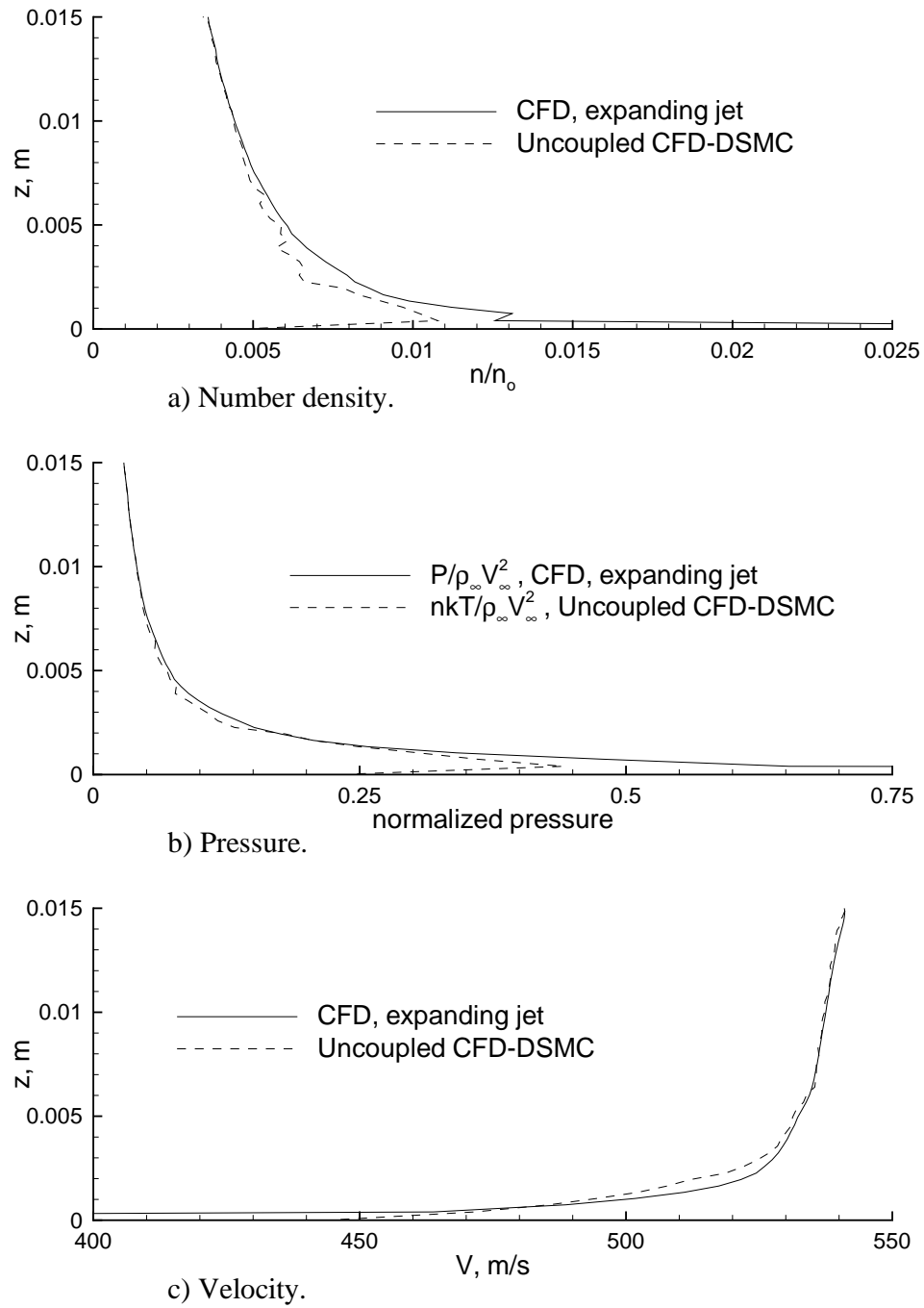


Fig. 3.27. Comparison of Ar jet flow properties forward of the jet exit on the symmetry plane at $P = 0.011$.

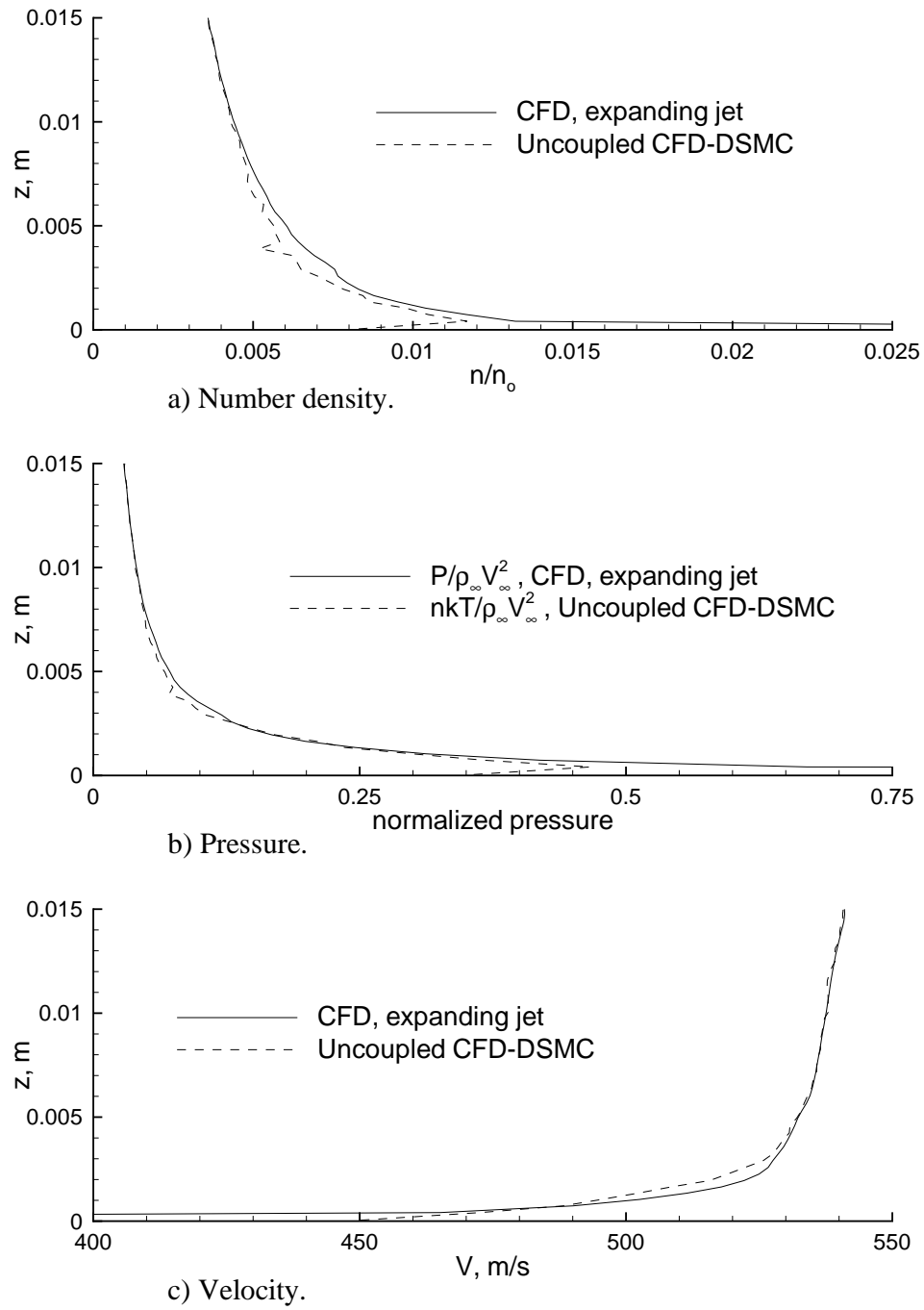


Fig. 3.28. Comparison of Ar jet flow properties on the $x = 0.125m$ cross flow plane at $P = 0.011$.

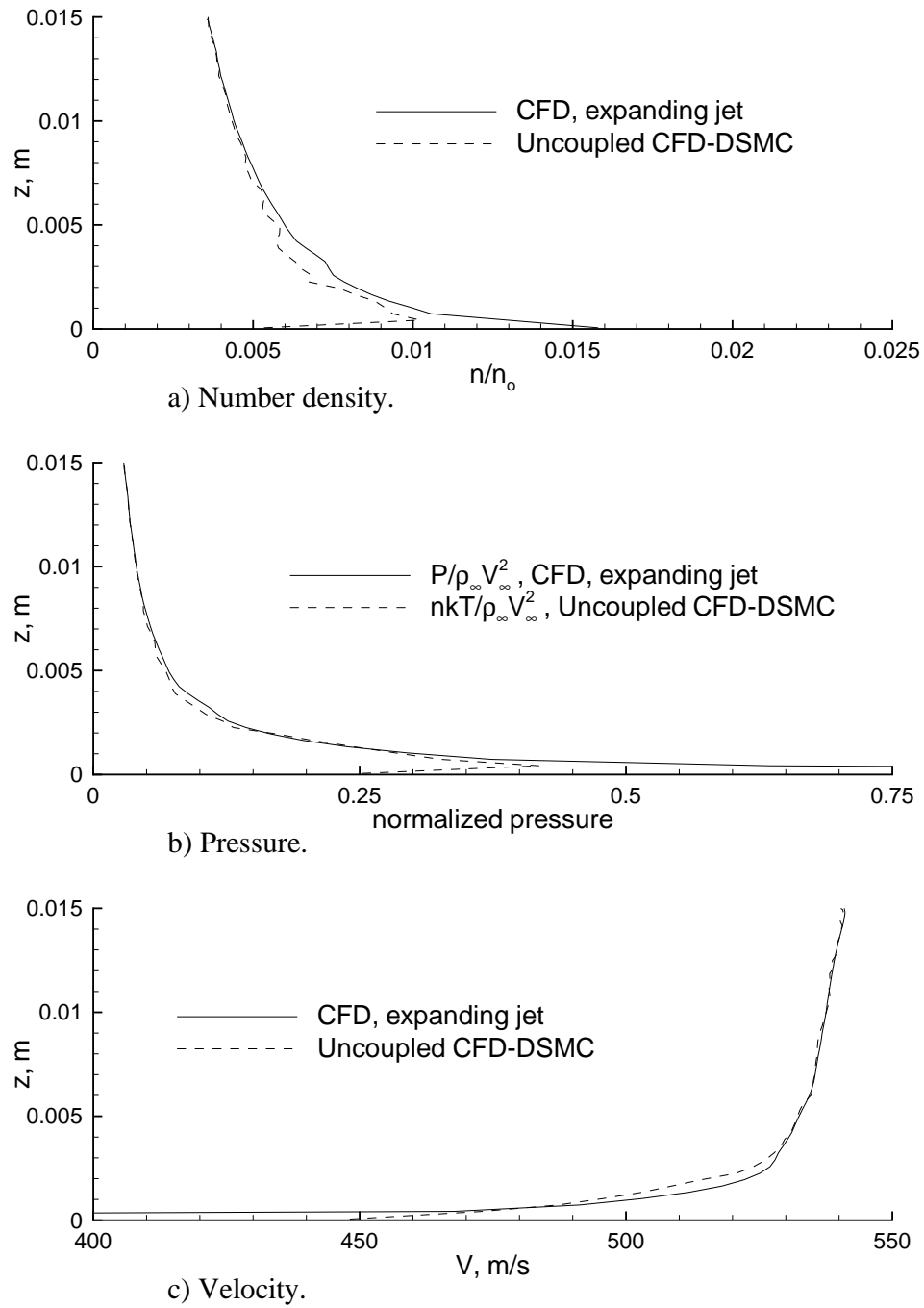


Fig. 3.29. Comparison of Ar jet flow properties aft of the jet exit on the symmetry plane at $P = 0.011$.

representative of those that would be employed as coupling boundary conditions if an iterative technique were required.

At the three locations, a comparison of normalized number density between the expanding jet CFD and uncoupled DSMC solutions shows a difference from the wall to about 0.005 m above the wall (See Figures 3.27a, 3.28a, and 3.29a.). Number density is consistently less in this region for the DSMC result; the difference being greatest at the wall, which may be caused by unresolved DSMC wall cell spacing at the inflow plume boundary, statistical scatter of the DSMC, nozzle edge effects of the CFD expanding jet solution, or a combination of all three. Generally, however, differences between the two number density results are not large except near the wall ($z \leq 0.0005$), and elsewhere away from the wall, the comparison is good.

Normalized pressure at the $P = 0.011$ breakdown parameter value for the forward symmetry plane, cross flow plane, and aft symmetry plane locations are given in Figures 3.27b, 3.28b, and 3.29b, respectively. For the CFD expanding jet, pressure was obtained directly from the solution, and for the DSMC, it is calculated as nkT , the equilibrium pressure. Similar to the number density comparisons discussed previously, there is a difference in pressure near the wall (to $z \approx 0.001m$), however, away from the near wall region, the pressure is in reasonable agreement.

The next comparison between the CFD expanding jet and DSMC interacting jet solutions is with velocity. Figures 3.27c, 3.28c, and 3.29c, show the velocity at the forward symmetry plane, cross flow plane, and aft symmetry plane locations, respectively. Generally, a good agreement is shown between the two solutions at the $P = 0.011$ location

of the comparisons. There is a difference, however, near the wall, which was also observed with the number density and pressure comparisons.

As discussed above, the near wall differences in flow properties may be caused by inadequate DSMC cell spacing at the wall near the $P = 0.01$ inflow boundary surface, which is particularly important in the rapidly expanding flow about the nozzle exit corner of the free expanding jet. Regardless of these near wall differences, the two solutions match reasonably well, especially away from the wall where the interacting flow compression would be present. Therefore, based on the comparisons of results given in Figures 3.27, 3.28, and 3.29, an uncoupling of the CFD and DSMC solution methods with no iterative cycle between the two is justified. This conclusion is further supported by the results given in the following paragraphs.

The credibility of the correlation given in Figure 3.10 is considered subsequently by comparing results from the expanding jet CFD solution and interacting jet DSMC solution along three line cuts on the symmetry plane from the $P = 0.01$ surface outward into the flow field. These line cut locations are shown in Figure 3.24 by the white dashed lines labeled line 1, line 2, and line 3. Lines 1 and 2 traverses upward and forward from the $P = 0.01$ surface through the jet interaction compression upstream of the nozzle exit, and line 3 passes aft from $P = 0.01$ directed upward and downstream of the nozzle exit. The flow quantities compared along the three lines are number density, pressure, and velocity as a function of increasing Bird breakdown parameter value, P . Given in Figures 3.30, 3.31, and 3.32 are the variables extracted on lines 1, 2, and 3, respectively, from the expanding jet CFD and interacting jet DSMC flow fields. By comparing the variation of these quantities with the breakdown parameter value in the direction of

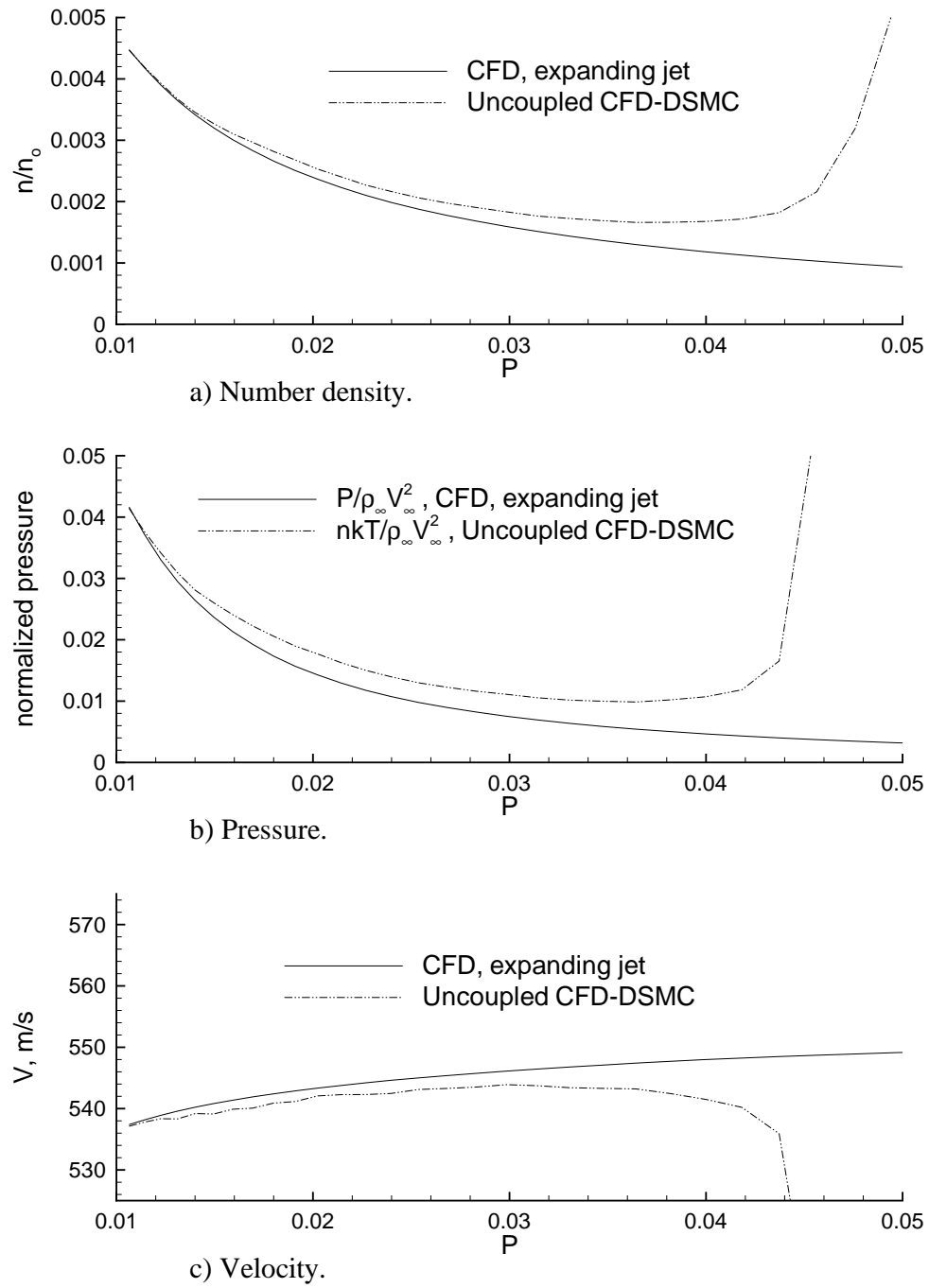


Fig. 3.30. Flow variable change along line 1 as a function of breakdown parameter value.

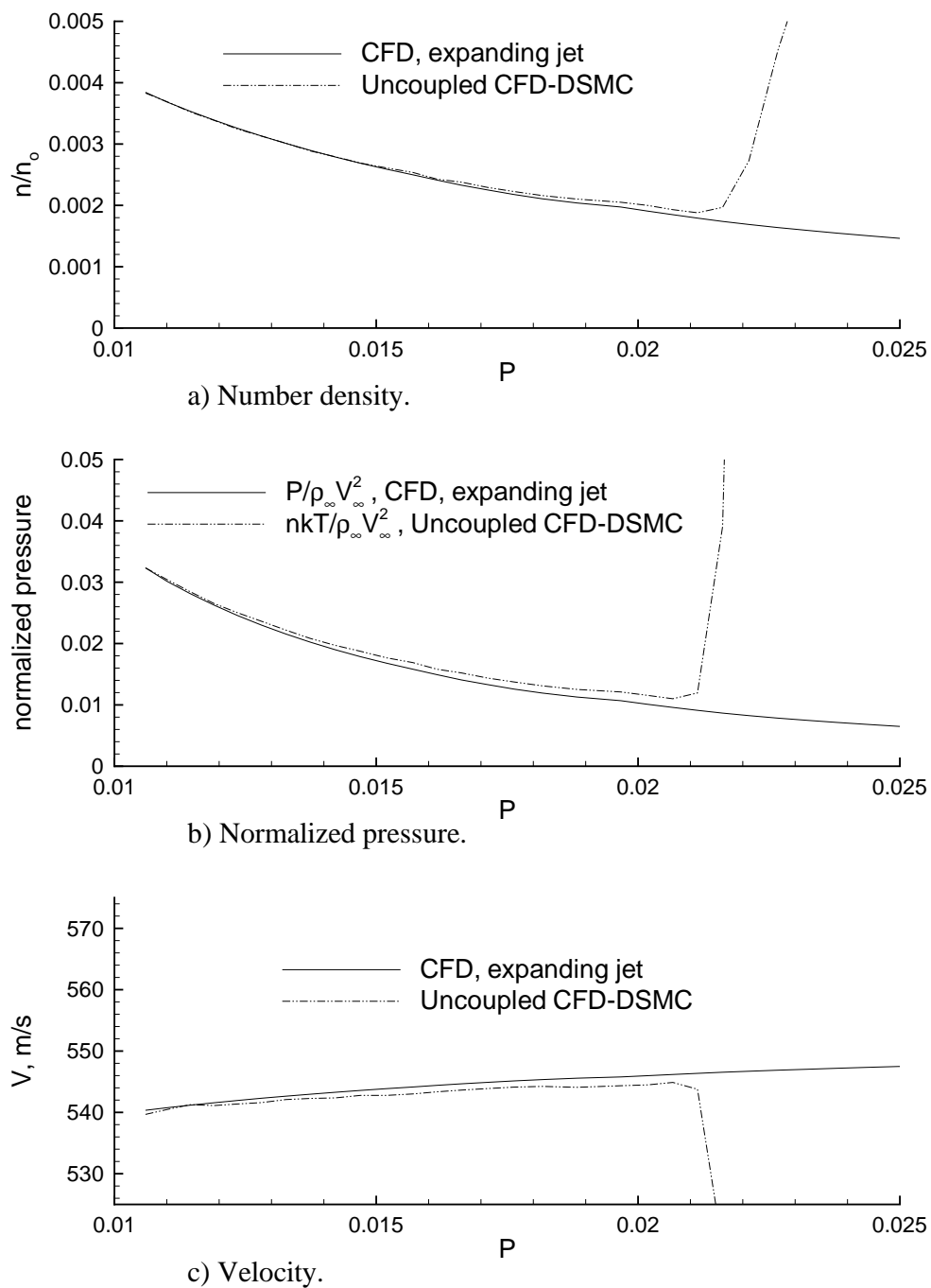


Fig. 3.31. Flow variable change along line 2 as a function of breakdown parameter value.

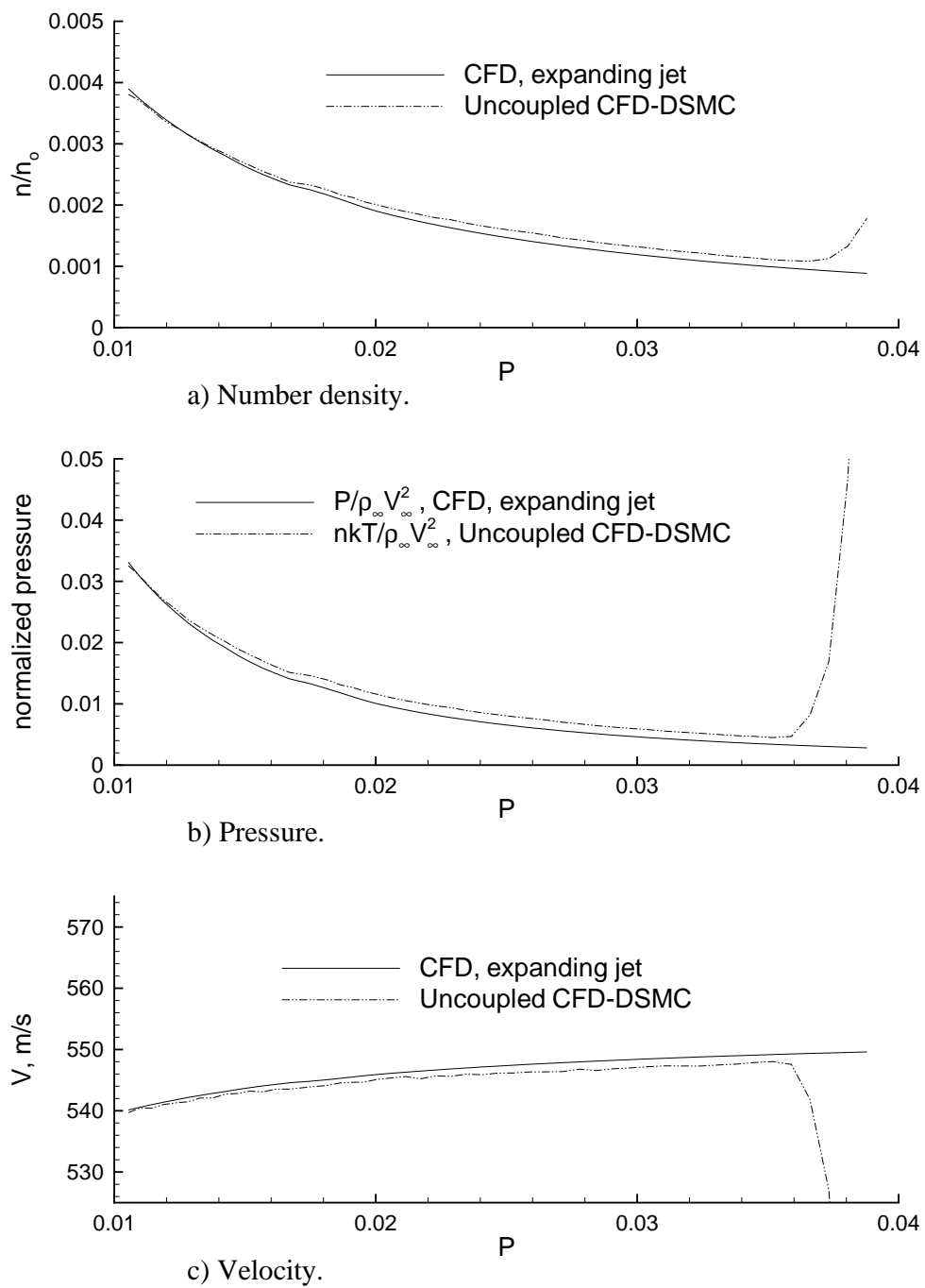


Fig. 3.32. Flow variable change along line 3 as a function of breakdown parameter value.

expanding flow (increasing P), definite conclusions may be revealed about using the results presented in Figure 3.10 to determine a value of P at which to uncouple the CFD and DSMC portions of the interacting flow field.

The variation of flow properties along line 1 (see Figure 3.24), which is given in Figure 3.30, shows that the number density, pressure, and velocity for the freely expanding jet (CFD) and interacting jet (DSMC) approach the same values as $P \rightarrow 0.01$. With increasing P , results from the two solutions diverge, and at $P = 0.02$, the flow variables are significantly different. Note that the figure shows for $P > 0.04$ there is a large increase in number density and pressure and a similar decrease in velocity for the uncoupled CFD-DSMC solution because at this location, the jet-free stream flow interaction is significant. Along line 1, $P = 0.04$ occurs a distance of about 0.0075 m from the $P = 0.01$ surface.

Shown in Figure 3.31 are the number density, pressure, and velocity comparisons along line 2. Note that line 2 is above line 1 and also extends into the forward jet interaction region. At $P = 0.01$, the flow variables presented in the figure from the CFD of the expanding jet and DSMC of the interacting jet have the same values. Also, the number density from the CFD and DSMC solutions are the same for $P < 0.015$ and only diverge slightly until the breakdown parameter is greater than 0.021. The pressure and velocity follow the same trend with increasing P . Moreover, for $P > 0.021$, the DSMC result shows density and pressure increases greatly with a corresponding decrease in velocity, and demonstrates that the initially expanding jet begins to be influenced by the interacting flow region at $P = 0.021$, which is about 0.006 m from the $P = 0.01$ surface.

Next, a comparison of the flow variables as a function of breakdown parameter value along line 3 is given in Figure 3.32. A trend similar to that of line 2 is observed, except that the P value where deviation between the freely expanding and interacting jet results is different. For line 3, the two solutions diverge slowly until $P = 0.036$, where, for increasing P , density and pressure increase rapidly, and velocity likewise decreases ($P = 0.036$ occurs 0.013 m from the $P = 0.01$ surface.). The sudden change in flow properties in the DSMC solution is located where the jet flow confronts the interacting portion of the flow field at that location.

Although only three line cuts have been presented, they clearly show that as P is increased, number density, pressure, and velocity differ between the freely expanding jet CFD and the interacting jet DSMC flow field solutions. Conversely, the two solutions approach each other as $P \rightarrow 0.01$. The analysis of properties along line 1 shows the difference becomes significant for breakdown parameter values greater than $P \approx 0.015$. For lines 2 and 3, the difference in properties was small until the flow encountered the edge of the interacting flow region. Therefore, it is concluded that the curve fit correlation given in Figure 3.10 can be employed as an accurate guide to define the breakdown parameter value at which to uncouple the CFD and DSMC portions of the jet interaction flow for the present flow conditions.

Subsequently, the third issue listed at the beginning of this section is explored. A comparison of two flat plate jet interaction simulations is provided to assess the consequence of defining the jet non-interacting plume surface with a value of the breakdown parameter larger than that suggested in Figure 3.10. In Section 3.4.4, the uncoupled CFD-DSMC simulation of a nitrogen free stream interacting with an argon jet defined

by a value of the non-interacting plume breakdown parameter of $P = 0.01$ was presented. For the present comparison, the same interaction is simulated except that the jet plume is defined by a $P = 0.02$ breakdown parameter value.

As with the $P = 0.01$ case, the present simulation required grid adaptation to produce the final molecular simulation. The grid adaptation procedure was identical to the one used for the $P = 0.01$ simulation. The extent of the domain, number of adaptation cycles, level II gridding for each cycle, and number of sampling time steps for each of the solution cycles were duplicated so that the final simulation would not be biased by the grid adaptation. The final adapted grid produced 134.1 million steady state molecules for the 13.25 million active cells. Note that the simulation with $P = 0.01$ required 134.5 million molecules, about 400 thousand molecules greater than the $P = 0.02$ simulation.

Flow field comparisons are made using number density contours at the two planar locations, which bisect the jet nozzle exit location. Figures 3.33a and b show the symmetry plane contours for the $P = 0.01$ and $P = 0.02$ cases, respectively, and Figures 3.34a and b show the cross flow plane number density contours at $x = 0.125$ m location for the same cases.

The flow field comparison shows that some differences exist between the two simulations. The most obvious difference is that the $P = 0.02$ solution has larger jet plume, but more subtle differences are present. In the interaction zone, for example, the region of maximum compression (highest number density) just forward of the jet plume ($x \approx 0.12$ m, $z \approx 0.02$ m) for the $P = 0.01$ case is larger than for the $P = 0.02$ case (see Figure 3.33). Also, the high density region abuts the surface of the $P = 0.02$

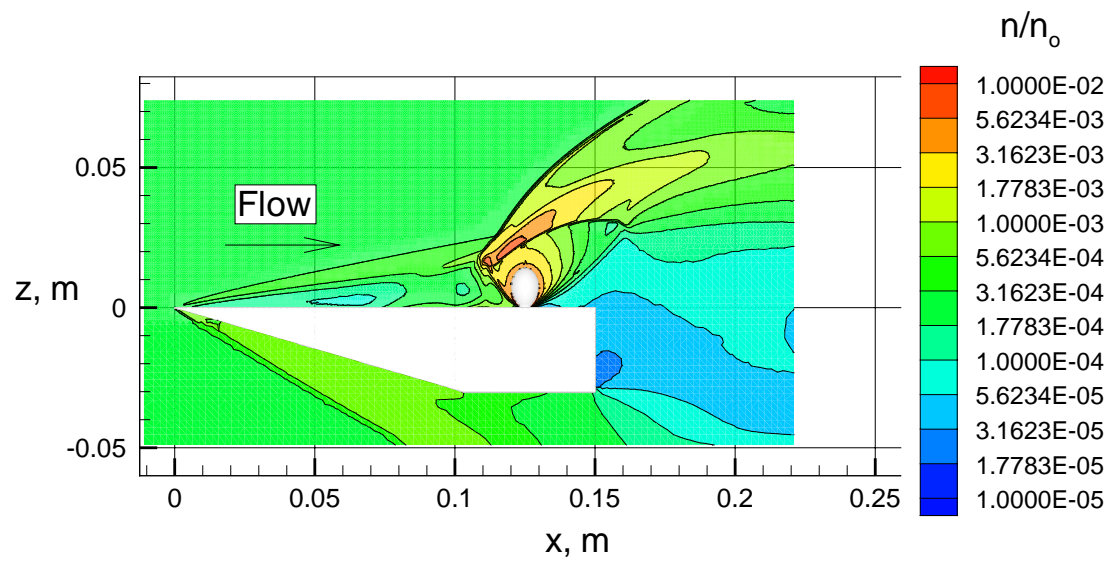
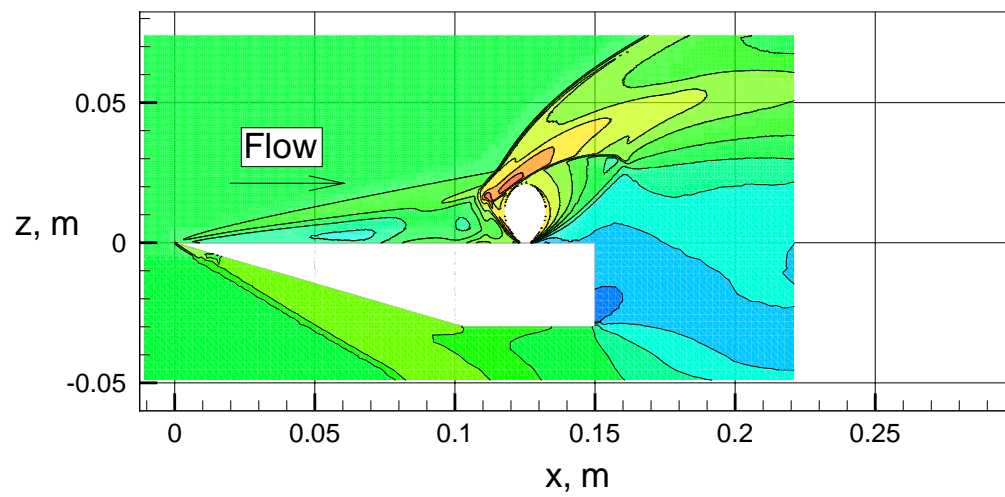
a) $P = 0.01$.b) $P = 0.02$.

Fig. 3.33. Number density contours on the symmetry plane for various breakdown parameters.

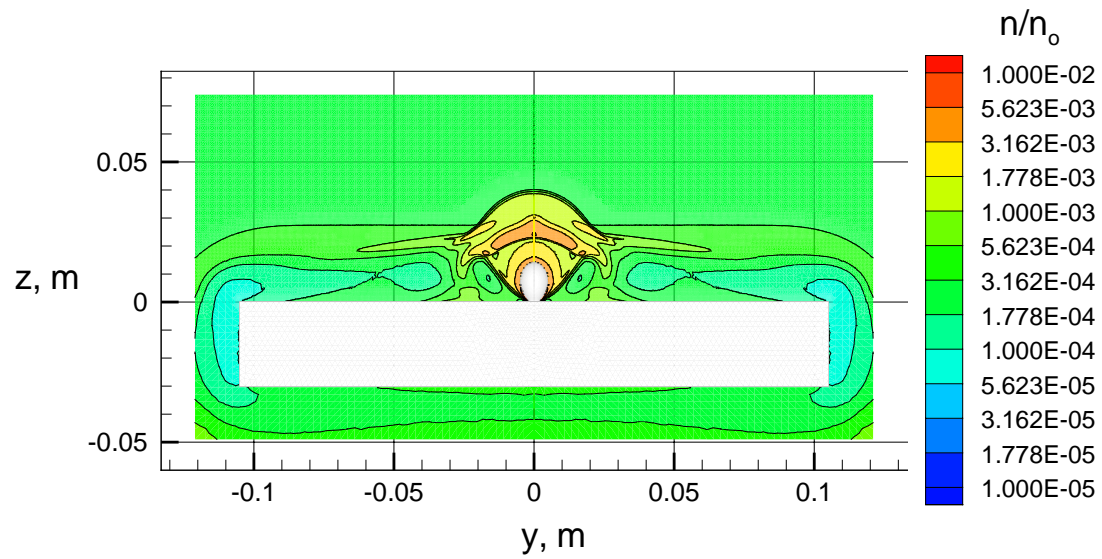
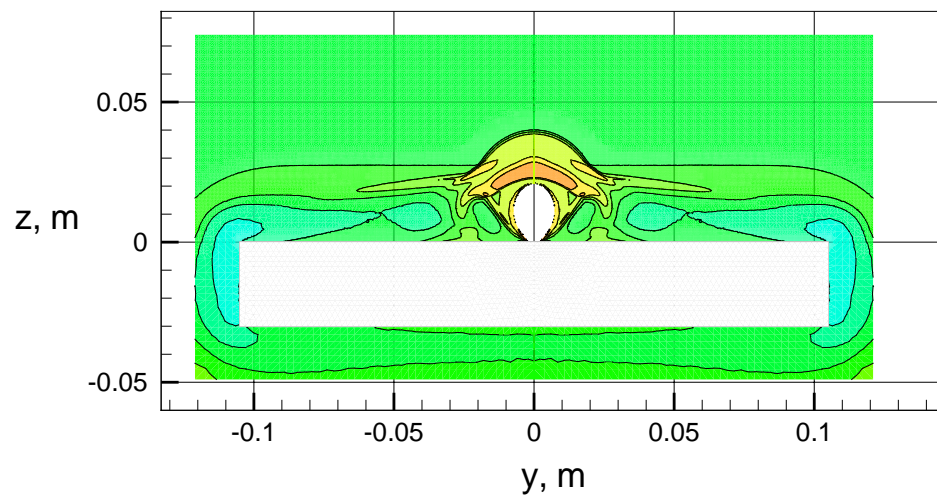
a) $P = 0.01$.b) $P = 0.02$.

Fig. 3.34. Number density contours at $x = 0.125$ m cross flow plane for various breakdown parameters.

plume. It is important to note that the boundary condition assigned to the jet plume is an outgassing surface. The outgassing surface allows a molecule moving toward the surface to pass through and be deleted from further considerations rather than a molecule striking the surface and rebounding back into simulation domain as with a solid surface boundary. This boundary type is applicable for the uncoupled technique where few molecules move into the plume region; however, as for the $P = 0.02$ plume, which abuts a high density compression, the size of the compression region may be reduced because molecules, which should affect the flow inside the plume breakdown surface and contribute to the interaction compression, are deleted when they cross the plume surface.

Slight differences are also shown when comparing the number density cross flow planes of the two cases (see Figure 3.34). Near the location $y \approx \pm 0.015$ m and $z \approx 0.01$ m, the $P = 0.01$ case has a region of lower number density than the $P = 0.02$ case. The difference may be caused by more complete development of the vortical flow about the jet plume in this region for the $P = 0.01$ plume than for the larger plume of $P = 0.02$, which extends closer to the vortical flow region (Also see Figure 3.20.).

Except for the differences discussed previously, both of the flow fields shown in Figures 3.33 and 3.34 exhibit the same gross features. Jet compression forward of the plume and expansion to the aft of the plume are nearly identical. For the present flat plate jet interaction, flow field differences do not generally affect the properties on the plate surface because the interacting flow is swept above and downstream of the plate. There are, however, several regions on the plate surface near the nozzle exit that differ. To show the differences near the nozzle exit caused by increasing the breakdown parameter value, a comparison between the surface pressure contours of the $P = 0.01$

and $P = 0.02$ cases is presented in Figures 3.35a and b, respectively. Shown in the figure is the starboard surface of the flat plate for each case. Note that $y = 0$ m is the plate symmetry line and the nozzle exit is located on the symmetry line at $x = 0.125$ m.

Similar to the flow field comparisons presented above, the surface pressure contours shown in Figure 3.35a and b are generally in good agreement. However, a difference is apparent at the near nozzle exit region. Shown in Figure 3.35b is a higher pressure compression adjacent to the nozzle exit and a lower pressure wake region downstream of the nozzle exit. These details are further revealed in Figure 3.36, a close-up view of the surface pressure and simulated oil flow in the immediate vicinity of the nozzle exit, which is shown as a white semi-circle centered at $(x = 0.125$ m, $y = 0.000$ m). Simulated oil flow streaks have also been included in the figure to indicate the effect of the continuum plume size on the local surface shear stress.

The figure shows surface pressure for the $P = 0.01$ case decreases monotonically around the circumference of the nozzle exit from forward to aft. The pressure around the nozzle exit of the $P = 0.02$ case initially decreases, sharply increases, then decreases. The high pressure region is located at $x \approx 0.124$ m and $y \approx 0.002$ m as shown in Figure 3.36b. Additionally, the oil flow lines in the figure are bulged away from the high pressure region for the $P = 0.02$ case when compared to the $P = 0.01$ case (Compare Figure 3.36b with Figure 3.36a.).

The cause of the high pressure region near the jet plume base is related to the anomaly about the base region shown earlier in Figure 3.9 for the $P = 0.02$ case. To examine the anomaly in greater detail, the CFD solution of the nozzle base region (See Section 3.3.1.) was investigated with the aid of the EnSight program, which showed the

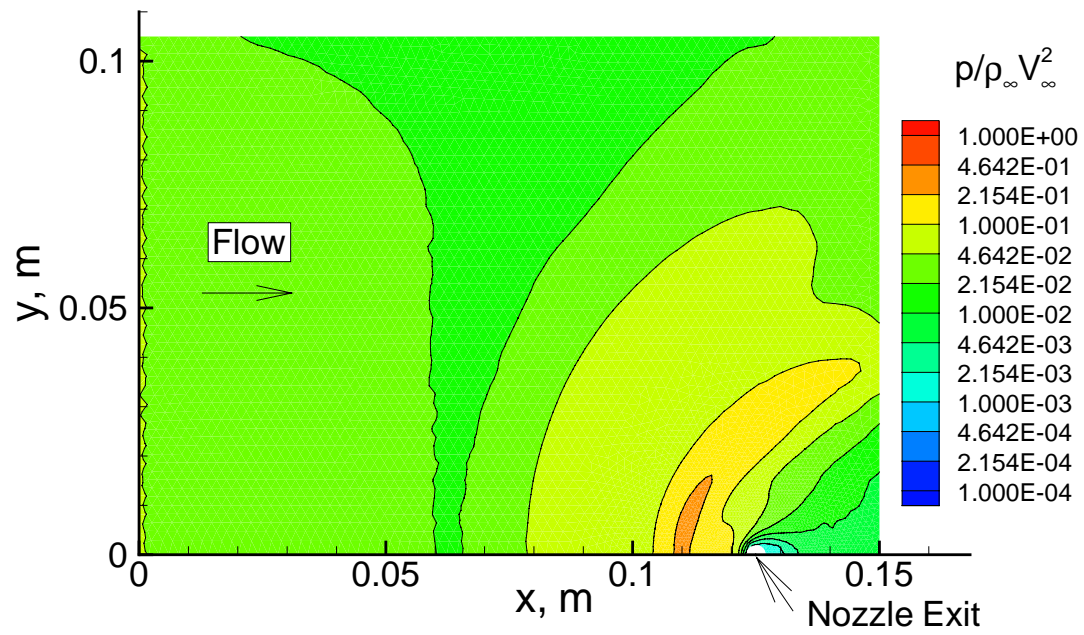
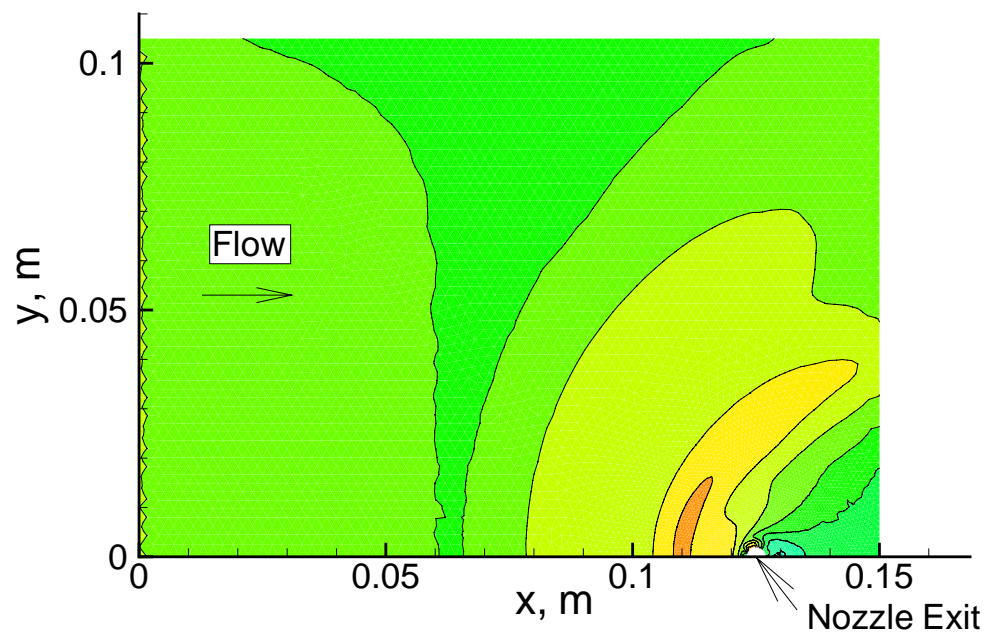
a) $P = 0.01$.b) $P = 0.02$.

Fig. 3.35. Surface pressure comparisons to show effect of breakdown parameter.

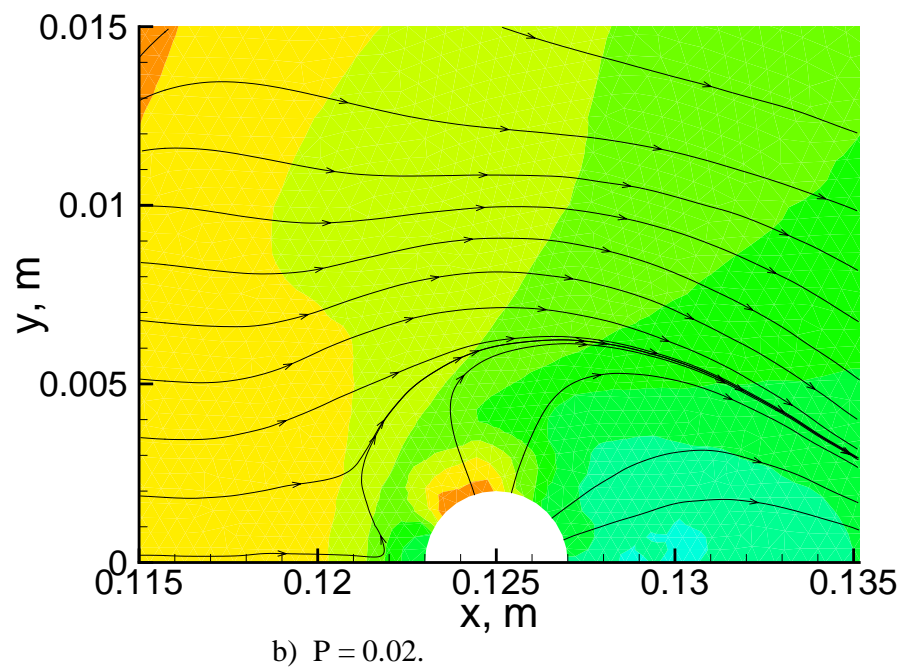
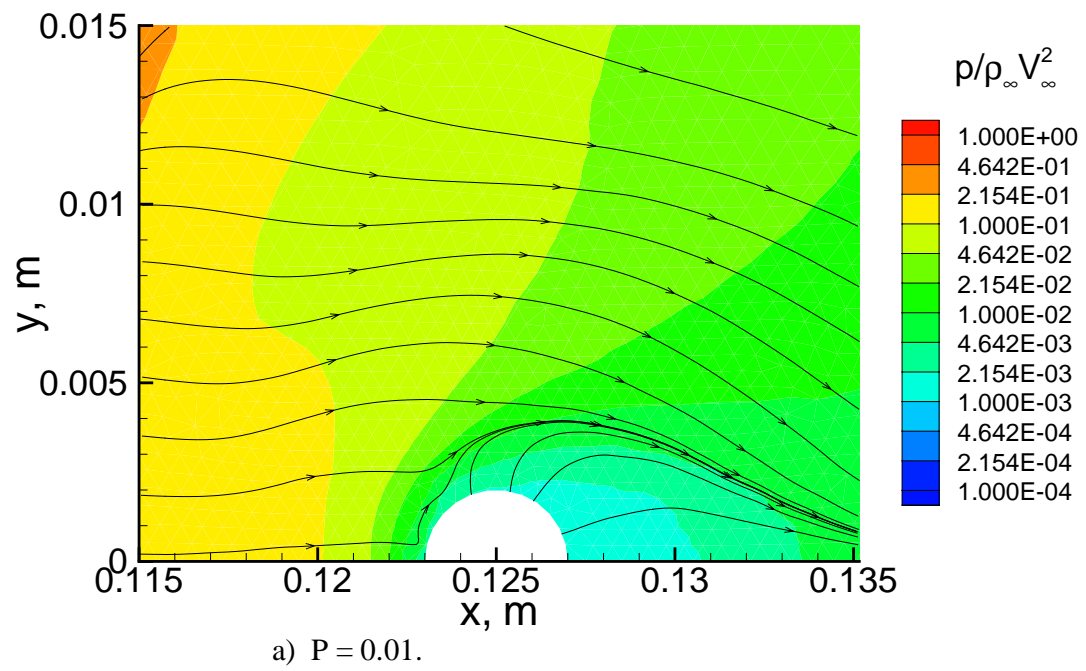


Fig. 3.36. Detailed surface pressure and simulated oil flow comparisons at the nozzle exit location.

breakdown surface for a parameter value of $P = 0.02$ case folded over to the plate surface outside of the nozzle exit parameter. This result indicates that locally about the base of the nozzle, an uncoupled CFD–DSMC jet interaction simulation, with the plume surface defined with $P = 0.02$, is not appropriate, which is evidenced by the difference in local pressure and simulated oil flow of the two flow solutions shown in Figure 3.36.

Although the differences between the flow field and surface properties of these two simulations are apparent only by a detailed analysis, they show that for a jet interaction with $Kn_d = 0.038$, the choice of plume breakdown parameter value does have an effect for the flat plate geometry. Moreover, for complex configurations with a similar Kn_d value, the resultant interacting flow may impinge on a downstream surface. To describe these types of flow, the choice of the breakdown parameter value may be more critical than for the present simulation.

Chapter 4

MGS Jet Interaction with Rarefied Flow

In this chapter, the uncoupled CFD–DSMC technique discussed in Chapter 2 and applied to the flat plate interaction in Chapter 3 is exercised to predict aerodynamics for the Mars Global Surveyor (MGS) planetary probe during an actively controlled aerobraking maneuver. In addition to providing an application of the present uncoupled CFD–DSMC method to simulate a flight condition jet interaction case, previous calculations for the same flight condition are available and allow a limited verification of the present method.

4.1 MGS Aerobraking Maneuver

The MGS is a Mars orbiter, which is designed to obtain surface, atmospheric, and magnetic data about the planet with its onboard instrumentation. The mission life is planned to end early January 2000. Launched on November 7, 1996, the MGS reached Mars orbital insertion September 11, 1997. The original mission plan called for an aggressive series of about 300 aerobraking orbits where the vehicle would lose orbital momentum to frictional drag by successively passing the vehicle, in an aerobraking configuration, through the upper Mars atmosphere during periapsis (the lowest altitude of an orbit). The purpose of the aerobraking activity is to passively change the highly

elliptic post-insertion orbit to a more circular mapping orbit without extensive expenditure of onboard propellant (See Lee [45] for a more comprehensive explanation of the aerobraking maneuver and other aspects of the MGS mission.).

The original aerobraking schedule and configuration were changed because the solar panel yoke, which connects the 2-axis gimbal mechanism to the solar panel array, was damaged when the MGS solar panels were deployed shortly after launch. However, the original aerobraking configuration was extensively studied by Shane [77] and Shane et al. [76] using the DSMC code, X2, of Rault [63] and [64]. The aerobraking studies of Shane included simulations of the attitude control system (ACS) thrusters during periapsis when the atmospheric density of an orbit is greatest and jet interaction with the free stream has the most affect. For the jet interaction studies of Shane [77], the Mars atmospheric density, $\rho_{\infty} = 120 \text{ kg/km}^3$ and temperature, $T_{\infty} = 148K$, and the free stream velocity, $V_{\infty} = 4811 \text{ m/s}$. Also, the free stream gas mixture on a per mole basis is composed of 95.5% CO_2 , 2.7% N_2 , 1.6% Ar , and 0.2% O_2 .

Results from the jet interaction studies of Shane [77] and Shane et al. [76] are compared with results obtained from the present uncoupled CFD–DSMC technique and are presented subsequently. For the comparison, two solutions for each angle-of-attack case are presented, one flow field with no jet interaction and the other, a jet interacting with the flow field. Also, note that the ACS thruster of the previous MGS jet interaction study [77] and [76] was modeled by a disc with continuum jet nozzle exit conditions imposed as an inflow boundary to the DSMC simulation, which does not adequately define the detailed jet flow physics.

The original aerobraking configuration of the MGS, shown in Figure 4.1, provides

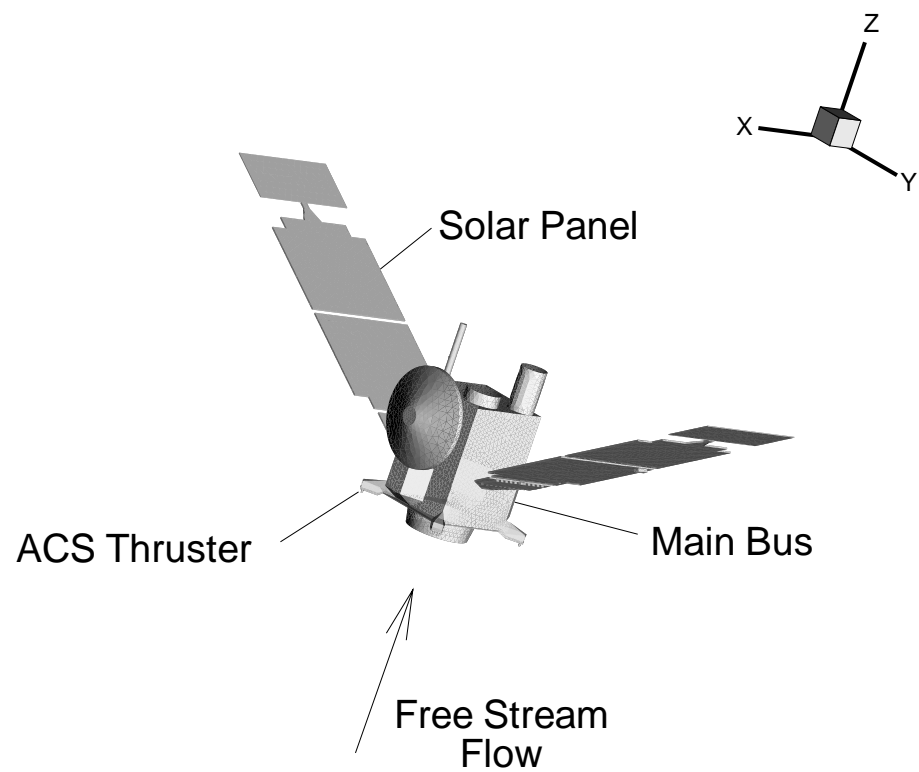


Fig. 4.1. Surface geometry of the Mars Global Surveyor (MGS) aerobraking configuration.

the directional orientation of the MGS during an aerobraking pass. Presented in the upper right hand side of the figure is a 3-D axis, which shows the coordinate directions used for the MGS model. Note that the solar panels are configured so that they are swept back 30° from the x-y plane during the aerobrake maneuver to provide a nominally stable aerodynamic shape. The main bus of the MGS has dimensions of about 1.5 m square in the x-y plane and is about 3 m high (in the z-direction), and the solar panel array, including the drag flap at the end of the panel, is about 5 m in length and 2 m wide. Also shown in Figure 4.1 is the location of one of four rocket engine modules, which consists of three ACS thrusters (two facing forward and one sideways for roll control). The other three modules are located symmetrically about the main bus in the same x-y plane. The exit diameter of each ACS thruster is 0.015 m (See Lee [45] for other MGS details.).

4.2 CFD Modeling of Attitude Control System (ACS) Thruster

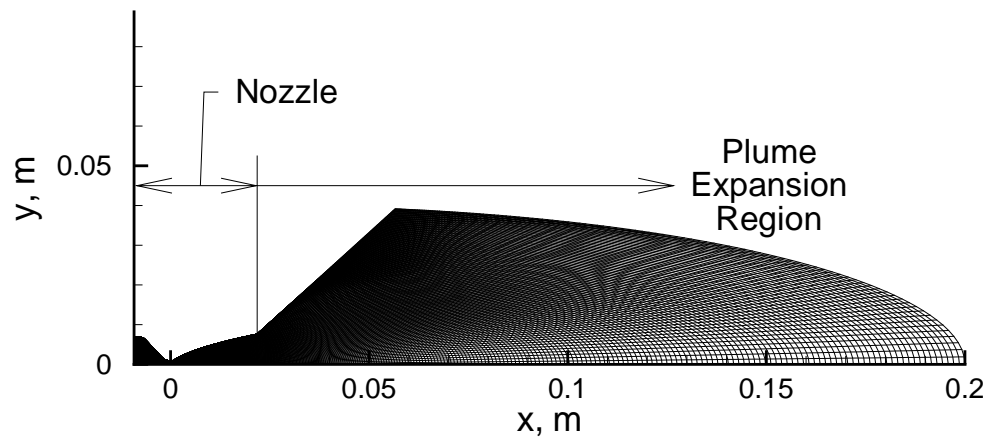
For the present uncoupled CFD–DSMC flow solution for the MGS during its aerobraking maneuver, first the ACS continuum flow solution to the breakdown surface must be obtained. The ACS thrusters used on the MGS vehicle are Primex (formally Rocket Research Company) model MR-111C monopropellant hydrazine rockets (Tolson [84]). To produce thrust, hydrazine (N_2H_4) is passed through Shell 405, an iridium impregnated aluminum oxide, and is decomposed catalytically into a high-temperature and high-pressure mixture of ammonia (NH_3), nitrogen (N_2), and hydrogen (H_2), which is expanded through a nozzle and exhausted at the nozzle exit. Details and a brief history

of monopropellant hydrazine technology are given by Eggers [21], Russi [71], Sackheim et al. [72] and Marcus [48].

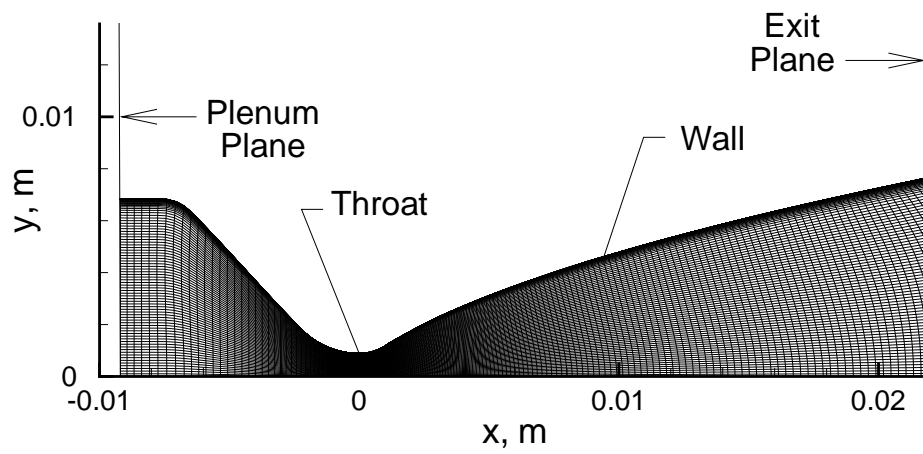
A CFD solution for the current MR-111C ACS thruster configuration, from the plenum, through the nozzle throat and internal expansion, and the external expansion from the nozzle exit into a jet plume, is produced by the GASP (AeroSoft [2]) computer program. This program has been successfully employed previously to produce continuum jet plume solutions for the Shuttle Orbiter PRCs thrusters (See Lumpkin et al. [47] and Rault [64].).

The nozzle contour for the MR-111C ACS thruster was obtained from Tolson [84] and the boundary conditions for the calculations from Morris [51]. The computational domain for the ACS thruster solution is shown in Figure 4.2a. A closeup view of the nozzle region, from the plenum to exit, is shown in Figure 4.2b. The nozzle is a converging-diverging type, which produces supersonic flow at the exit. As shown in the figure, the computational domain consists of 400 cells in the flow direction and 120 cells from the nozzle center line to the outer boundary with one-half of the computational cells used to calculate the nozzle internal flow. The domain consists of one cell circumferentially because only an axisymmetric flow solution of the thruster is needed. Also, the grid shown in Figure 4.2b is finely spaced near the nozzle wall to define the nozzle wall boundary layer.

The ACS thruster is an impulsive type, which is either fully off or on, and Morris [51] indicates that a solution for the maximum thrust condition with plenum conditions of $T = 1167\text{K}$ and $p = 0.978\text{ MPa}$ would best represent the thruster on condition.



a) Nozzle and expansion region.

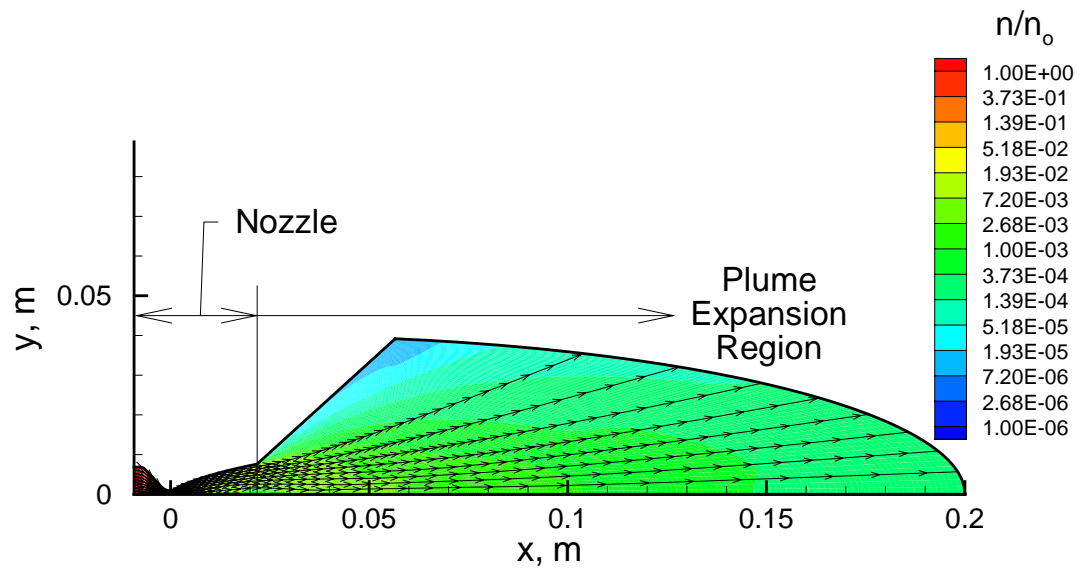


b) Closeup view of nozzle region

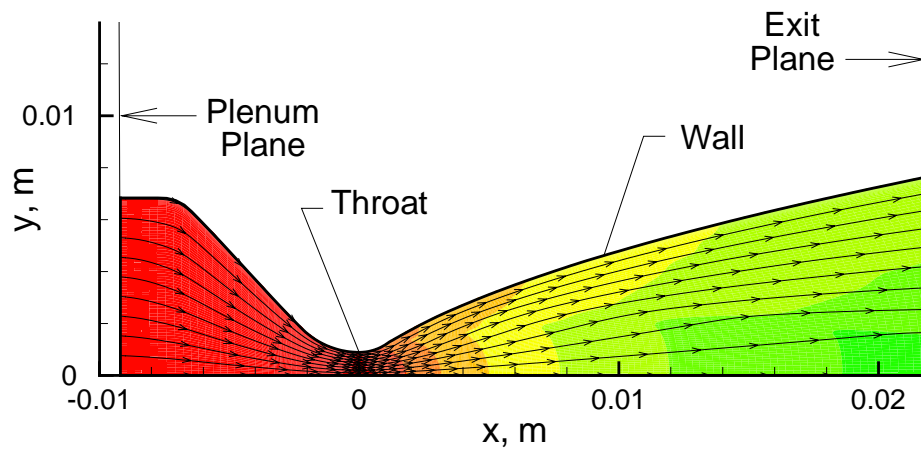
Fig. 4.2. CFD grid for the MGS ACS thruster (Primex MR-111C).

Additionally, he suggests a frozen mixture with a mole fraction of 19% ammonia, 30% nitrogen, and 51% hydrogen be imposed at the plenum plane, and that a no-slip constant temperature wall of 500K be used for the nozzle wall boundary condition. Outside the nozzle, the flow expansion region was bounded by a slip wall, which extended 45° from the nozzle center line axis (Morris [51]). This outer bounding angle was chosen for the expansion region to prevent the CFD solution from diverging because the local temperature may become artificially negative during the solution process with a greater expansion angle (See Figure 4.2a.). Stuart [81], who routinely produces CFD solutions for expanding jet plumes using the GASP computer program (see References [47] and [64]), also recommended that the flow outside the nozzle exit be modeled as inviscid because the viscous contribution to a freely expanding flow is minimal. A first-order extrapolation from the interior cell values was imposed as a boundary condition on the domain out-flow boundary. The advice of both Morris [51] and Stuart [81] was used to produce the present continuum flow ACS thruster solution.

Given the grid and the boundary conditions discussed above, a CFD solution for the ACS thruster was produced. The final solution L_2 norm was reduced more than 10 orders of magnitude to a constant value from the no flow initial condition. The solution was considered converged when the L_2 norm became constant as the flow field solution no longer changed between time integration steps. Shown in Figure 4.3 are normalized number density contours and flow streamlines from the ACS thruster solution. The entire solution domain is shown in Figure 4.3a, including the expansion region. Note that the flow streamlines in the outer expansion region do not expand to the slip wall, which is 45° from the center line axis. Therefore, this outer slip wall boundary location



a) Nozzle and expansion region.



b) Closeup view of nozzle region.

Fig. 4.3. Number density contours and streamlines for MGS ACS thruster.

is sufficient to define the expanding nozzle flow field. Figure 4.3b shows a closeup view of the number density contours in the nozzle from the plenum to the nozzle exit condition. Although not shown in the figure, the average Mach number at the nozzle exit plane is about 6.25.

4.3 Breakdown of Continuum Jet Flow

The uncoupled CFD–DSMC simulation of the flat plate jet interaction presented in Section 3.4, with the Knudsen number based on jet diameter, $Kn_d = 0.038$, by definition, represents a jet interaction in the transitional–rarefied flow regime. The correlation given in Figure 3.10 applies only to jet interactions with a similar level of flow rarefaction. The present MGS ACS jet interaction, however, has a Knudsen number based on jet diameter of $Kn_d = 49$, which describes a jet interaction with a moderately rarefied flow regime. Because the MGS ACS jet interaction is with a rarefied free stream, a Bird breakdown parameter value of $P = 0.02$ is appropriate to define the continuum jet plume breakdown surface. Note that for $P > 0.02$, the expanding flow is not in thermal equilibrium and is not adequately defined by a continuum CFD analysis.

The flow field of the ACS thruster outside the nozzle, shown in Figure 4.3a, is analyzed to determine the extent of flow in the expanding region that should be considered as continuum. As with the flat plate jet interaction, the Bird breakdown parameter, P , is defined by Equation 3.10 with the collision frequency, ν , defined by Equation 3.11. A difference in defining P and ν for flat plate jet plume and the present ACS jet plume is that the flat plate jet is a single species and the ACS jet is a gas

mixture. An effective molecular diameter, d_{eff} , and molecular mass, m_{eff} , are needed for the gas mixture to calculate P using Equations 3.10 and 3.11.

A definition for the effective molecular diameter, d_{eff} , is obtained by manipulating Equations 1.35, 1.40, 1.41, 4.1, and 4.8 presented by Bird [11], and is given as:

$$d_{eff} = \sqrt{\frac{1}{2^{1/2}\pi \sum_{p=1}^S (n_p \lambda_p)}} \quad (4.1)$$

where S is the total number of species in the mixture and $n_p \lambda_p$ is:

$$n_p \lambda_p = \frac{n/n_p}{\sum_{q=1}^S [(n/n_q)\pi(\frac{d_p+d_q}{2})^2(1 + \frac{m_p}{m_q})^{1/2}]} \quad (4.2)$$

Finally, an effective molecular mass, m_{eff} , is given as:

$$m_{eff} = \frac{M_{mix}}{N} \quad (4.3)$$

Substituting the effective molecular diameter and mass obtained from Equations 4.1 and 4.3, respectively, into Equations 3.10 and 3.11, and performing the analysis for $P = 0.02$, yields the breakdown surface shown in Figure 4.4. Note the difference in the shape of the supersonic ACS nozzle breakdown surface and the sonic flat plate jet shown in Figure 3.11. The supersonic jet breakdown surface does not expand outward from the centerline axis to the same extent as the breakdown surface from the sonic jet. Because the ACS nozzle exit Mach number is about 6.25, the maximum Prandtl-Meyer turning angle of the supersonic jet is less than that of the sonic jet, resulting, therefore, in the difference in the shape of the two breakdown surfaces.

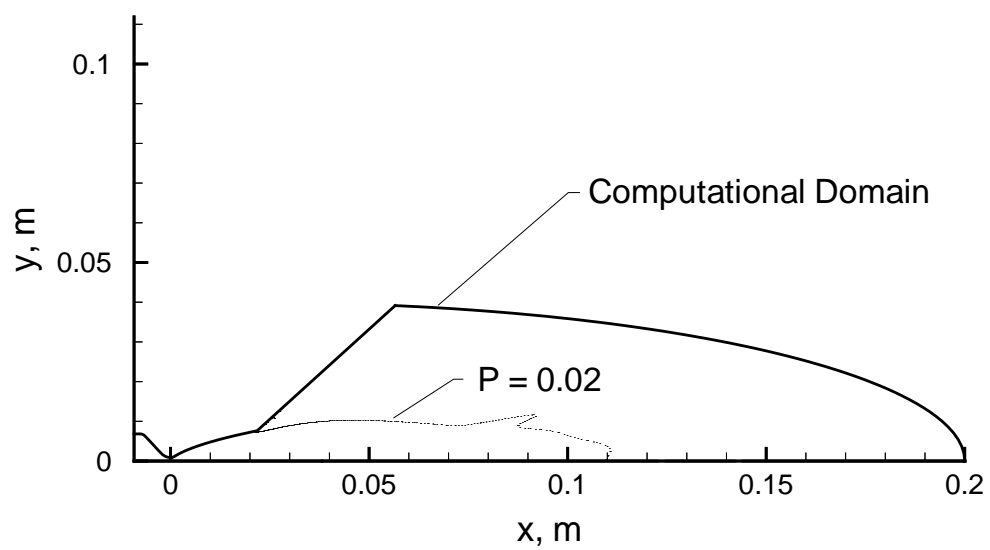


Fig. 4.4. $P = 0.02$ breakdown surface location for MGS ACS thruster.

4.4 Surface Triangulation for DSMC

To perform molecular simulations for the MGS during its aerobraking maneuver without and with the jet interacting flow fields using the DAC series of programs (LeBeau [44]), a triangulated surface description with the proper boundary conditions for both configurations is required. A surface description of the MGS geometry with no ACS rocket engine modules was obtained from Wilmoth [93] and served as a template for the two required configurations. The GridTool program (Samareh [73]) provided a graphics environment to create surface patches for the ACS jet modules and the $P = 0.02$ ACS jet plume surface, and merge them at the proper location on the spacecraft. ACS jet module surfaces were created directly in the GridTool environment; however, the jet plume shape was first transferred from the cloud of points representation shown in Figure 4.4 to an IGES surface description with the Surfacr program (See Imageware [39].); then, the IGES file was read into the GridTool program. The IGES graphics format is a compatible input file type for the GridTool program.

After producing the closed volume MGS configurations with GridTool, grid control sources [60] were placed strategically about both geometries to control the size distribution and number of triangles used to describe each surface. As an option, the GridTool program outputs a FELISA (Peirò et al. [60]) formatted input file. The surface triangulation routine of the FELISA program read the GridTool output files and created the triangulated surface description for the MGS configuration without and with the jet.

Finally, an author written code, *ftodac*, translated the FELISA file to the DAC format and applied the appropriate boundary conditions for all of the surface triangles.

The MGS surface boundary condition is non-catalytic, fully diffuse with full momentum accommodation with a wall temperature of 300K. These conditions match those used in the MGS study by Shane [77]. For each triangular element of the $P = 0.02$ ACS jet plume surface, the *ftodac* code interpolated the jet plume properties from the CFD flow field and assigned those properties to the plume outgassing surface at that spatial location.

The surface description of the MGS with no jet consists of about 26,000 triangles and was used to create the image shown in Figure 4.1, and the MGS configuration with the jet plume consists of nearly 37,000 triangles, of which 1300 triangles define the $P = 0.02$ plume surface. A closeup view of the ACS thruster and jet breakdown surface is shown in Figure 4.5, which was created using the DAC triangulated surface.

4.5 DSMC Modeling of MGS

As discussed previously, DSMC for two configurations, the MGS without and with a jet interaction flow field during an aerobraking maneuver, is applied and the aerodynamic results are compared with results from a similar study by Shane [77] and Shane et al. [76]. The comparison of the studies is made between the calculated yawing moment coefficient as a function of angle-of-attack ($C_{Mx} = f(\alpha)$). To produce the moment coefficient for the comparison, molecular simulations at five angle-of-attack flow conditions for each configuration have been performed and analyzed. Flow direction for each configuration was changed to produce angle-of-attack ranging from -15° to 15° in 7.5° increments. Free stream flow conditions for the simulations were given previously in

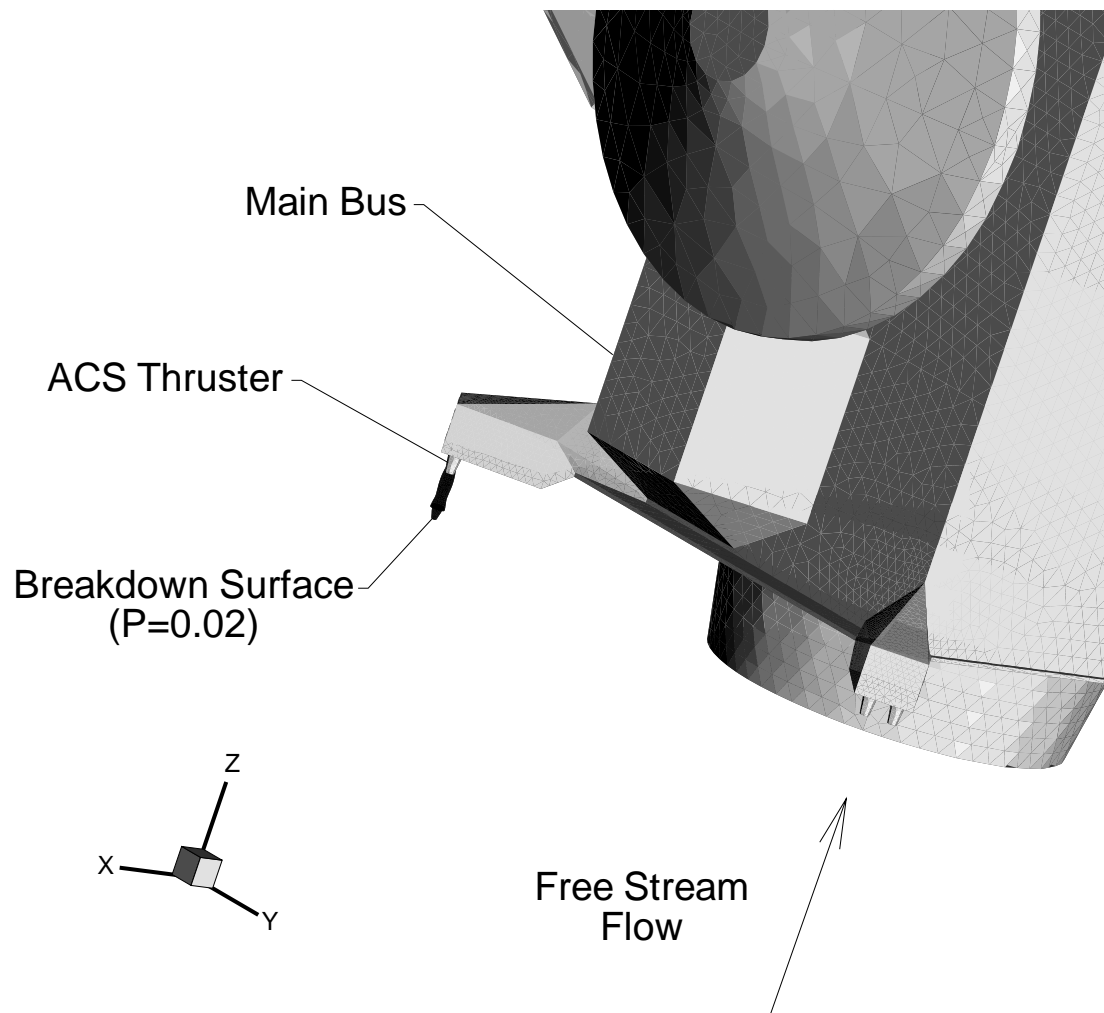


Fig. 4.5. Closeup view of MGS ACS thruster and $P = 0.02$ breakdown surface.

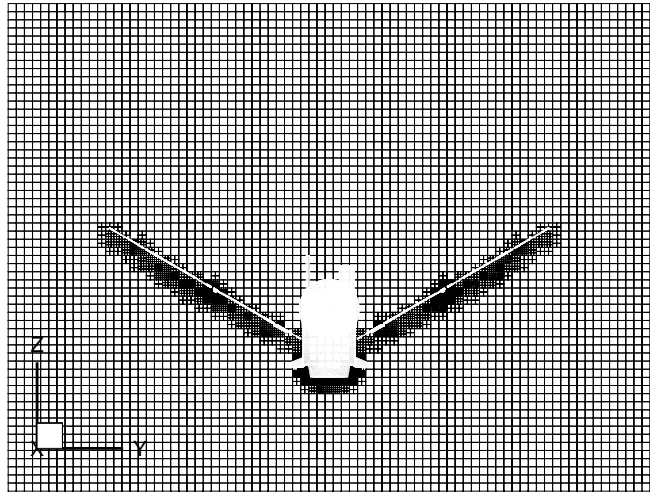
Section 4.1. Although molecular simulations for five angle-of-attack cases were accomplished, flow results for only three angles are presented, the $\alpha = 0^\circ, \pm 15^\circ$ cases, because these cases represent the centered and angle limited configurations of the study.

4.5.1 MGS Flow Field Without Jet Interaction

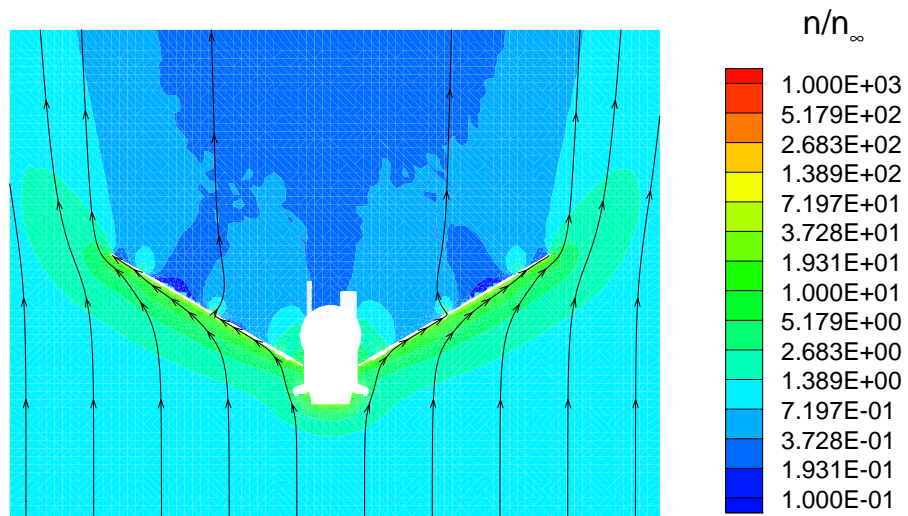
In this section, the flow field results of the molecular simulation for the MGS configuration with no jet interaction are presented. The simulation was applied by the DAC code of LeBeau [44], which has the option of grid adaptation based on a previous solution by clustering level II cells in the flow domain where higher density flow is present to better capture the flow field physics. For the present molecular simulations, adjusted simulation parameters for fine grid in higher density regions also allowed for better flow sampling and a more accurate flow simulation.

Two grid adaptation cycles were required for each of the no jet interaction cases before the change in calculated moment coefficient between the last two molecular simulations was insignificant. The difference in moment coefficient for the zero degree angle-of-attack case, which is typical of the other cases, was 0.00037. The corresponding difference in the x-directed moment was 0.081 N-m.

Shown in Figures 4.6a and b are the final adapted grid and normalized number density contours for the zero degree angle-of-attack no jet interaction case. The cross section (y-z plane) shown in the figure is at the center of the MGS main bus ($x = 0.000$ m). Note that the number density is normalized by the free stream number density. Also included in Figure 4.6b are flow streamlines, which show the free stream flow direction is from the bottom to the top of the figure. The MGS is colored white in the grid



a) Final grid adaptation.



b) Number density coutours and streamlines.

Fig. 4.6. Planar cross section of MGS flow field with no ACS jet interaction ($\alpha = 0^\circ$).

and number density contour figures to better locate it within the surrounding flow field domain.

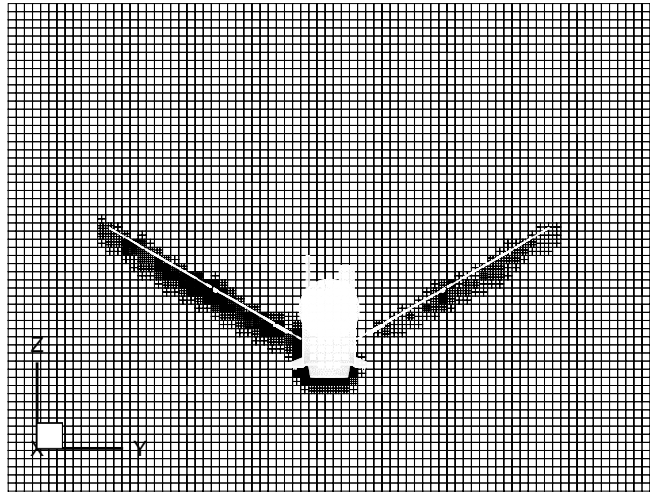
For the uniform, first, and second adapted grid solutions of each angle-of-attack case, the parallel version of the DAC series was employed on local SGI workstations with R10000 CPUs. The total time to produce a molecular simulation for the zero degree angle-of-attack case was 222.6 node hours, and the final adapted grid solution required 332 Mbytes of distributed memory. The second adapted grid consisted of about 310 thousand active cells with 3.17 million simulated molecules. Once the number of molecules in the simulation became steady, the sampling arrays were cleared, and 2500 steady state samples were obtained so that the statistical error of the simulation is about two percent. Computational time and memory requirements for the other angle-of-attack cases were similar.

The second grid adaptation, shown in Figure 4.6a, produced a grid with minimum cell dimensions of one local mean free path based on the previous flow field solution. Note the fine grid clustering (of level II cells) about the windward side of the main bus and solar panels, where the number density is higher as shown by the contours in Figure 4.6b. High number density pockets are also shown about the leeside of the aerobraking MGS configuration because of flow moving between the main bus and yoke, the yoke and inner solar panel, the inner and outer solar panels, and the outer solar panel and drag flap. The yoke, inner and outer solar panels, and drag flap are individual components of the solar panel, which is shown in Figure 4.1.

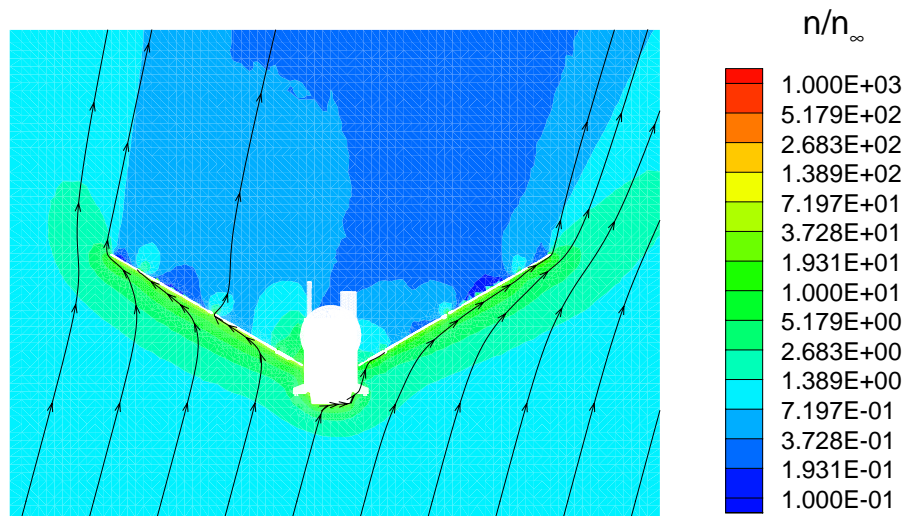
The second adapted grid and number density contours for the no jet interaction, $\pm 15^\circ$ angle-of-attack MGS molecular simulations are shown in Figures 4.7 and 4.8, respectively. The streamlines shown in the figures indicate the direction of the free stream flow with respect to the aerobraking MGS configuration. Free stream flow is directed from the lower left to upper right side in Figure 4.7b for the 15° angle-of-attack case, and for the -15° case, it is directed from the lower right to upper left side as shown in Figure 4.8b.

Finer, tightly clustered, level II cells are shown in the region about the side of the main bus and solar panel that is more directly exposed to the incoming free stream flow; for example, the flow field about the solar panel on the left side in Figure 4.7 is defined with a greater number of fine cells than the right side solar panel. Likewise, for the -15° angle-of-attack case, compare the cell distribution about the solar panel on the right side in Figure 4.8 with one on the left side.

Also, number density contours are more closely spaced on the more directly exposed solar panels indicating larger local density gradient (See the density contours just upstream of the left solar panel shown in Figure 4.7 and those just upstream of the right solar panel shown in Figure 4.8.). The higher density gradient is because the free stream flow is directed more normally to the exposed solar panel surface and turns through less of an angle than for the other solar panel. In addition, the direction of the free stream flow skews the number density contours upstream and downstream of the MGS configuration. Note the asymmetric appearance of the number density shown in Figures 4.7b and 4.8b when compared to the number density contours shown in Figure 4.6b.

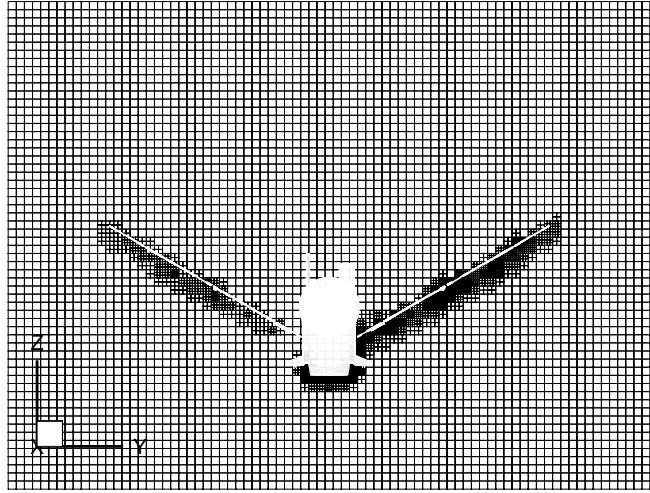


a) Final grid adaptation.

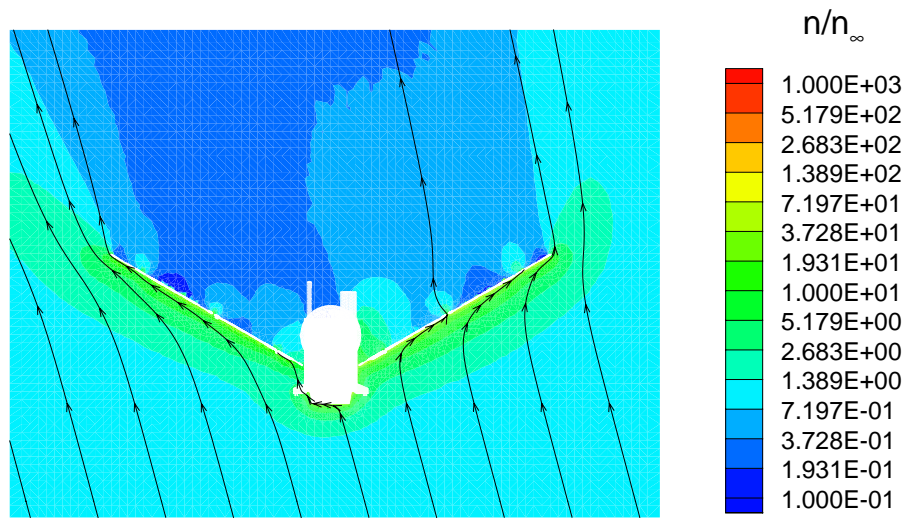


b) Number density coutours and streamlines.

Fig. 4.7. Planar cross section of MGS flow field with no ACS jet interaction ($\alpha = 15^\circ$).



a) Final grid adaptation.



b) Number density coutours and streamlines.

Fig. 4.8. Planar cross section of MGS flow field with no ACS jet interaction ($\alpha = -15^\circ$).

4.5.2 MGS Flow Field With Jet Interaction

Presented below are flow field results about the MGS aerobraking configuration with an interacting ACS jet thruster. Procedures for implementing the uncoupled CFD–DSMC method, developed previously, are followed to define the configuration used for the present molecular simulation. The configuration consists of a triangulated MGS surface and an appropriately attached thruster plume. Thruster plume flow properties, used as an inflow boundary to the DSMC domain are defined on the $P = 0.02$ breakdown surface, as discussed in Section 4.3. Shown in Figure 4.5 is a closeup view of the ACS jet plume attached to a thruster on the MGS main bus. As with the previous molecular simulations, the DAC series of programs (LeBeau [44]) was applied to perform the DSMC and define the flow interaction of the ACS jet with the free stream. Additionally, multiple adaptation cycles were required to assure the final results were obtained with acceptable resolution.

Since yawing moment coefficient is the quantity sought for the comparison with results of Shane [77], the difference in yawing moment coefficient between the previous and current adaptation cycle was monitored to provide an indication of solution convergence. When the difference was reduced to a negligible value, grid adaptation cycles were discontinued. This occurred for the present zero degree angle-of-attack case after one uniform and three adaptation cycles were completed and resulted in a yawing moment coefficient difference of 0.00039 between the second and third adaptation cycle results. In terms of dimensional yawing moment, the difference is 0.086 N-m between the two solutions.

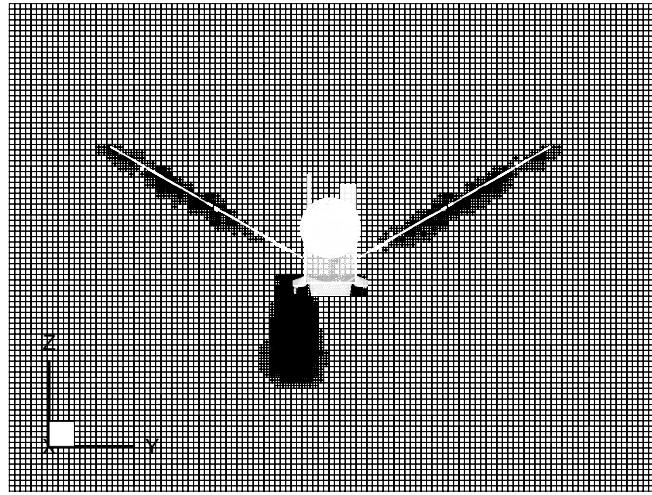
The DSMC for the flow field about the MGS with an interacting ACS jet was performed using the parallel version of the DAC series (LeBeau [44]) executed on local SGI R10000 CPUs. The LAM (Ohio Supercomputer Center [56]) version of MPI provided the computer connectivity, which consisted of up to 17 computers, depending on the particular adaptive cycle of the solution being executed. The final adaptive cycle for the zero degree angle-of-attack case, typical of the other jet interaction cases, had the greatest number of computers linked in parallel and consisted of 1.1 million cells with a total of 9.2 million steady state molecules and a distributed memory of 1.1 Gbytes. The total computational time required for the simulation was 880 node hours, of which 650 node hours were used for the final adapted grid simulation to obtain 2500 steady state samples.

The final adapted grid for the jet interaction case resolved the flow domain into cells of at least one mean free path. It should be noted that, for the present ACS jet thruster, if the plume flow field from the thruster exit to the $P = 0.02$ breakdown surface were resolved into cells of one mean free path, it is estimated from the CFD solution that the molecular simulation for the plume alone would require nearly 600 million cells or, with an average of 10 molecules per cell, about 6 billion molecules. The computational memory requirement of the simulation would be about 600 Gbytes based on the jet interaction case; resources for such a calculation are not available. By calculating first the continuum portion of the plume using CFD and considering it as an outgassing plume surface, a molecular simulation using DSMC for the MGS jet interaction with an appropriate cell spacing becomes a tractable problem with present computer technology.

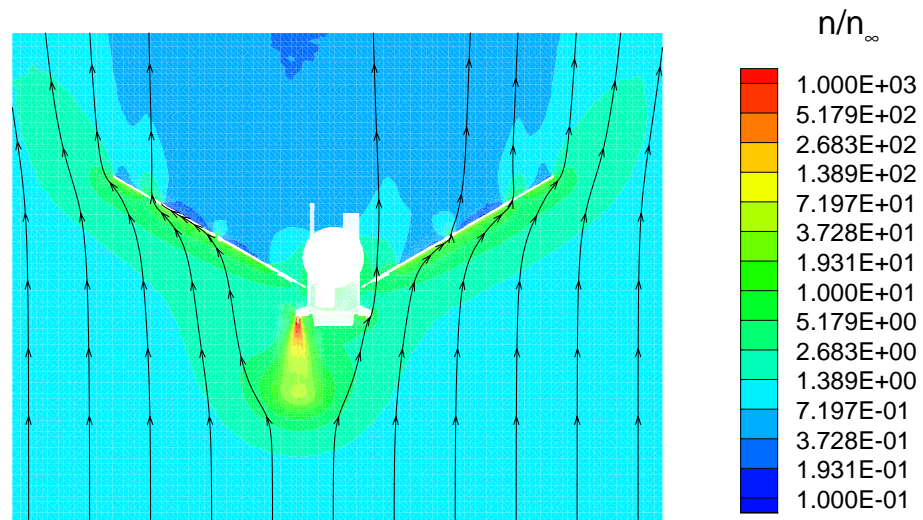
Presented next are the final adapted grid and flow field results at the y-z plane cross section of the thruster plume location ($x = 0.8$ m) for three of the cases. Results for five cases were produced; however, only those for the 0 and $\pm 15^\circ$ angle-of-attack cases are presented because they represent the mid-point and extremes of the angle-of-attack range. Shown in Figure 4.9a and b are the grid and number density contours, respectively, for the zero degree angle-of-attack case. As was done with the figures presented for the no jet interaction cases (See Section 4.5.1.), the MGS is colored white in the grid and number density contour figures to better locate it in the flow field.

Level II cells for the third grid adaptation, shown in Figure 4.9a, are so closely spaced in the region of the high density plume that the individual cells blend together to form a black region upstream of the ACS plume, which is located on the left side of the MGS main bus as shown in Figure 4.5. Note that the area occupied by the fine cells (the black region shown upstream of the plume in Figure 4.9a) is nearly the same size as the MGS main bus.

The effect of the thruster on the free stream flow field is quantitatively demonstrated by the number density contours shown in Figure 4.9b. The ACS jet for this case produces significant influences on the free stream about 3.3 m upstream of the main bus, compared to the no jet case where the influence of the bus is less than one meter upstream as shown in Figure 4.6b (For reference, the straight line distance between the outer solar panel drag flaps shown in the figure is 11 m.). The jet plume causes the number density contours upstream of the MGS to bulge more on the left side than on the right because the plume is offset about 0.8 m to the left of the main bus centerline. This offset of the plume causes a shadowing from the free stream of the portion of the



a) Final grid adaptation.



b) Number density coutours and streamlines.

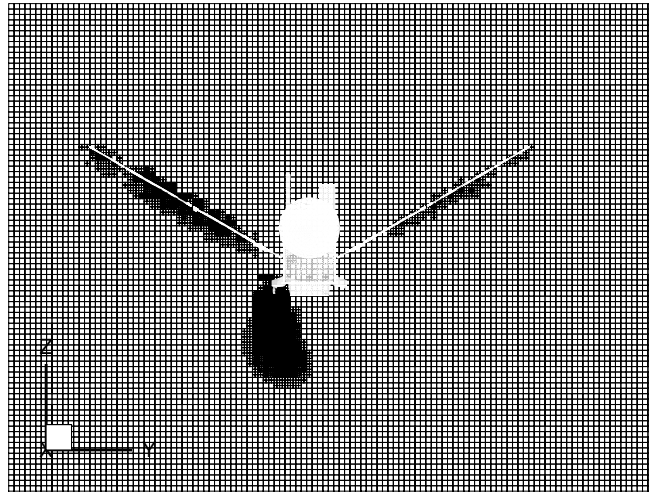
Fig. 4.9. Planar cross section of MGS flow field with ACS jet interaction ($\alpha = 0^\circ$).

left solar panel closest to the main bus. The free stream flow is also deflected as shown by the streamlines in Figure 4.9b.

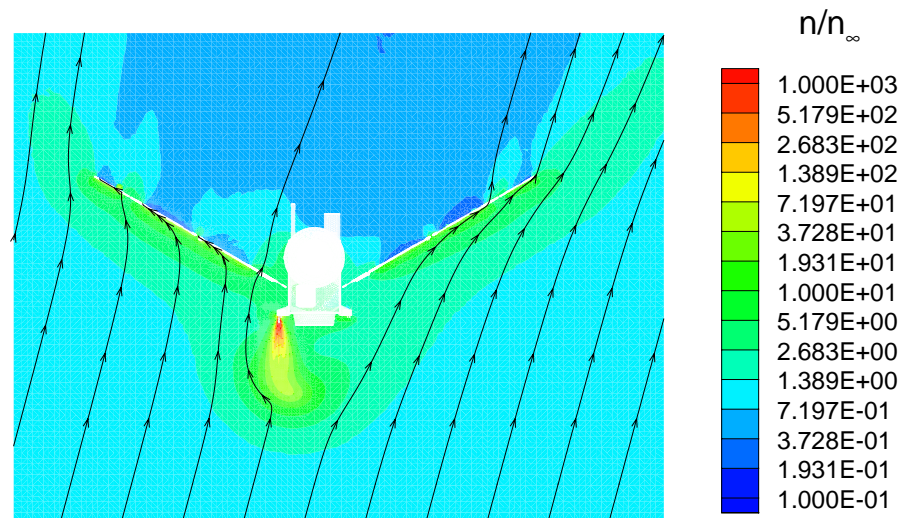
Presented in Figure 4.10 are the final adapted grid and number density contours for the 15° angle-of-attack MGS jet interaction case. The figure shows a flow cross section of the y-z plane at the ACS thruster location. Similar to the zero degree angle-of-attack case, level II cells are closely spaced upstream of the plume (shown by the black region in Figure 4.10a); however, unlike the cells of the zero degree angle-of-attack case shown in Figure 4.9a, the cells are asymmetrically distributed with more cells to the right.

Number density contours presented in Figure 4.10b show an asymmetric deflection of the plume to the right, which is consistent with the jet plume flow interacting with the free stream flow directed from the lower left to the upper right in the figure. In addition, number density is higher on the left solar panel than on the right solar panel because the flow at 15° angle-of-attack impinges more directly on the left panel and because the thruster plume shadows a portion of the right panel by deflecting the free stream flow. Also note that grid clustering near the solar panels shown in Figure 4.10a, which is based on the number density distribution of the previous solution cycle, indicates higher number density on the left solar panel than on the right.

Figure 4.11 shows the final adapted grid and number density contours for the -15° angle-of-attack MGS jet interaction case at the cross section location of the ACS thruster. The grid cross section (see Figure 4.11a) shows the level II cells at the plume location as a dark region upstream of the thruster because they are so closely spaced. Note that the plume grid farthest upstream from the thruster is skewed to the left. The

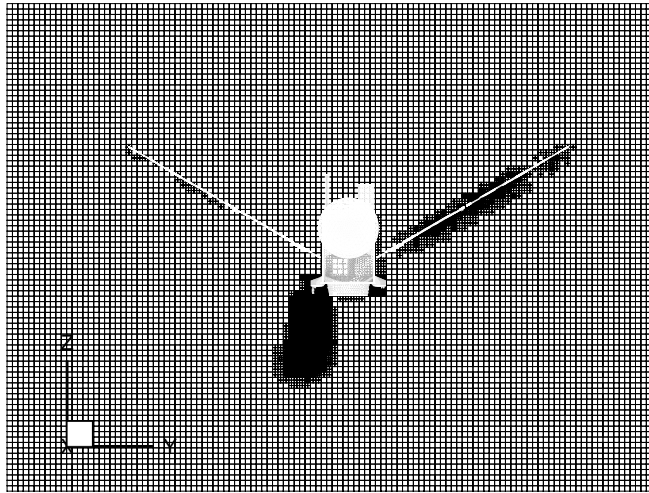


a) Final grid adaptation.

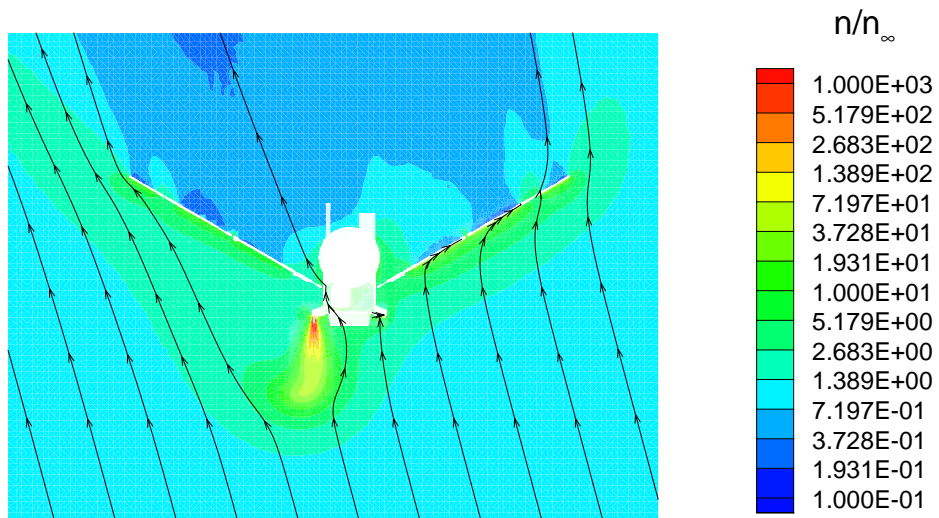


b) Number density contours and streamlines.

Fig. 4.10. Planar cross section of MGS flow field with ACS jet interaction ($\alpha = 15^\circ$).



a) Final grid adaptation.



b) Number density coutours and streamlines.

Fig. 4.11. Planar cross section of MGS flow field with ACS jet interaction ($\alpha = -15^\circ$).

grid near the right solar panel is also closely spaced with level II cells; however, the grid about the left solar panel is more coarsely spaced with many fewer level II cells.

Number density contours and streamlines at the thruster cross section are shown in Figure 4.11b, indicating that the high density plume expands upstream from the thruster and is skewed to the left, as it interacts with the free stream. For this case, the thruster plume shadows the left solar panel from the free stream more than the thruster plume shadows the right solar panel for the 15° angle-of-attack case (Compare the number density contours and streamlines in Figure 4.11b with those in Figure 4.10b.). The left panel for the present -15° angle-of-attack case is shadowed to a greater extent because the plume, which is on the left side, is more directly in front of the panel with respect to the free stream direction and deflects the flow. Note that the higher number density contours on the right solar panel for this case are similar to those of the no jet interaction -15° angle-of-attack case shown in Figure 4.8b because the plume minimally effects the right side solar panel.

4.5.3 MGS Surface Pressure Without and With Jet Interaction

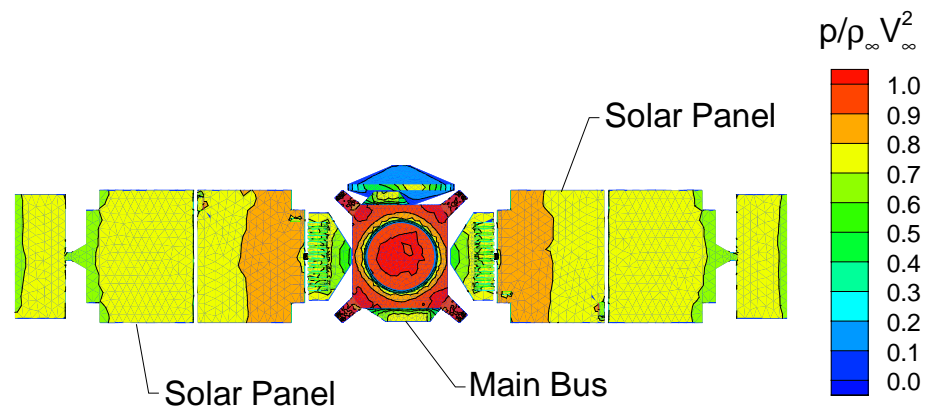
To further illustrate the effect of the ACS jet thruster interacting with the free stream, pressure contours on the windward surface of the MGS are presented in this section. In the previous two sections (Sections 4.5.1 and 4.5.2) the effect of the jet interaction on the flow field was presented, which showed that the ACS jet plume redirected the much lower density free stream and shadowed a portion of the MGS downstream surface so that the free stream flow did not impinge directly on the surface. This caused

a decrease in the flow field number density locally near the downstream surface. Presented subsequently is the effect of the interaction on the surface pressure. Moreover, because aerodynamics of the aerobraking MGS are sought for a comparison with previously published results, which is given in the next section, the windward surface pressure contours will show visually the effect of the interacting ACS jet with the rarefied flow.

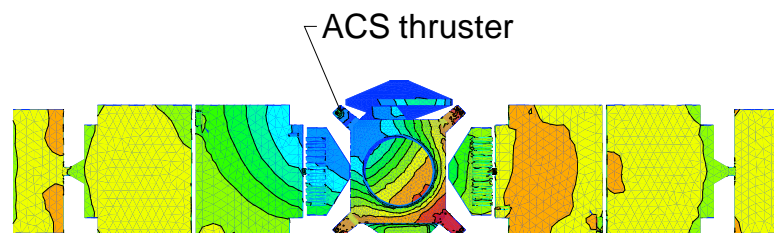
Given in Figures 4.12a and b are the surface pressure contours on the windward side of the MGS for the no jet and jet interaction cases, respectively, at $\alpha = 0^\circ$. The surface shown in the figure is oriented in the x-y plane opposed to the free stream direction (See Figure 4.1.). The contours shown in Figure 4.12a result from the flow field shown in Figure 4.6b; likewise, contours shown in Figure 4.12b result from the flow field shown in Figure 4.9b.

The pressure contours shown in Figure 4.12a are symmetric with the highest pressure on the base of the MGS main bus and windward side of the thruster modules. The pressure is lower on the left and right solar panels because they are swept 30° from normal impingement by the free stream flow. With the upper left ACS thruster fired, the pressure contours on the windward surface change substantially as shown in Figure 4.12b. Centered about the ACS thruster location is much lower pressure than for the case with no jet interaction (See Figure 4.12a.). As discussed previously, the higher density jet shadows the downstream portion of the MGS.

Presented in Figures 4.13a and b are windward surface pressure contours on the MGS at $\alpha = 15^\circ$ without and with ACS jet interaction, respectively. The flow field that produced the surface pressure contours given in Figure 4.13a is presented in Figure 4.7b,

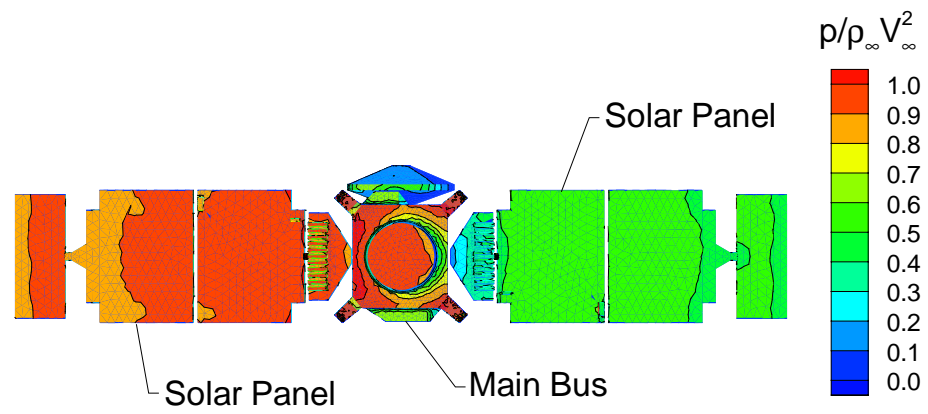


a) No ACS jet interaction.

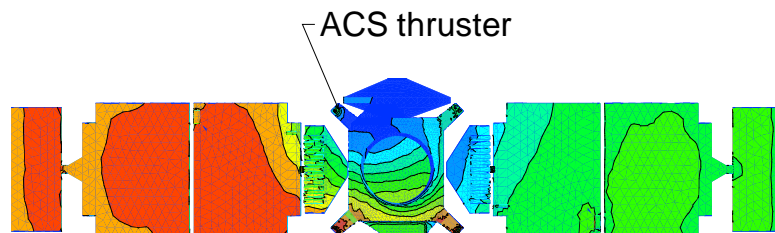


b) ACS jet interaction.

Fig. 4.12. Windward surface pressure contours on MGS ($\alpha = 0^\circ$).



a) No ACS jet interaction.



b) ACS jet interaction.

Fig. 4.13. Windward surface pressure contours on MGS ($\alpha = 15^\circ$).

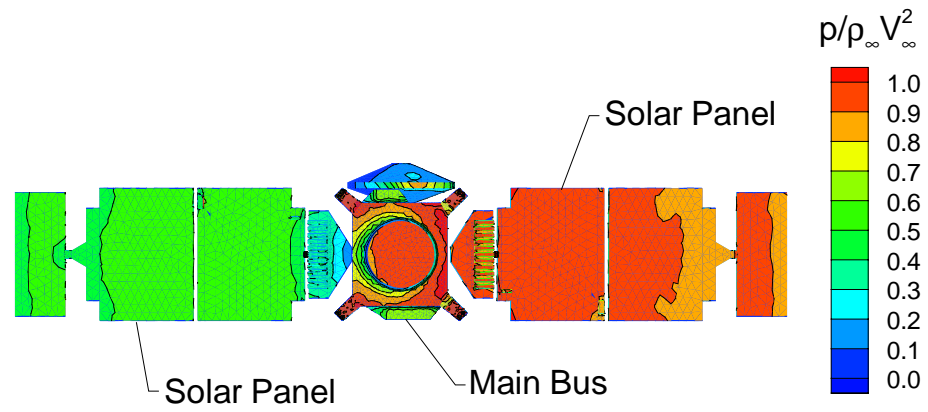
and the pressure contours given in Figure 4.13b are produced by the flow field presented in Figure 4.10b.

The left solar panel in Figure 4.13a is subjected to higher pressure than the right one because the free stream impinges more normal on the left panel. For example, see the flow field streamlines given in Figure 4.7b, which are directed from the lower left to the upper right and approach the left panel 15° from its surface normal, while the streamlines glance the right panel at 45° .

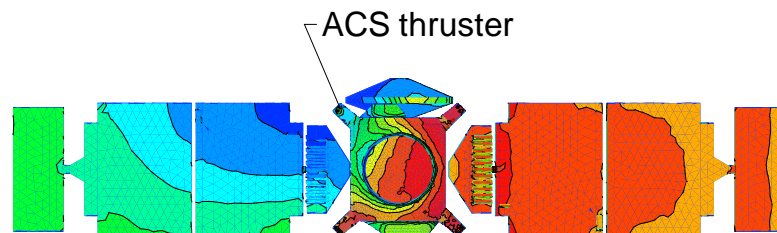
Figure 4.13b shows the surface pressure contours on the MGS at $\alpha = 15^\circ$ with an interacting ACS jet. The pressure in the vicinity of the firing ACS thruster on the main bus is much lower than on the left and right solar panels. Unlike the $\alpha = 0^\circ$ jet interaction case (See Figure 4.12b.), the lower pressure region for the $\alpha = 15^\circ$ case extends minimally onto both panels. The pressure on the right solar panel nearest the main bus is lower than that of the matching region on the left panel. The cause of this pressure distribution can be explained by observing the interacting flow field given in Figure 4.10b. The flow field streamlines in the figure demonstrate that the jet shadowing effect is centered about the corner of the MGS main bus, which is the region of lower surface pressure shown in Figure 4.13b.

Figures 4.14a and b show the MGS windward surface pressure contours for the no jet and interacting jet cases, respectively, at $\alpha = -15^\circ$. The flow field in Figure 4.8b produces the pressure distribution in Figure 4.14a, and the flow field in Figure 4.11b produces the pressure distribution in Figure 4.14b.

Because the free stream angle-of-attack for the $\alpha = -15^\circ$ simulation differs only in the direction of the cross flow velocity component from the $\alpha = 15^\circ$ simulation, the



a) No ACS jet interaction.



b) ACS jet interaction.

Fig. 4.14. Windward surface pressure contours on MGS ($\alpha = -15^\circ$).

pressure distribution on the MGS without jet interaction (shown in Figure 4.14a) is a mirror image of the one shown in Figure 4.13a having only switched sides—right to left—with angle-of-attack sign change. For example, the high pressure region is on the right solar panel for $\alpha = -15^\circ$ and on the left solar panel for $\alpha = 15^\circ$ (Compare Figures 4.14a and 4.13a.).

With an interacting jet at $\alpha = -15^\circ$, the MGS surface pressure (shown in Figure 4.14b) is reduced on the left side of the main bus and on the left solar panel when compared to the no jet case presented in Figure 4.14a. The flow field streamlines for this condition (shown in Figure 4.11b) are directed from the lower right to the upper left, and when the higher density jet plume interacts with the free stream and diverts the flow, a large portion of the left solar panel is shadowed. Moreover, because the left panel is swept 45° from the flow, it offers a smaller profile; thus, the jet plume affects a greater area of the panel.

4.6 MGS Aerodynamics

Aerodynamic yawing moment coefficient for the MGS without and with ACS jet interaction as a function of angle-of-attack is compared in this section. The comparison is made between results presented by Shane [77] and Shane et al. [76], which were generated by the DSMC X2 code, and the present no jet interaction results presented in Section 4.5.1 and jet interaction results presented in Section 4.5.2. The no jet interaction results were produced by employing the DAC series (LeBeau [44]), and the jet interaction results were produced using the present uncoupled CFD–DSMC method with the GASP computer program (AeroSoft [2]) and DAC series.

The post-processing routine of the DAC series (*sprop*) was employed to calculate aerodynamic moments from the MGS molecular simulations by summing (integrating) the vector product of pressure and shear force contributions with the position vector from a prescribed point to the centroid of each surface triangle. The point about which moments for the present study were taken is the same location used previously by Shane [77], which is at the center of the MGS main bus in the x-y plane and at the z-location near the attachment of the solar panel yoke and main bus. To obtain the moment coefficient, C_{Mx} , the moment is normalized by the product of the reference area, A , reference length, L , and free stream dynamic pressure, q . Values of these quantities for the MGS at the free stream density and velocity of the study are $A = 17.5 \text{ m}^2$, $L = 9 \text{ m}$, and $q = 1.39 \text{ Pa}$.

Calculated yawing moment coefficient for the MGS as a function of angle-of-attack about the x-axis, which is oriented in the direction shown by the 3-D axis in the upper right side of Figure 4.1, is presented in Figure 4.15. The square symbols shown in the figure are from the study by Shane [77], and the circular symbols are from the present study. Open symbols are used for results with no jet interaction, and closed symbols represent the cases with ACS jet interaction. Additionally, the direct thrust contribution of the ACS jet is included in all of the C_{Mx} jet interaction results presented in the figure. Although Shane [77] did not include the direct thrust contribution in his study, his jet interaction data have been modified for the present comparison to include the direct thrust contribution to the moment. The single ACS jet contribution to the yawing moment coefficient is $C_{Mx,jet} = -0.014$ based the exit plane thrust calculated from the ACS CFD results presented previously (See Section 4.2.). The effect of including the direct thrust contribution to aerodynamic moment coefficient is to bias the solid

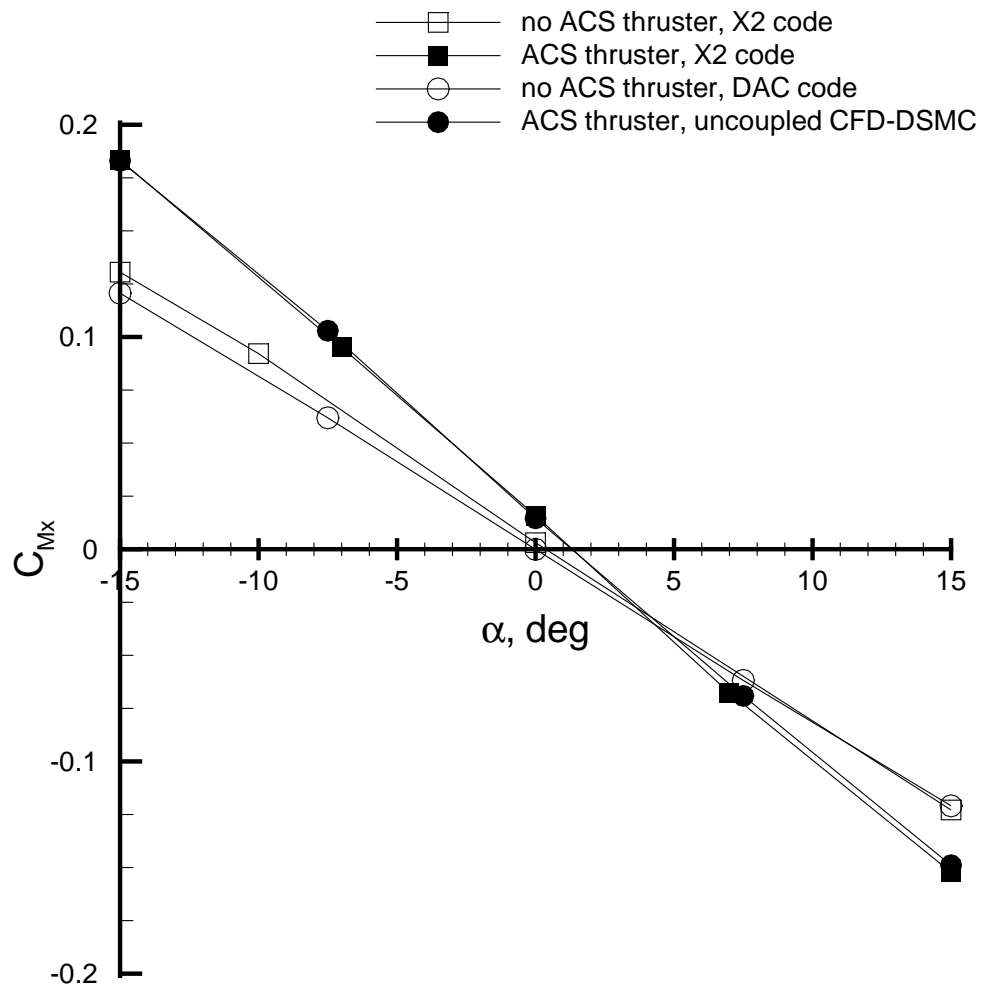


Fig. 4.15. Comparison of yawing moment coefficient for the MGS without and with ACS jet interaction.

symbols negatively in Figure 4.15 (by $C_{Mx,jet} = -0.014$), which then correctly shows the equilibrium trim condition is at an angle-of-attack of $\alpha \approx 1.5^\circ$ ($C_{Mx} = 0$).

Several conclusions can be made concerning the $C_{Mx} = f(\alpha)$ curve shown in Figure 4.15. The consequence of the ACS jet on the moment coefficient is not a superposition of the thrust contribution with the no ACS jet moment coefficient curve. Thruster plume shadowing of various portions of the MGS surface as a function of angle-of-attack alters the surface pressure distribution, which, when integrated over the surface, changes the slope of the C_{Mx} vs. α curve (to a larger negative value) for the aerobraking MGS configuration as well as shifting the trim attitude by 1.5° .

Moreover, for particular angle-of-attack ranges, the jet affects C_{Mx} differently because the net effect of direct thrust and plume shadowing varies with α . Thrust reversal occurs for $\alpha < 4.5^\circ$; that is, the negative moment increment from the ACS jet contribution does not cancel the positive moment generated from the redistribution of surface pressure because of the thruster plume shadowing on the MGS surface. At $\alpha \approx 4.5^\circ$, the ACS jet thruster has no net effect on the C_{Mx} value when compared to the no jet C_{Mx} value. However, for $\alpha > 4.5^\circ$, the change in C_{Mx} from the no jet value is negative; that is, the shadowing effect of the ACS jet on the moment is in the same direction as the direct thrust moment; therefore, only for $\alpha > 4.5^\circ$ is the ACS jet thruster providing a contribution in the expected direction.

The comparison presented in Figure 4.15 for the MGS jet interaction cases (solid symbols) shows that predictions from the present uncoupled CFD–DSMC method are in good agreement with those of Shane [77] for the ACS jet interacting with a moderately rarefied flow. Good agreement between the two independent studies gives increased

confidence in both results. Additionally, these studies provide insight into the underlying flow physics of the interaction, which is needed by mission planners to determine the effect of a jet thruster interacting with a rarefied flow field for the particular configuration and mission being studied.

Chapter 5

Concluding Remarks

An uncoupled CFD–DSMC technique has been developed, which provides solutions for continuum jet interactions in the rarefied flow regime. Because the density in the rarefied regime spans many orders of magnitude, the technique was applied to two problems: one of a jet interaction in the transitional–rarefied flow regime and the other in a more highly rarefied regime. For both flow regimes, the continuum and molecular analyses are uncoupled at an appropriate Bird breakdown surface.

Uncoupling the continuum and non-continuum portions of an interacting flow at an appropriate jet plume surface offers computational advantages because continuum CFD does not apply everywhere in the flow field and performing simulations exclusively with DSMC would require huge computational resources. It is estimated that the CFD–DSMC technique can reduce DSMC requirements for the entire flow field solution of jet interaction problems by about six orders of magnitude for a sonic jet interaction and about three orders of magnitude for a highly-expanded supersonic jet interaction.

A correlation was obtained for the interaction in the transitional–rarefied flow regime with $Kn_d = 0.038$, which shows that the appropriate Bird breakdown surface at the interaction interface for the uncoupling is a function of a non-dimensional parameter. The correlation is used to assure that the uncoupled surface is independent of the interaction effects; that is, the flow inside the surface is unaffected by the interaction

and the jet flow information passes only out of the surface. Thus, the CFD and DSMC solutions do not require an iterative coupling. Using the correlation, an uncoupled solution was obtained for an experimental test condition. Good agreement was shown in the non-interacting region with the Bird G2 code; however, because the experimental results are presently unpublished, no comparisons are included.

The uncoupled technique was also applied to an aerobraking flight condition of the Mars Global Surveyor spacecraft with an attitude control system jet interaction in the rarefied regime corresponding to $Kn_d = 49$. Results of the present method compared well with previously published results from the X2 DSMC code, which gives credence to applying the present method at that condition.

The present uncoupled CFD–DSMC technique has been shown to provide solutions for jet interactions in the rarefied flow regime. A correlation, which was obtained, gives guidance for uncoupling the continuum plume defined by a Bird breakdown parameter value, P , in the transitional–rarefied flow regime as function of free stream and jet properties. For other jet interactions, which are in a more highly rarefied flow regime, application of the method with a $P = 0.02$ plume provides a reasonable surface to uncouple the continuum jet from the surrounding interaction with the rarefied flow.

Chapter 6

Direction for Future Research

To more fully examine the interaction of continuum jets with rarefied flow, additional experimental and numerical studies are needed. Suggestions for some of these studies are itemized below:

- As a further validation of the present uncoupled CFD–DSMC technique, for example, a comparison between results from the current transitional–rarefied simulation and the experiment, when available, is needed. To facilitate this comparison, tabulated results from the present study are included in the Appendix.
- Systematic studies of jet interactions in the rarefied flow regime as a function of Kn_d using generic models, such as a flat plate at non-zero ($\pm\alpha$) incidence, cones, hemisphere–cones, corners, rear-facing steps, etc., which may represent local vehicle surfaces that issue reaction control jets, are needed to provide a data base of the resultant interaction flow fields.
- The RCS nozzle exit on the surface of a transatmospheric vehicle is blended to the outer mold line and does not necessarily issue normal from the surface. To understand this “real life” situation, studies of curved exit, non-normal issuing jet interactions are needed.

- Studies to define the effect of clustered multiple jets on the interaction are needed.

Generally, RCS jets are arranged so they are either fired singly or, if more thrust is needed, in groups of more than one. Multiple jet interaction studies will provide insight into how best to model the continuum portion of the flow to apply a numerical CFD–DSMC uncoupled scheme.

References

- [1] *21th International Symposium on Rarefied Gas Dynamics*, Universite de Provence, Marseille, France, July 1998.
- [2] AeroSoft. *GASP Version 3, The General Aerodynamic Simulation Program, Computational Flow Analysis Software for the Scientist and Engineer, User's Manual*. AeroSoft, Inc., May 1996.
- [3] J. Allègre and M. Raffin. Experimental study on control jet interaction (final report), ESA/ESTEC contract 111 191. Technical Report 608/91.1043, CNRS Aerothermique RC-91-11, SESSIA, December 1991.
- [4] J. Allègre, M. Raffin, and J. P. Caressa. Experimental investigation of transverse jet effects related to hypersonic space vehicles. In Battrick [8], pages 165–170. ESA-SP-318.
- [5] Amtec. *Tecplot User's Manual Version 7*. Amtec Engineering, Inc., Bellevue, Washington, August 1996.
- [6] Dale A. Anderson, John C. Tannehill, and Richard H. Pletcher. *Computational Fluid Mechanics and Heat Transfer*. Hemisphere Publishing Corporation, New York, 1984.
- [7] John D. Anderson, Jr. *Hypersonic and High Temperature Gas Dynamics*. McGraw-Hill, Inc., 1989.

- [8] B. Battrick, editor. *Aerothermodynamics for Space Vehicles, Proceedings of the First European Symposium*, ESTEC, Noordwijk, The Netherlands, May 1991. ESA-SP-318.
- [9] G. A. Bird. *Molecular Gas Dynamics*. Clarendon Press, Oxford, 1976.
- [10] G. A. Bird. *DSMC Computation of Two-Dimensional or Axially-Symmetric (G2) or Three-Dimensional with Axially-Symmetric Grid (A3) Rarefied Flows, The G2/A3 Program System Users Manual, Version 1.8*. G.A.B. Consulting Pty Ltd, Killara, Australia, March 1992.
- [11] G. A. Bird. *Molecular Gas Dynamics and the Direct Simulation of Gas Flows*. Clarendon Press, Oxford, 1994.
- [12] C. Borgnakke and P. S. Larsen. Statistical collision model for Monte Carlo simulation of polyatomic gas mixtures. *Journal of Computational Physics*, 18(4):405–420, 1975.
- [13] Iain D. Boyd, Gang Chen, and Graham V. Candler. Predicting failure of the continuum fluid equations in transitional hypersonic flows. *Physics of Fluids*, 7(1):210–219, January 1995.
- [14] C. Campbell, J. Caram, S. Berry, T. Horvath, N. Merski, M. Loomis, and E. Venkatapathy. Overview of the X-38 hypersonic aerothermodynamic wind tunnel data and comparison with numerical results. AIAA Paper 97–2475, June 1997.

- [15] CEI. *EnSight User Manual for Version 5.5.2*. Computational Engineering International, Inc., Research Triangle Park, North Carolina, 1996.
- [16] Dean R. Chapman. Computational aerodynamics development and outlook, Dryden Lecture in Research for 1979. AIAA Paper 79-0129, 1979.
- [17] S. Chapman and T. G. Cowling. *The Mathematical Theory of Non-Uniform Gases*. Cambridge University Press, New York, 1964.
- [18] COESA. *U. S. Standard Atmosphere, 1976*. NOAA, NASA, USAF, Washington, D.C., October 1976.
- [19] Georg Dettleff. Plume flow and impingement in space technology. *Prog. Aerospace Sci.*, 28:1-71. Pergamon Press, Great Britain, 1991.
- [20] T. P. Eastop and A. McConkey. *Applied Thermodynamics for Engineering Technologists, Third Edition*. Longman Inc., New York, 1978.
- [21] R. F. Eggers. Microthrust monopropellant hydrazine propulsion system technology. AIAA Paper 68-556, June 1968.
- [22] John Farley. VAAC Harrier flight test - thrusting forward (testing of advanced flight controls for vectored-thrust flight ASTOVL fighter). *Flight International*, 145(4406):22-25, February 2, 1994.
- [23] Edward D. Flinn. Quickly built model tests short takeoffs. *Aerospace America*, 34(4):18-19, April 1996.

- [24] Eric James Fuller. *Experimental and Computational Investigation of Helium Injection into Air at Supersonic and Hypersonic Speeds*. PhD thesis, Virginia Polytechnic Institute and State University, Blacksburg, Virginia, June 1992.
- [25] Benjamin Gal-Or. Civilizing military thrust vectoring flight control. *Aerospace America*, 34(4):20–21, April 1996.
- [26] A. L. Garcia, J. B. Bell, W. Y. Crutchfield, and B. J. Alder. Mesh and algorithm refinement using direct simulation Monte Carlo. In *21th International Symposium on Rarefied Gas Dynamics, Book of Abstracts, Volume 1, Oral Sessions* [1]. July 1998.
- [27] Martin R. Gilmore. Defence Evaluation and Research Agency, personal communication, August 1996.
- [28] Martin R. Gilmore and K. Warburton. Axi-symmetric hypersonic jet interaction: A combined experimental and computational study II. AIAA Paper 95–0414, January 1995.
- [29] Christopher E. Glass. A parametric study of jet interactions with rarefied flow. In *21th International Symposium on Rarefied Gas Dynamics, Book of Abstracts, Volume 1, Oral Sessions* [1]. July 1998.
- [30] Christopher E. Glass and Gerald J. LeBeau. Numerical study of a continuum sonic jet interacting with a rarefied flow. AIAA Paper 97–2536, June 1997.

- [31] Peter A. Gnoffo, K. James Weilmuenster, H. Harris Hamilton, II, David R. Olynick, and Ethiraj Venkatapathy. Computational aerothermodynamics design issues for hypersonic vehicles. AIAA Paper 97-2473, June 1997.
- [32] Daniel S. Goldin. *NASA Strategic Plan*. National Aeronautics and Space Administration, Washington, D. C., February 1996.
- [33] R. N. Gupta and A. L. Simmonds. Hypersonic low-density solutions of the Navier-Stokes equations with chemical nonequilibrium and multicomponent surface slip. AIAA Paper 86-1349, June 1986.
- [34] Roop N. Gupta, Carl D. Scott, and James N. Moss. Slip-boundary equations for multicomponent nonequilibrium airflow. NASA Technical Paper 2452, NASA, November 1985.
- [35] B. L. Haas, Hassan A. Hassan, J. N. Moss, and W. C. Rochelle. Simulating rarefied aerothermodynamics. *Aerospace America*, 33(6):28-31, June 1995.
- [36] D. B. Hash and H. Hassan. Two-dimensional coupling issues of hybrid DSMC/Navier Stokes solvers. AIAA Paper 97-2507, June 1997.
- [37] M. Holden, J. Kolly, and K. Chadwick. Calibration, validation and evaluation studies in the LENS facility. AIAA Paper 95-0291, January 1995.
- [38] M. Yousuff Hussaini, Bram van Leer, and John Van Rosendale (Eds.). *Upwind and High-Resolution Schemes*. Springer, New York, 1997.

- [39] Imageware. *Surfacer User's Guide*. Imageware, Inc., Ann Arbor, Michigan, 1995. SUR.UG./4-95.
- [40] Paul Kallender. Japan cuts spending; HOPE killed. *Space News*, 8(29):1,19, July 21-27 1997.
- [41] D. B. Kanipe. Plume/flowfield jet interaction effects on the space shuttle orbiter. *Journal of Spacecraft and Rockets*, 20(4):351–355, Jul-Aug 1983.
- [42] David B. Kanipe and Barney B. Roberts. Evolution of the wind tunnel test program for space shuttle orbiter jet interaction upon entry and comparison of predictions with flight test results. In *Proceedings of the JANNAF 13th Plume Technology Meeting*, pages 83–94, April 1982. CPIA Publication 357.
- [43] Pijust K. Kundu. *Fluid Mechanics*. Academic Press, Inc., New York, 1990.
- [44] G. J. LeBeau. A parallel implementation of the direct simulation Monte Carlo method. *Computer Methods in Applied Mechanics and Engineering, Parallel Computational Methods for Flow Simulation and Modeling*, 174:319–337, 1999.
- [45] Wayne Lee. Mars Global Surveyor project mission plan document, final version, rev. B, MGS 542–405. JPL D–12088, JPL–NASA, November 1996.
- [46] Mark P. Loomis, Ethiraj Venkatapathy, Periklis Papadopoulos, Carol B. Davies, Scott Berry, Tom Horvath, and Charles Campbell. Aeroheating and aerodynamic CFD validation and prediction for the X-38 program. AIAA Paper 97–2478, June 1997.

- [47] Forrest E. Lumpkin, III, Gerald J. LeBeau, and Phillip C. Stuart. A CFD/DSMC analysis of plumes and plume impingement during Shuttle/Mir docking. AIAA Paper 95-2034, June 1995.
- [48] Milton Marcus. Historical evolution of hydrazine thruster design. AIAA Paper 90-1838, July 1990.
- [49] William D. McGrory, David C. Slack, Michael P. Applebaum, and Robert W. Walters. *GASP Version 2.2, The General Aerodynamic Simulation Program*. AeroSoft, Inc., 1993.
- [50] Message Passing Interface Forum. MPI: A message-passing interface standard. Technical Report CS-94-230, University of Tennessee, Knoxville, TN, 1994.
- [51] Joe Morris. Primex Aerospace Corporation (formally Rocket Research Company), personal communication, 1998.
- [52] James N. Moss, Virendra K. Dogra, and Joseph M. Price. DSMC simulations of viscous interactions for a hollow cylinder-flare configuration. AIAA Paper 94-2015, June 1994.
- [53] James N. Moss, Didier F. G. Rault, and Joseph M. Price. *AIAA Progress in Astronautics and Aeronautics, Rarefied Gas Dynamics: Space Science and Engineering*, volume 160, chapter Direct Monte Carlo Simulations of Hypersonic Viscous Interactions Including Separations, pages 209-220. AIAA, 1993.

- [54] Shinji Nagai, Kouichi Hozmi, Akira Yoshizawa, Nobutoshi Hara, Keisuke Fujii, Hideo Bito, and Tadashi Katurahara. Hypersonic wind tunnel tests of RCS jet interference. In *Proceedings of the Nineteenth International Symposium on Space Technology and Science*, pages 423–430, Yokohama, Japan, 1994.
- [55] NASA. *1996 Mars Missions, Press Kit*. National Aeronautics and Space Administration, November 1996.
- [56] Ohio Supercomputer Center. *MPI Primer/Developing with LAM*. The Ohio State University, November 1996.
- [57] David R. Olynick and W. D. Henline. Navier-Stokes heating calculations for benchmark thermal protection system sizing. *Journal of Spacecraft and Rockets*, 33(6):807–814, Nov–Dec 1996.
- [58] David R. Olynick and Tim Tam. Trajectory based validation of the shuttle heating environment. *Journal of Spacecraft and Rockets*, 34(2):172–181, Mar–Apr 1997.
- [59] David J. Peake and Murray Tobak. Three-dimensional interactions and vortical flows with emphasis on high speeds. NASA Technical Memorandum 81169, NASA, March 1980.
- [60] J. Peirò, J. Peraire, and K. Morgan. FELISA SYSTEM, Version 1.1, Reference Manual, Part 2–User Manual. Swansea technical report, University College of Swansea, Swansea, U. K., August 1994.

- [61] Th. Pörtner. Simulation requirements for RCS plume-flowfield interaction modelling on a winged reentry vehicle. In Battrick [8], pages 101–106. ESA-SP-318.
- [62] Th. Pörtner. First experimental assessment of RCS plume-flow field interaction on Hermes leading edge thruster configuration. In *Computational and Experimental Assessment of Jets in a Cross Flow*, pages 31–1–31–13, Winchester, United Kingdom, April 1993. AGARD Conference Proceedings 534.
- [63] D. F. G. Rault. Aerodynamic characteristics of the Magellan spacecraft in the Venus upper atmosphere. *Journal of Spacecraft and Rockets*, 31(4):537–542, Jul–Aug 1994.
- [64] D. F. G. Rault. Methodology for thruster plume simulation and impingement effects characterized using DSMC. AIAA Paper 95–2032, June 1995.
- [65] D. F. G. Rault, Francisco J. Cestero, and Russell W. Shane. Spacecraft aerodynamics during aerobraking maneuver in planetary atmospheres. AIAA Paper 96–1890, June 1996.
- [66] Didier F. G. Rault and Michael S. Woronowicz. Application of Direct Simulation Monte Carlo to satellite contamination studies. *Journal of Spacecraft and Rockets*, 32(3):392–397, May–Jun 1995.
- [67] Paul O. Romere, David B. Kanipe, and James C. Young. Space shuttle entry aerodynamic comparisons of flight 1 with preflight predictions. *Journal of Spacecraft and Rockets*, 20(1):15–21, Jan–Feb 1983.

- [68] M. Rosenhauer, K. Plähn, and K. Hannemann. Comparison of decoupled hybrid Navier–Stokes — DSMC calculations with experiments in plumes. In *21th International Symposium on Rarefied Gas Dynamics, Book of Abstracts, Volume 1, Oral Sessions* [1]. July 1998.
- [69] R. Roveda, D. B. Goldstein, and P. L. Varghese. A hybrid Euler/DSMC approach to unsteady flows. In *21th International Symposium on Rarefied Gas Dynamics, Book of Abstracts, Volume 1, Oral Sessions* [1]. July 1998.
- [70] Roberto Roveda, David B. Goldstein, and Philip L. Varghese. A combined discrete velocity/particle based numerical approach for continuum/rarefied flows. AIAA Paper 97–1006, January 1997.
- [71] M. J. Russi. A survey of monopropellant hydrazine thruster technology. AIAA Paper 73–1263, November 1973.
- [72] R. L. Sackheim, R. A. Carlson, H. Macklis, and D. H. Lee. Evolution of a standardized monopropellant rocket engine design concept. AIAA Paper 74–1133, October 1974.
- [73] Jamshid Samareh. Gridtool: A surface modeling and grid generation tool. In *Proceedings of the Workshop on Surface Modeling, Grid Generation, and Related Issues in CFD Solutions*, pages 821–831. NASA, May 1995. NASA CP–3291.

- [74] William I. Scallion. Space shuttle reaction control system - flowfield interactions during entry. In David A. Throckmorton, editor, *Proceedings of the Orbital Experiments (OEX) Aerothermodynamics Symposium*, pages 345–370, Williamsburg, Virginia, April 1995. NASA. NASA Conference Publication 3248.
- [75] U. Schumann. Direct and large eddy simulation of turbulence—Summary of the state of the art 1991. In *Introduction to the Modeling of Turbulence, Lecture Series 1991-02*, Rhode Saint Genèse, Belgium, March 1991. von Karmen Institute For Fluid Dynamics.
- [76] Russell W. Shane, Didier F. G. Rault, and Robert H. Tolson. Mars Global Surveyor aerodynamics for maneuvers in Martian atmosphere. AIAA Paper 97-2509, June 1997.
- [77] Russell William Shane. Aerothermodynamics of the Mars Global Surveyor spacecraft. Master's thesis, George Washington University, Washington, DC, December 1997.
- [78] Bradford Smith, Gaylen R. Rinaudot, Kent A. Reed, and Thomas Wright. Initial Graphics Exchange Specification (IGES), version 4. NBSIR report 88-3813, National Bureau of Standards, Warrendale, PA, June 1988.
- [79] F. W. Spaid and L. A. Cassel. Aerodynamic interference induced by reaction controls. AGARDograph No. 173 (ADARD-AG-173), December 1973.
- [80] Charles G. Speziale. Turbulence modeling for time-dependent RANS and VLES: A review. *AIAA Journal*, 36(2):173–184, February 1998.

- [81] Phillip C. Stuart. NASA Johnson Space Center, personal communication, 1998.
- [82] Paul V. Tartabini, Richard G. Wilmoth, and Didier F. G. Rault. Direct simulation Monte Carlo calculation of a jet interaction experiment. *Journal of Spacecraft and Rockets*, 32(1):75–83, Jan–Feb 1995.
- [83] David Throckmorton. Today’s technology for tomorrow’s launch vehicles. *Aerospace America*, 33(6):20–24, June 1995.
- [84] Robert H. Tolson. JIAFS, George Washington University, personal communication, 1998.
- [85] D. C. Wadsworth and D. A. Ervin. One–dimensional hybrid continuum/particle simulation approach for rarefied hypersonic flows. AIAA Paper 90–1690, June 1990.
- [86] D. C. Wadsworth and D. A. Ervin. Two–dimensional hybrid continuum/particle approach for rarefied flows. AIAA Paper 92–1690, July 1992.
- [87] Pamela P. Walatka, Pieter G. Buning, Larry Pierce, and Patricia A. Elson. PLOT3D user’s manual. Technical Memorandum 101067, NASA, March 1990.
- [88] Keith Warburton. Defence Evaluation and Research Agency, personal communication, 1997.
- [89] Scott C. Ward. A computational model for predicting the performance of jet–interaction steering control systems for conical missiles. AIAA paper 87–0069, January 1987.

- [90] S. Watanabe, R. Takaki, and Y. Yamamoto. RCS gas-jet interactions in the hypersonic flight experiment, HYFLEX. AIAA paper 97-0524, January 1997.
- [91] Shigeya Watanabe and Ryoji Takaki. RCS gas-jet interaction experiment. In *Proceedings of the HYFLEX/HOPE-Symposium*, pages 130–137, July 1996.
- [92] Frank M. White. *Viscous Fluid Flow*. McGraw-Hill Book Company, New York, 1974.
- [93] Richard G. Wilmoth. NASA Langley Research Center, personal communication, 1998.
- [94] Richard G. Wilmoth, Gerald J. LeBeau, and Ann B. Carlson. DSMC grid methodologies for computing low-density, hypersonic flows about reusable launch vehicles. AIAA Paper 96-1812, June 1996.
- [95] Richard G. Wilmoth and Paul V. Tartabini. Three-dimensional DSMC calculations of jet/corner flow interactions. In *Proceedings of the 19th International Symposium on Rarefied Gas Dynamics*, Oxford University, Oxford, England, July 1994.
- [96] Yukimitsu Yamamoto. Numerical simulation of hypersonic viscous flow for the design of H-II Orbiting Plane (HOPE) Part II. AIAA paper 91-1390, June 1991.
- [97] Changan Zhang, David A. Randall, Chin-Hoh Moeng, Mark Branson, Kerry A. Moyer, and Qing Wang. A surface flux parameterization based on the vertically averaged turbulence kinetic energy. *Monthly Weather Review*, 124(11):2521–2536, November 1996.

REPORT DOCUMENTATION PAGE			Form Approved OMB No. 0704-0188	
Public reporting burden for this collection of information is estimated to average 1 hour per response, including the time for reviewing instructions, searching existing data sources, gathering and maintaining the data needed, and completing and reviewing the collection of information. Send comments regarding this burden estimate or any other aspect of this collection of information, including suggestions for reducing this burden, to Washington Headquarters Services, Directorate for Information Operations and Reports, 1215 Jefferson Davis Highway, Suite 1204, Arlington, VA 22202-4302, and to the Office of Management and Budget, Paperwork Reduction Project (0704-0188), Washington, DC 20503.				
1. AGENCY USE ONLY (Leave blank)		2. REPORT DATE November 2000		3. REPORT TYPE AND DATES COVERED Technical Publication
4. TITLE AND SUBTITLE Numerical Study of Rarefied Hypersonic Flow Interacting With a Continuum Jet			5. FUNDING NUMBERS WU 242-80-01-01	
6. AUTHOR(S) Christopher E. Glass				
7. PERFORMING ORGANIZATION NAME(S) AND ADDRESS(ES) NASA Langley Research Center Hampton, VA 23681-2199			8. PERFORMING ORGANIZATION REPORT NUMBER L-18029	
9. SPONSORING/MONITORING AGENCY NAME(S) AND ADDRESS(ES) National Aeronautics and Space Administration Washington, DC 20546-0001			10. SPONSORING/MONITORING AGENCY REPORT NUMBER NASA/TP-2000-210551	
11. SUPPLEMENTARY NOTES The information presented in this report was offered as a thesis for the degree of Doctor of Philosophy, The Pennsylvania State University, August 1999. Because of its length, the appendix is available only online at http://techreports.larc.nasa.gov/ltrs/PDF/2000/tp/NASA-2000-tp210551app.pdf				
12a. DISTRIBUTION/AVAILABILITY STATEMENT Unclassified-Unlimited Subject Category 34 Distribution: Standard Availability: NASA CASI (301) 621-0390			12b. DISTRIBUTION CODE	
13. ABSTRACT (Maximum 200 words) An uncoupled CFD-DSMC technique is developed and applied to provide solutions for continuum jets interacting with rarefied external flows. The technique is based on a correlation of the appropriate Bird breakdown parameter for a transitional-rarefied condition that defines a surface within which the continuum solution is unaffected by the external flow-jet interaction. The method is applied to two problems to assess and demonstrate its validity: one of a jet interaction in the transitional-rarefied flow regime and the other in the moderately rarefied regime. Results show that the appropriate Bird breakdown surface for uncoupling the continuum and non-continuum solutions is a function of a non-dimensional parameter relating the momentum flux and collisionality between the two interacting flows. The correlation is exploited for the simulation of a jet interaction modeled for an experimental condition in the transitional-rarefied flow regime and the validity of the correlation is demonstrated. The uncoupled technique is also applied to an aerobraking flight condition for the Mars Global Surveyor spacecraft with attitude control system jet interaction. Aerodynamic yawing moment coefficients for cases without and with jet interaction at various angles-of-attack were predicted, and results from the present method compare well with values published previously.				
14. SUBJECT TERMS Continuum jet interaction; Direct simulation Monte Carlo; Mars Global Surveyor (MGS); Rarefied flow; Reaction control system (RCS); Uncoupled CFD-DSMC			15. NUMBER OF PAGES 219	
			16. PRICE CODE A10	
17. SECURITY CLASSIFICATION OF REPORT Unclassified	18. SECURITY CLASSIFICATION OF THIS PAGE Unclassified	19. SECURITY CLASSIFICATION OF ABSTRACT Unclassified	20. LIMITATION OF ABSTRACT UL	